

Chemotaxis of self-phoretic active particles and bacteria

vorgelegt von
Diplom-Mathematiker

Oliver Pohl

geboren in Weimar

von der Fakultät II - Mathematik und Naturwissenschaften
der Technischen Universität Berlin
zur Erlangung des akademischen Grades
Doktor der Naturwissenschaften (Dr. rer. nat.)

genehmigte

Dissertation

Promotionsausschuss:

Vorsitzender: Prof. Dr. rer. nat. Michael Lehmann

Erster Gutachter: Prof. Dr. rer. nat. Holger Stark

Zweiter Gutachter: Prof. Dr. rer. nat. Ralf Metzler

Tag der wissenschaftlichen Aussprache 31. Mai 2016

Berlin 2016

Contents

1. Introduction	5
2. Statistical physics of active motion	11
2.1. Introduction of stochastic processes	11
2.1.1. Brownian motion	11
2.1.2. White noise and Langevin dynamics	13
2.1.3. Stochastic differential equations and their interpretation	15
2.1.4. Fokker-Planck equation	17
2.1.5. Shot noise	19
2.1.6. Kramers-Moyal coefficients	24
2.2. Active Motion	25
2.2.1. Active motion in biology and synthetic systems	25
2.2.2. A model for an active swimmer	26
2.2.3. Collective motion of active particles	29
3. Chemotaxis and diffusiophoresis	33
3.1. Macroscopic perspective: Keller-Segel model	33
3.2. Chemotaxis in bacterial systems	34
3.2.1. Random Walk of the bacteria <i>E.coli</i> and <i>P.putida</i>	36
3.2.2. Chemotaxis of <i>E.coli</i>	36
3.2.3. Inference of the response function	38
3.2.4. Chemokinesis vs. Chemotaxis	40
3.3. Diffusiophoresis: How chemical gradients lead to colloidal motion	43
3.3.1. Basic hydrodynamics: Navier-Stokes and Stokes equations	43
3.3.2. Slip velocity \mathbf{v}_s	45
3.3.3. Swimming velocity and torque	47
4. Dynamic clustering and chemotactic collapse in a system of active colloids	49
4.1. Introduction	49
4.2. Lyon Experiments	50
4.3. Model for active colloids with interactions transmitted by a chemical field	51
4.3.1. Derivation of the model equations	51
4.3.2. Rescaling	54
4.3.3. Screening, repulsive particle-particle and particle-wall interactions	54
4.3.4. Numerical implementation	55
4.4. Statediagram: Overview of the phenomenology	56
4.5. Gas phase, Dynamic clustering 1 and 2	57
4.5.1. Dilute regime: $\sigma = 5\%$	57

4.5.2.	Dynamic clustering for varying area fractions σ	60
4.5.3.	Dynamic clustering for varying Péclet number	62
4.6.	Collapse Regimes	63
4.7.	Relation to the Keller-Segel model	66
4.7.1.	Mapping of the colloidal model to the Keller-Segel equations	67
4.7.2.	Comparison of mean field equations with simulations	69
4.8.	System without screening	70
4.8.1.	Dynamic clustering without screening	70
4.8.2.	Collapse without screening	71
4.9.	Cluster dynamics: Fusion and fission rates	74
4.10.	Conclusion	76
5.	Inference of chemotaxis of the bacteria <i>E.coli</i> and <i>P.putida</i>	79
5.1.	Introduction	79
5.2.	Shot noise model for run-and-tumble motion	82
5.3.	Inference	83
5.3.1.	Experiments	83
5.3.2.	Absolute conditioned Moments	84
5.3.3.	Calculating CMs from experimental trajectories	88
5.4.	Overall tumbling statistics	90
5.4.1.	Tumbling statistics of <i>E.coli</i>	90
5.4.2.	Defining a novel tumble recognizer	92
5.4.3.	Tumbling statistics of <i>P.putida</i>	94
5.5.	Chemotaxis and Chemokinesis	95
5.5.1.	Adaptedness to the background concentration	96
5.5.2.	Chemotactic strategies	98
5.5.3.	Temporal chemotaxis: Testing the response function	103
5.6.	Conclusion	107
6.	Conclusions	109
A.	CM Inference method	113
A.1.	Calculation of odd conditioned moments	113
A.2.	Materials and Methods	113
A.3.	Numerical details	115
A.4.	Trajectory analysis	117
A.5.	Chemotaxis in late trajectories $T= 30,45$ min. and $T= 60$ min.	117
A.6.	Moments of P_β of <i>P.putida</i>	120
A.7.	CM ratios for <i>P.putida</i>	120

Introduction

In biology, chemotaxis refers to directed motion of an organism in response to chemical concentration gradients. A sophisticated biochemical signaling pathway permits even the smallest known living organisms, i.e., bacteria, to successfully perform chemotaxis on micrometer scale [1]. Larger and more complex creatures such as amoeba [2] or human cells [3] perform chemotaxis and, in a broader context, insects or mammals follow concentration gradients by means of their olfactory organ [4]. Chemotaxis enables living organisms to find sources of nutrients by following their gradient traces. Moreover, when chemicals are produced by the agents themselves, chemotaxis can lead to information exchange, i.e., communication. In cellular colonies this leads to the formation of biofilms containing billion of cells, a phenomenon which dates back more than 3 billion of years [5]. For mammals, olfactory information not only leads to sources of food, but also influences their social interaction. In short, chemotaxis is an essential part of life.

Meanwhile, remaining on the micron scale, the study of *active colloids* has attracted increasing attention [6, 7]. These particles move through their ambient fluid by converting different kinds of energy into kinetic energy. On human length scales such machines have of course been produced prominently since the middle of the 19th century, however, motors on micron scale constitute a recent development. The energy sources, which empower these tiny particles are diverse, ranging from light [8, 9], through chemical concentrations in the ambient fluid [10], to electricity [11]. The colloids may consist of different kinds of materials, for instance oil [12, 13], metals [10, 14] or silicon [15]. Once activated, they can exert work and perform transport tasks [16], they may form “molecules” [17] or even self-reproduce [18]. Last but not least, they can be directed along chemical gradients [10].

Microorganisms such as cells on the one hand and active colloids on the other are typically studied by different subject areas, the first primarily by biology and the second by material science or chemistry. Nevertheless, physicists are interested in both. This is because, from a physicist’s point of view, they share several key properties. First of all, be it a bacterium metabolizing nutrients or a colloid acting as a catalyst for various reactions on its surface, both move actively through its surrounding as a result of conversion of ambient energy sources. The field of *active particles*, sometimes called *active matter*, has recently received enormous attention in the physical community [19–23]. During the active motion, energy is constantly produced such that the systems are intrinsically *out-of-equilibrium*. Indeed, many of their fascinating properties are owed to the violation of laws of classical equilibrium statistical mechanics. This is true in particular for large assemblies of active particles when *collective behavior* emerges. The

latter constitutes another common property of biological and colloidal systems. In fact, collective phenomena are ubiquitous in nature, prominent examples comprise flocking birds [24, 25], swarming midges [26], and schooling fish [27] on large scales, macroscopic spiral formations in colonies of amoeba [28] or biofilm formation of bacteria on micron scale. Many of these phenomena have been elucidated by the application of concepts from statistical physics, such as (non-equilibrium) phase transitions [25, 29], minimizing entropy techniques [30], exit times [31], anomalous diffusion, or aging [32, 33], to just mention a small selection. On the other hand, active colloidal systems are typically more controllable and less complex than their biological counterparts, so that collective phenomena can be studied with higher accuracy and, therefore, constitute ideal model systems for biological collective phenomena. Recently, cluster formation in systems of active colloids has been discussed, particularly non-equilibrium versions like dynamic clustering [14] or cluster formation in high density systems with phase separation [34] have become focus of interest.

Finally, when the concept of chemotaxis is stripped off its bio-chemical content and is just defined via its phenomenological dynamical characteristic, which is, response to a chemical concentration gradient, then this property emerges as well in synthetic systems. In fact, colloids are observed to move along chemical gradients [35]. The underlying physical effect is called diffusiophoresis, a concept studied in line with electrophoresis or thermophoresis referring to motion along electrical fields or temperature gradients [36]. It describes the motion of a particle in response to a chemical concentration gradient extending along the particle's surface.

This thesis consists of two projects. In the following, we provide a motivation and an introduction of both. We start with a study of active colloids.

Dynamic clustering and chemotactic collapse in a system of active colloids

The experiments presented in Ref. [14] very much inspired this project. In fact, they represent an example, in which the three aforementioned phenomena, active motion, collective behavior, and chemotaxis meet in a single system. The setup consists of an assembly of so-called *Janus particles*, which are colloids covered with two different materials on their respective sides. This material inhomogeneity effectively leads to active motion under the consumption of a certain chemical. As a consequence, chemical gradients build up, which causes motion of neighboring particles along the gradients by means of diffusiophoresis. Hence, a chemical field mediates interactions between the colloids, reminiscent of chemotaxis in bacterial colonies. The system exhibits *dynamic clustering*, a state in which clusters dynamically emerge and dissolve.

Somewhat earlier in 2011, the numerical study of Ref. [34] and later [21] discussed phase separation in a system of active disks moving in two dimensions and interacting only by a hard-core repulsion potential. For high enough densities one large, crystalline cluster emerges together with a gas-like state of freely swimming particles. As has been

detailed in a series of analytical studies [37–39], activity alone can lead to this instance of phase separation. This is no longer true at low density regimes as, for instance, in the experiments [14] or [35]. Without attractive interactions, occasional collisions are too rare and short-lived to create a nucleus from which one giant cluster can form. Indeed, in Ref. [35] effective diffusiophoretic interactions were experimentally measured. Only these lead to collective behavior in form of dynamic clustering.

Similar setups have been investigated from a theoretical perspective. In Ref. [9] a system of active colloids interacting via thermophoresis was shown to exhibit a collapsed state, in which all particles gather in one large cluster. It was termed “super-nova” in the given thermophoretic context. Ref. [40] implements diffusiophoresis for specific surface properties of self-phoretic colloids and identifies various states such as clumping and asters. However, the theoretical understanding of such non-equilibrium colloidal systems remains limited. In particular, dynamic clustering has not yet been explained. In Refs. [9] and [14] the authors related the colloidal system to the *Keller-Segel equations* [41]. They are known from bacterial chemotaxis and predict a collapse to one large cluster for strong chemotactic response. A dynamic collapse was reported in a theoretical study of bacteria interacting via chemotaxis [42]. It was shown that in specific situations such a collapsed cluster may break and merge again, a phenomenon which was termed “hot clustering”. However, a mapping of the full diffusiophoretic picture to the Keller Segel setup has not yet been provided. Also, to our knowledge there is no study dealing with the dynamic collapse behavior in active colloidal systems.

In this thesis, we develop a model for an assembly of active colloids, which interact by means of the gradients of a chemical field. Each particle consumes the chemical for its active motion, thereby creating sinks. Solving the respective diffusion equation, one obtains long-ranged chemical gradients. As we shall show, they have a twofold diffusiophoretic effect. First, the particles drift along (or against) the gradient independent of their active moving direction. Second, because they are Janus-particles, the colloids also align (or anti-align) their moving direction with the gradients. Together with the chemical gradients, which create the colloids themselves, an effective diffusiophoretic interaction is established between them. Last, we take into account that interactions of particles in large clusters are screened because the chemical field cannot diffuse freely. By means of Brownian dynamic simulations of the above model, we give evidence that dynamic clustering emerges only when the two phoretic effects counteract. Moreover, we locate the transition from a gas-like to a collapsed state depending on the phoretic parameters. This transition is discussed in the framework of the Keller-Segel equations, to which we map our phoretic model. The collapsed state is studied in more detail and we show the existence of a regularly pulsating cluster, which emerges again in the case of counteracting phoretic interactions. Finally, we calculate fusion and fission rates locally on dynamically evolving clusters and show that they can be used to characterize dynamic clustering.

Next, we focus on living organisms again, in particular, on the description of bacterial chemotaxis. This forms the second project of this thesis.

Inference of chemotaxis and chemokinesis in bacteria

The modeling of bacterial chemotaxis is typically much more involved, since cascades of biochemical reactions need to be considered to successfully predict the chemotactic response. Hence, such models typically have many degrees of freedom [43, 44]. This refers, in particular, to the bacterium *E.coli*, probably the best studied bacterium in the world. The biochemical machinery which enables the cell to perform chemotaxis is well understood, and so is its biased random walk, which guides the cell to more nutritive sides [45]. It consists of alternating runs, during which the bacterium nearly moves straight, and tumbles, where it reorients its moving direction randomly.

For chemotaxis, the bacterium extends its runs in gradient direction, thereby biasing the random walk and inducing a drift along the gradient [46]. A bacterium typically recognizes the gradient direction by means of *temporal chemotaxis*. Therefore, the chemotactic information is obtained based on the chemical concentration the bacterium experienced along its past trajectory. Its according response can be mathematically described with the aid of a *response function* that was experimentally measured [47, 48]. Temporal chemotaxis stands in contrast to *spatial chemotaxis*, according to which eukaryotic cells recognize the gradient instantaneously, by effectively comparing the concentration field at various points along their membranes. To analyze the random walk, *tumble recognizers* are used (*e.g.* in [46, 48]), which identify tumbles. However, such a heuristic procedure involves the setting of a number of threshold parameters, which need to be chosen based on visual inspection of the trajectories.

We here present a different approach. For this purpose, a basic model for the run-and-tumble motion of bacteria is defined, which is restricted to the main dynamic features of the random walk. It permits us, to analytically calculate its *conditioned moments*, which are similar to the so-called *Kramers-Moyal coefficients*. They have been previously used to distinguish between diffusive and drift motion in experimentally recorded trajectories [49, 50]. As we shall show, when matching the analytical moments to the ones obtained from experimental trajectories, one can *infer* the parameters from the model. In particular, the tumble rate, the rotational diffusion constant and the mean tumble angle are determined. To exploit this inference technique, we make use of experimental trajectories recorded in experiments of the bacteria *E.coli* and *P.putida*. Their respective random walks look very different, however, both turn out to be well described by our model.

In addition, we show how the method can be used to define a novel tumble recognizer, for which no unknown parameters need to be determined. Rather, it gets calibrated with the previously inferred parameters. Next, when studying bacteria in nutrient gradients, we show that our inference setup is capable to study spatial and temporal chemotaxis

as well as *chemokinesis*. The latter refers to a bacterial response to the background concentration of a chemical. Our inferred results for *E.coli* give evidence that a small subpopulation biases not only its tumble rate, but also its tumble angle as additional chemotaxis strategy. We support this result by a scaling argument of moment ratios, which are directly calculated from the experiments. An angle bias was previously reported in Ref. [51], however, it was characterized as a weak bias applied equally by all bacteria. For the second bacterium, *P.putida*, we show by analyzing its chemotaxis and -kinesis statistics that this bacterium is not adapted to a certain chemical. This means, that its chemotactic response depends on the background concentration of the nutrient. Last, we show how various response functions can be tested when studying the bacterial response conditioned on its past trajectory. In the following, we give a brief outline of this thesis.

Outline

In Chap. 2, we first introduce concepts from the field of stochastic processes, which serve as a theoretical framework for the entire thesis. Making use of them, we introduce active motion and outline an analysis of an assembly of active particles.

Next, we discuss the concepts of chemotaxis and its colloidal counterpart, diffusio-phoresis, in Chap. 3. We provide a discussion of the Keller-Segel-model, which captures essential features of chemotaxis on a mean field level. Chemotaxis in bacterial systems is discussed in more detail. In particular, we provide a comparison to the concept of chemokinesis by analyzing two particular response functions.

Chap. 4 essentially bases on our two articles [52, 53]. First, a model for a system of active colloids is introduced, which exhibits dynamic clustering. The theory of diffusio-phoresis is used to rationalize interactions between the particles. The model is shown to reproduce dynamic clustering and is classified into dynamic clustering 1 and 2 based on appropriate cluster statistics. Next, we study the collapsed state, in particular, its dynamic properties are discussed. A mapping of the phoretic model to the Keller-Segel equations is provided to rationalize the occurrence of the collapsed state. Finally, we calculate “reaction rates“ of the dynamic clusters and show how they can be used to detect phoretic interactions.

In Chap. 5, we start with a model for bacterial run-and-tumble behavior. We give a brief overview of the experiments, which record trajectories of the bacteria *E.coli* and *P.putida*. Next, we introduce so-called conditioned moments and calculate them for the shot noise model. They are matched with the conditioned moments obtained from the experiments to infer the model parameters. As a first result, tumble statistics averaged over all moving directions are presented, i.e., the chemical gradient is ignored. It

is shown how to define a novel tumble recognizer based on the previous inference. We draw conclusions on the bacteria's chemotactic and chemokinetic behavior, by conditioning the Kramers-Moyal coefficients appropriately. In particular, we discuss chemotactic strategies of *E.coli* and *P.putida*. Furthermore, the adaption of *P.putida* to the nutrient benzoate is studied. Last, we show that temporal chemotaxis can be detected when conditioning on the past.

Finally, in Chap. 6 we summarize our work and provide an outlook.

Statistical physics of active motion

In this chapter, we elaborate the concept of active motion. For this purpose, we first introduce stochastic methods to describe stochastic processes, present examples, and discuss some of their properties. In fact, the elaborated concepts will be used throughout the entire thesis. They will be applied to define a model of active particles and to discuss its basic properties. Finally, collective behavior in a model system of an assembly of active particles is discussed.

2.1. Introduction of stochastic processes

In the following, we introduce various concepts from the theory of stochastic processes, which will be frequently used throughout this thesis. In particular, we provide three descriptions of stochastic processes, namely the Langevin equation, the Fokker-Planck equation and Kramers-Moyal coefficients. We discuss their connection and present examples. In addition we introduce the concept of shot-noise and include it into the Langevin and Fokker-Planck setup. We start with the introduction of Brownian motion.

2.1.1. Brownian motion

In 1827 Robert Brown made a startling discovery, when observing spherosomes ejected from pollen grains. They performed a continuous noisy motion [see Fig. 2.1] in water. He repeated the experiments with inorganic matter of similar size and, observing the same jittery motion, he concluded that the motion is not related to life [54]. How could one explain this phenomenon? The key observation is that the particle in consideration is emerged in a liquid. Due to thermal motion the liquid particles (size of water molecules $\approx 0.29\text{nm}$) move and hit the larger spherosome particles ($\approx 0.5\mu\text{m}$) [55]. In the following, we call the process, which describes the position of the particle, $\mathbf{B}(t)$ and motivate its properties.

First of all, the water molecules move in each direction with the same probability, for which reason we expect the displacement of the large particles to vanish on average. Furthermore, the kicks in a given time interval can be considered as numerous independent stochastic variables, the sum of which obeys approximately a normal distribution due to the central limit theorem. Assuming the kicks to happen independently leads to independent increments of $\mathbf{B}(t)$. Last, we do not expect the particle to teleport or tunnel through space and hence we assume the paths of $\mathbf{B}(t)$ to be continuous (which

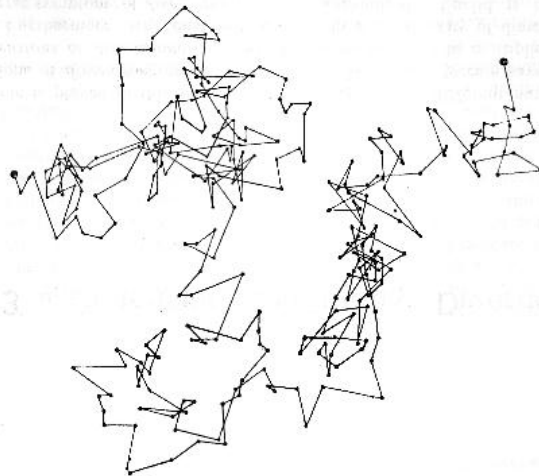


Figure 2.1.: Jittery motion of a small pollen as observed by Robert Brown in 1827

does not follow from the previous conditions). Summing up, we obtain the following characterization of the so-called Brownian motion in d dimensions [56]:

1. The increment $\mathbf{B}(t) - \mathbf{B}(t')$ is independent of $\mathbf{B}(s) - \mathbf{B}(s')$ for any $t > t' \geq s > s'$
2. \mathbf{B} is a *continuous* stochastic process in time
3. $\mathbf{B}(t) - \mathbf{B}(s)$ is Gaussian with mean 0 and covariance matrix $\mathbf{1}q(t - s)$ for $t \geq s \geq 0$

In section 2.1.2 the constant q will be related to temperature and friction.

The scaling of Brownian motion with time is different from regular smooth motion. More quantitatively, one can show that the the "second variation" $[\mathbf{B}(t), \mathbf{B}(t)]$ is finite [56]:

$$[\mathbf{B}(t), \mathbf{B}(t)] = \lim_{\Delta t \rightarrow 0} \sum_{n=0}^{\lceil t/\Delta t \rceil} |\mathbf{B}(t_{n+1}) - \mathbf{B}(t_n)|^2 = dqt, \quad (2.1)$$

where $t_{n+1} = t_n + \Delta t$ and $t_0 = 0$. This can be shown by first verifying that $\langle [\mathbf{B}(t), \mathbf{B}(t)] \rangle = dqt$. In a second step, one shows that the variance of $[\mathbf{B}(t), \mathbf{B}(t)]$ vanishes, thereby proving that $[\mathbf{B}(t), \mathbf{B}(t)]$ gives deterministically the result specified in Eq. (2.1). This equation has various consequences. First of all, Brownian motion is not differentiable because $[f(t), f(t)]$ for differentiable functions f vanishes. Second, it motivates the symbolic notion " $d\mathbf{B}(t)^2 = qd \cdot dt$ ". However, note that for any finite dt the increment $d\mathbf{B}(t)^2$ is a stochastic random variable, and the aforementioned relation holds only on average, i.e., $\langle d\mathbf{B}(t)^2 \rangle = qd \cdot dt$. Last, Levy's theorem states that Eq. (2.1), together with the so-called

martingale condition $\langle \mathbf{B}(t) | \mathbf{B}(s) = \mathbf{x} \rangle = \mathbf{x}$ (for $s \leq t$), define the concept of Brownian motion completely (no need to require the increments to be Gaussian or continuous) [57].

2.1.2. White noise and Langevin dynamics

In the previous section, we have not explicitly considered friction in our approach to model the spherosomes. In fact, we assumed *overdamped motion* meaning that inertia can be neglected and forces directly translate into velocities. We discuss the transition from underdamped to overdamped motion in Sec. 2.2.2 and 3.3.1 in more detail. In the following *Langevin* approach friction as well as inertia lead to the generalized Newtonian equation [58]:

$$\dot{\mathbf{r}} = \mathbf{v}, \quad (2.2)$$

$$M\dot{\mathbf{v}} = -\gamma\mathbf{v} + \boldsymbol{\xi}, \quad (2.3)$$

where γ is the friction coefficient, M the mass, and $\boldsymbol{\xi}(t)$ models a stochastic force. We define it and discuss its properties in the following paragraph.

White noise

The stochastic force is transmitted by random kicks of the ambient fluid particles and can be modeled by a *Gaussian white noise* process $\boldsymbol{\xi}(t)$. On average this force vanishes at every time t and it is δ -correlated:

$$\langle \boldsymbol{\xi}(t) \rangle = 0, \quad (2.4)$$

$$\langle \boldsymbol{\xi}(t) \otimes \boldsymbol{\xi}(s) \rangle = q\mathbf{1}\delta(t - s), \quad (2.5)$$

where q for the time being is a free constant.¹

Gaussian white noise process is deeply connected to Brownian motion. One can indeed define $\boldsymbol{\xi}$ as "derivative" of Brownian motion, so that one writes $\frac{d\mathbf{B}(t)}{dt} = \boldsymbol{\xi}(t)$.² Using this definition, we can show the two properties (2.4) and (2.5) of the white noise process. In fact, we first observe that

$$\langle \boldsymbol{\xi}(t) \rangle = \left\langle \frac{d\mathbf{B}(t)}{dt} \right\rangle = \frac{\langle d\mathbf{B}(t) \rangle}{dt} = 0, \quad (2.6)$$

since Brownian increments have zero mean. To check for Eq. (2.5), we introduce two smooth test functions ϕ and ρ with compact support meaning that they are non-zero only in a bounded region. Then, we calculate component wise for any indices i and j :

¹To fully define $\boldsymbol{\xi}$ as *Gaussian* white noise, one requires all higher cumulants than order two to be zero.

²Clearly, since Brownian motion is not differentiable, there is no derivative in the classical sense.

However, it can be rigorously shown that Gaussian white noise is the distributional derivative of Brownian motion [56].

$$\begin{aligned} \int_{-\infty}^{\infty} \int_{-\infty}^{\infty} \langle \xi_i(t) \xi_j(s) \rangle \phi(t) \rho(s) dt ds &= \int_{-\infty}^{\infty} \int_{-\infty}^{\infty} \langle dB_i(t) dB_j(s) \rangle \phi(t) \rho(s) = \\ q \int_{-\infty}^{\infty} \delta(ij) \phi(t) \rho(t) dt &= q \int_{-\infty}^{\infty} \int_{-\infty}^{\infty} \delta(ij) \delta(t-s) \phi(t) \rho(s) dt ds, \end{aligned}$$

where $\delta(ij)$ is the Kronecker- δ . For the second equation we use $\langle dB_i^2(t) \rangle = q \cdot dt$ and that increments as well as components are uncorrelated $\langle dB_j(t) dB_i(t) \rangle = \langle dB_i(t) dB_i(s) \rangle = 0$ for $s \neq t$ and $i \neq j$, while for the third equation the definition of the δ -function is applied. Hence, the white noise is also δ -correlated when defined via Brownian motion.³

Using the Wiener-Khinchine theorem, one can write the power spectrum $S[\xi]$ of a one-dimensional white noise process ξ in terms of its autocorrelation function:

$$\begin{aligned} S[\xi](\omega) &:= \lim_{T \rightarrow \infty} \frac{1}{2T} \left\langle \left(\int_{-T}^T \exp(-2\pi i \omega t) \xi dt \right)^2 \right\rangle \\ &= \lim_{T \rightarrow \infty} \frac{1}{2T} \int_{-T}^T \int_{-T}^T \exp(2\pi i \omega t) \langle \xi(t + \tau) \xi(\tau) \rangle d\tau dt. \end{aligned} \quad (2.7)$$

Substituting Eq. (2.5) gives the result:

$$S[\xi](\omega) = \lim_{T \rightarrow \infty} \frac{1}{2T} \int_{-T}^T \exp(0) q d\tau = q,$$

which means that the power spectrum contains equal contributions of all frequencies. Therefore, ξ is called *white* noise. One also obtains a first interpretation of q as the amplitude of the white noise power spectrum. In the following, we make use of the properties of Gaussian white noise, when discussing the Langevin approach.

Langevin equation

We introduce the rate $\tilde{\gamma} := \frac{\gamma}{M}$. The linear equation (2.3) can be solved exactly given an initial velocity $\mathbf{v}(0)$:

$$\mathbf{v}(t) = \mathbf{v}(0) \exp(-t\tilde{\gamma}) + \frac{1}{M} \int_0^t \exp[-(t-t')\tilde{\gamma}] \boldsymbol{\xi}(t') dt'. \quad (2.8)$$

This allows us to calculate the autocorrelation function:

$$\langle v_i(t) v_i(s) \rangle = v_i(0)^2 \exp[-\tilde{\gamma}(t+s)] + \frac{q}{2M\tilde{\gamma}} [\exp[-\tilde{\gamma}|t-s|] - \exp[-\tilde{\gamma}(t+s)]]. \quad (2.9)$$

³Indeed, with the definition of Gaussian white noise via Brownian motion, one can also proof that all higher cumulants of ξ vanish using that the normal distribution has this very property.

For unequal indices $i \neq j$ the correlation is zero. In the stationary state, i.e., for large times s and t , the first and third term on the right-hand side vanish and we can calculate the kinetic energy of the d -dimensional system:

$$\langle E \rangle = \frac{1}{2} M \langle |\mathbf{v}(t)|^2 \rangle = \frac{1}{2} M d \frac{q}{2\gamma M}. \quad (2.10)$$

According to the *equipartition theorem* the kinetic energy equals the thermal energy:

$$\frac{1}{2} M \langle |\mathbf{v}(t)|^2 \rangle = \frac{d}{2} k_B T. \quad (2.11)$$

Together with Eq. (2.10), this allows us to determine our unknown parameter $q = 2\gamma k_B T$. Yet, we can give q another interpretation in terms of average moving distance when calculating the mean square displacement:

$$\begin{aligned} \langle |\mathbf{r}(t) - \mathbf{r}(s)|^2 \rangle &= \int_s^t \int_s^t \langle \mathbf{v}(t') \cdot \mathbf{v}(s') \rangle dt' ds' \\ &= d \left[\left(|\mathbf{v}(0)|^2 - \frac{q}{2\gamma M} \right) \frac{[\exp(-\tilde{\gamma}s) - \exp(-\tilde{\gamma}t)]^2}{\tilde{\gamma}^2} + \frac{q(t-s)}{\gamma^2} - \frac{qM}{\gamma^3} [1 - \exp[-\tilde{\gamma}(t-s)]] \right]. \end{aligned} \quad (2.12)$$

For large t and s we can disregard all terms but the one linear in $t - s$:

$$\langle |\mathbf{r}(t) - \mathbf{r}(s)|^2 \rangle \approx \frac{qd}{\gamma^2} (t - s) = 2dD(t - s), \quad (2.13)$$

where we introduced the diffusion constant $D := \frac{q}{2\gamma^2}$. From this we obtain the celebrated Stokes-Einstein equation:

$$D = \frac{k_B T}{\gamma}. \quad (2.14)$$

2.1.3. Stochastic differential equations and their interpretation

In the previous section, we have introduced the Langevin approach, which adds a stochastic force to Newtonian dynamics. One can extend this formalism to the case in which the deterministic as well as the stochastic part are functions of the stochastic process itself. To this end, one defines the *generalized Langevin equation* or *stochastic differential equation* (SDE) for a stochastic process $X(t)$:

$$\dot{X} = f(X) + g(X)\xi, \quad (2.15)$$

where f and g are smooth functions. If $g = 0$, we are left with an ordinary differential equation (ODE). In Eq. (2.3) and (2.8) we essentially treated the Langevin equation as a linear ODE with the noise as inhomogeneity. However, it turns out that this is no longer

possible for Eq. (2.15) when the noise amplitude depends on X itself. Indeed, Eq. (2.15) without further interpretation is not well-defined. To treat this problem, one writes it in integral form [56]:

$$\int_0^t \dot{X}(s)ds = \int_0^t f[X(s)]ds + \int_0^t g[X(s)]dB(s), \quad (2.16)$$

where we used the connection between white noise and Brownian motion established in the previous section. The so-called *stochastic integral* for a given α is defined as

$$\int_0^t g[X(s)]dB(s) := \lim_{\Delta t \rightarrow 0} \sum_{n=0}^{\lceil t/\Delta t \rceil} g\left(\alpha X(t_{n+1}) + (1-\alpha)X(t_n)\right)dB(t_n), \quad (2.17)$$

with $t_{n+1} = t_n + \Delta t$, $t_0 = 0$, and $dB(t_n) = B(t_{n+1}) - B(t_n)$. As we shall see, due to the particular scaling properties of Brownian motion, it makes a significant difference at which intermediate point the function g is evaluated. Frequently, the integral equation (2.16) is written in differential form

$$dX(t) = f[X(t)]dt + g[X(t)]dB(t) \quad (2.18)$$

$$= f[X(t) + \alpha dX(t)]dt + g[X(t) + \alpha dX(t)]dB(t). \quad (2.19)$$

There are three common choices for α :

- $\alpha = 0$: Ito interpretation
- $\alpha = \frac{1}{2}$: Stratonovich interpretation
- $\alpha = 1$: Klimontovich interpretation

We perform a Taylor expansion to first order to relate the SDEs (2.19) for different α :

$$g[X(t) + \alpha[X(t + \Delta t) - X(t)]] \approx g(X) + \alpha g'(X)dX$$

When plugging this into Eq. (2.19) we obtain

$$\begin{aligned} dX &= f(X + \alpha dX)dt + g(X + \alpha dX)dB \\ &\approx f(X)dt + \alpha f'(X)dtdX + g(X)dB + \alpha g'(X)dBdX \\ &= f(X)dt + g(X)dB + \alpha f'(X)[f(X)dt + g(X)dB]dt + \alpha g'(X)[f(X)dt + g(X)dB]dB \\ &\approx [f(X) + \alpha g(X)g'(X)]dt + g(X)dB, \end{aligned} \quad (2.20)$$

where terms including $dtdB$ and dt^2 are neglected. Indeed, one can proof the integral version of Eq. (2.20) exactly by making use of the mean value theorem for integrals. In

this sense, Eq. (2.20) can be treated as exact formula. Hence, the stochastic differential equation in Ito interpretation $dX = f(X) + \frac{1}{2}g(X)g'(X)dt + g(X)dB(t)$ is equivalent to $dX = f(X)dt + g(X) \circ dB(t)$ in the Stratonovich interpretation. Note that whenever g is constant, there are no different interpretations. Then the noise is called *additive*, otherwise *multiplicative*. The fact that a multiplicative SDE is not uniquely defined unless the interpretation is specified, is sometimes referred to as *Stratonovich-Ito-dilemma*. We will give physical examples in section 2.2.2 and 3.2.4, where "the correct interpretation" is discussed. As we shall see, it depends on the specific case at hand. In particular, the origin of the function g needs to be considered.

Next, we study the transformation behavior, when the stochastic process X is transformed by a smooth function h . A similar expansion as above gives the generalized chain rule for SDEs called Ito-Lemma:

$$dh(X) = h'(X)dX + \frac{1}{2}h''(X)dX^2 = (f(X)dt + g(X)dB)h'(X) + \frac{1}{2}g^2h''(X)dt,$$

where X solves the Ito-equation (2.19). With some more calculation one can show that a Stratonovich solution $X(t)$ does apply the familiar chain rule [59]:

$$dh(X) = h'(X)dX.$$

To keep the procedure transparent, we restricted ourselves to one dimension. However, in a similar way one can define a multivariate stochastic process $\mathbf{X}(t)$:

$$d\mathbf{X} = \mathbf{f}(\mathbf{X}) + \underline{\mathbf{g}}(\mathbf{X})d\mathbf{B}, \tag{2.21}$$

where \mathbf{f} is a vector and $\underline{\mathbf{g}}$ a matrix. With $g_{ij} \neq 0$ for $i \neq j$ one models correlated noise sources in the system. As in the one-dimensional case, formula 2.21 requires an interpretation. When choosing the Ito interpretation, one obtains the corresponding Ito-Lemma:

$$dh(\mathbf{X}) = (\mathbf{f}(\mathbf{X}) \cdot \nabla h(\mathbf{X}) + \frac{1}{2}\underline{\mathbf{g}}(\mathbf{X})\underline{\mathbf{g}}^T(\mathbf{X}) : [\nabla \otimes \nabla h(\mathbf{X})])dt + \underline{\mathbf{g}} : (\nabla h(\mathbf{X})d\mathbf{B}(t)^T). \tag{2.22}$$

Next, we introduce a second description of stochastic processes, which does not depend upon interpretation.

2.1.4. Fokker-Planck equation

In ordinary calculus, once we obtain a solution of an ordinary or partial differential equation, we essentially know the exact behavior of our system: its behavior is deterministic. On the other hand, the solution of an SDE is a highly irregular stochastic process (as Brownian motion itself), which follows different trajectories for different realizations. So,

when our system is noisy, we cannot expect to obtain certainty of its behavior, but we may ask for the probability for a certain event to happen. Assume $p(\mathbf{x}, t | \mathbf{x}_0, t_0)$ to be the probability density of the stochastic process \mathbf{X} , which solves an Ito SDE and fulfills an initial condition $\mathbf{X}(t_0) = \mathbf{x}_0$. Furthermore, let h be a smooth function with compact support. Then, interchanging integral and time derivative gives [59]:

$$\partial_t \langle h(\mathbf{X}(t)) \rangle = \int h(\mathbf{x}) \partial_t p(\mathbf{x}, t | \mathbf{x}_0, t_0) d\mathbf{x}. \quad (2.23)$$

Using Ito's formula (2.22) and $\langle d\mathbf{B} \rangle = 0$, an alternative expression can be derived:

$$\begin{aligned} \partial_t \langle h(\mathbf{X}(t)) \rangle &= \left\langle \frac{dh(\mathbf{X})}{dt} \right\rangle = \langle \mathbf{f}(\mathbf{X}) \cdot \nabla h(\mathbf{X}) + \frac{1}{2} \underline{\mathbf{g}}(\mathbf{X}) \underline{\mathbf{g}}^T(\mathbf{X}) : [\nabla \otimes \nabla h(\mathbf{X})] \rangle \\ &= \int [\mathbf{f}(\mathbf{x}) \cdot \nabla h(\mathbf{x}) + \frac{1}{2} \underline{\mathbf{g}}(\mathbf{x}) \underline{\mathbf{g}}(\mathbf{x})^T : [\nabla \otimes \nabla h(\mathbf{x})]] p(\mathbf{x}, t | \mathbf{x}_0, t_0) d\mathbf{x}. \end{aligned} \quad (2.24)$$

The operator $A[h] := \mathbf{f} \cdot \nabla h + \frac{1}{2} \underline{\mathbf{g}} \underline{\mathbf{g}}^T : [\nabla \otimes \nabla h]$ is called the generating operator for the stochastic process \mathbf{X} . Its conjugate is easily obtained by partial integration (Green's identities for higher dimensions): $A^*[h] = -\nabla \cdot (\mathbf{f}h) + \frac{1}{2} \nabla \otimes \nabla : (\underline{\mathbf{g}} \underline{\mathbf{g}}^T h)$. Making use of Eq. (2.23) and (2.24) and applying the definition of the conjugate operator, gives:

$$\int h \partial_t p dt = \int A[h] p dx = \int h A^*[p] dx.$$

Since h is arbitrary, we obtain the celebrated Fokker-Planck equation (FPE):

$$\dot{p}(\mathbf{x}, t) = -\nabla \cdot (\mathbf{f}p) + \frac{1}{2} \nabla \otimes \nabla : [\underline{\mathbf{g}}(\mathbf{x}) \underline{\mathbf{g}}(\mathbf{x})^T p(\mathbf{x}, t | \mathbf{x}_0, t_0)], \quad (2.25)$$

which is a linear partial differential equation (PDE) of second order. The first term is typically called drift and the second term represents the diffusion. Now, whenever drift and diffusion are reasonably smooth, Eq. (2.25) together with an initial condition $p(\mathbf{x}_0, t_0 | \mathbf{x}_0, t_0) = \delta(0)$ determine a unique probability density p of the stochastic process \mathbf{X} . For its derivation we interpreted \mathbf{X} in the Ito sense. What is the corresponding FPE to the Stratonovich SDE? We calculate in one dimension for clarity. Using the transformed SDE (2.20) with $\alpha = 0.5$ and Eq. (2.25), after some algebra one obtains the corresponding Stratonovich FPE:

$$\dot{p}(t) = \partial_x [-fp + \frac{1}{2} g \partial_x (gp)]. \quad (2.26)$$

Hence, one advantage of the FPE is that the difference between Ito and Stratonovich is expressed in different formulae (2.25) and (2.26), i.e., in the order of differentiation.

Furthermore, we can interpret the Fokker-Planck equation in terms of transport. Indeed, p fulfills a continuity equation

$$\dot{p} = -\nabla \cdot \mathbf{J}, \quad J_i := f_i p - \frac{1}{2} \sum_j \partial_j g_{ij} p,$$

with probability flux \mathbf{J} . For $g = \sqrt{2D}$ and $f = 0$ we obtain Fick's law with diffusion constant D . The function f can be interpreted as streaming velocity. There are neither sources nor sinks such that the overall density $\int p dx$ is conserved.

2.1.5. Shot noise

In this section, we introduce the notion of *shot noise*. This is a stochastic process with a finite number of jumps (or shots) in finite time. Shot noise processes have been used in various fields of science such as physics, biology, or finance [60]. In Ref. [61], a shot noise process has been used to model the energy depot of an active Brownian walker. The latter will be explained in Sec. 2.2.2. In Ref. [62], it is shown that shot noise occurs in electric conductors as quantized charges. In neurology, shot noise is a natural choice to model spikes of firing neurons. It has been claimed that using shots as input information for single neurons is a more accurate assumption than Brownian input [63]. In Chap. 5, we will apply a jump-diffusion model to bacterial motion.

Poisson process

When introducing the erratic motion of a small particle in a fluid as Brownian motion, we identified the numerous, independent kicks of small fluid particles as microscopic reason for it. Mathematically speaking, the sum of independent random contributions leads to Gaussian increments by virtue of the central limit theorem. This theorem can be violated, for instance, when the variances of the underlying random variables diverge. A typical example is the so-called Levy walk, where power-law distributions of the microscopic noise sources lead to large jumps in the resulting stochastic process [64]. Another source of violation of the central limit theorem is the absence of sufficient stochastic kicks at every instance of time. Here, we consider a process $Q(t)$ which exhibits maximally one strong random kick in the time interval $[t, t + \Delta t]$ with probability $\lambda \Delta t$ independent of time t . When performing the limit $\Delta t \rightarrow 0$, the fact that shots independently occur at two consecutive time intervals means that the process instantaneously “forgets” about what happened before. Hence, it is *memoryless* meaning that the distribution p of the waiting time T does not depend on how long the waiting has already been:

$$p(T > t + s | T > t) = p(T > s). \quad (2.27)$$

One can show that the only continuous memoryless distribution is the exponential distribution with mean λ . If we now count the shots N after a time t , it follows the Poissonian

distribution [65]:

$$P^{t\lambda}(N) = \frac{(\lambda t)^N}{N!} \exp(-\lambda t). \quad (2.28)$$

Then, we can define the *Poisson process* with rate λ :

$$Q(t) = \sum_{i=1}^{N^{\lambda t}} \beta_i, \quad (2.29)$$

where β_i are the shot amplitudes. These are identically, independently distributed stochastic variables with distribution P_β . $N^{\lambda t}$ is a Poissonian-distributed random variable with mean λt . Note that Q is non-continuous due to its jumps in contrast to Brownian motion, which is continuous. It is straight forward to generalize Q to higher dimensions where in each dimension the process is again a one-dimensional Poisson process. In order to calculate the moments of Q we can make use of Wald's equation [66]:

$$\langle [Q(t) - Q(0)]^n \rangle = \langle N^{\lambda t} \rangle \langle \beta^n \rangle = \lambda t \langle \beta^n \rangle. \quad (2.30)$$

This is a remarkable result. The moments of Q scale linearly with t for *each* power n . This is in contrast to Brownian motion, where the moments scale like $t^{\frac{n}{2}}$ [see Eq. (5.14)]. We will exploit this unique scaling behavior in Chap. 5. Nevertheless, the Poisson process has the property of independent increments in common with Brownian motion, which enables the definition of another white noise process.

Shot noise as formal derivative of the Poisson process

The process symbolically defined by $q(t) := dP/dt$ can be written as a sum of δ -functions:

$$q(t) = \sum_{i=1}^{N^{\lambda t}} \beta_i(\theta) \delta(t - t_i), \quad (2.31)$$

with the stochastic variables β_i as before and the number of shots $N^{\lambda t}$, which is Poissonian distributed. As for the Gaussian white noise, one can calculate the first two moments. Assuming $\langle \beta_i \rangle = 0$, one first obtains:

$$\langle q(t) \rangle = \left\langle \sum_{i=1}^{N^{\lambda t}} \beta_i \delta(t - t_i) \right\rangle = 0.$$

Furthermore, since β_i and β_j for $i \neq j$ are uncorrelated, one calculates for $s \leq t$:

$$\langle q(t)q(s) \rangle = \sum_{i=1}^{N^{\lambda t}} \beta_i^2 \delta(t - t_i) \delta(s - t_i) = \sum_{i=1}^{N^{\lambda t}} \beta_i^2 \delta(t - s) \delta(t - t_i).$$

Hence, q is δ -correlated, for which reason it is called white. Due to its δ -function definition one can symbolically write $q(t) \sim \frac{1}{dt}$ in contrast to Gaussian white noise, which scales like $\xi(t) \sim \frac{1}{\sqrt{dt}}$.

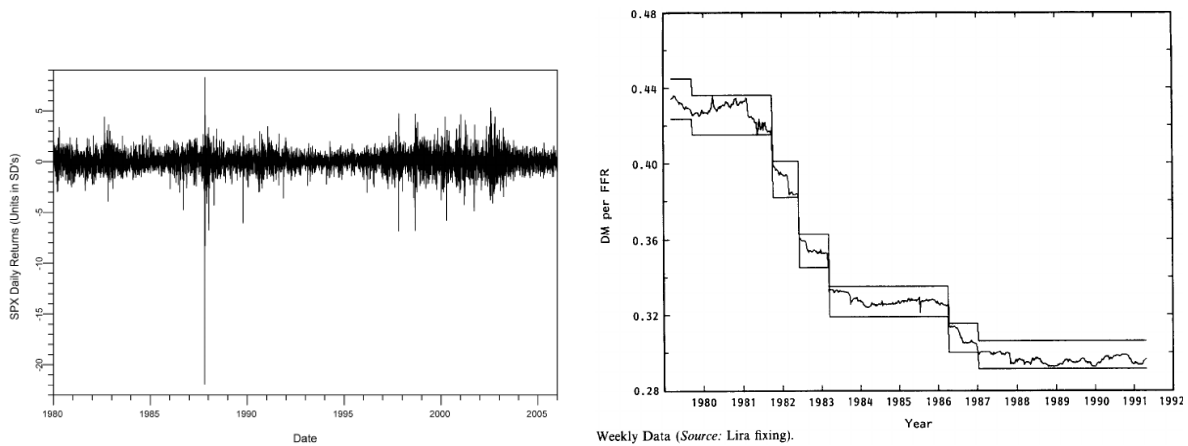


Figure 2.2.: Left: Extracted from [67]. Daily normalized changes of the American *S&P500* Stock index $dS = (S(n+1) - S(n))/S(n)$ during 1980 and 2005. One clearly recognizes huge shots in the time series. Right: Extracted from [68]. The exchange rate of Deutsche Mark vs. French Franc from 1980 until 1992. Prominent steps are recognizable.

Jump-diffusion equation

When modeling the temporal behavior of the stock exchange, one might identify three main effects. First, there are several sellers and buyers at any small time interval. They may be considered as essentially independent and lead to fluctuations of the stock price well-described by Brownian motion. In addition, due to global economy trends the stock may follow a drift. Both effects together would be well described by a stochastic diffusion equation (2.18), and, indeed, the latter is a common tool in stochastic financing [60]. However, sometimes there are unexpected blows, which may be caused by environmental catastrophes, unexpected political decisions, or powerful investors taking the decision to buy or sell many stocks at a time [67]. As examples, we see in Fig. 2.2 on the left the daily normalized changes of the American *S&P500* Stock index during 1980 and 2005 and, on the right, the exchange rate of the German and French currency during 1980 and 1992. Obviously, both processes are subjects to large jumps, which cannot result from Brownian motion with drift alone.

To account for such a situation, one can add a shot noise term to the regular drift-diffusion terms [67, 68]:

$$d\mathbf{x} = \mathbf{f}(\mathbf{X})dt + \underline{\mathbf{g}}(\mathbf{X})d\mathbf{B} + d\mathbf{Q} = [\mathbf{f}(\mathbf{X}) + \underline{\mathbf{g}}(\mathbf{X})\boldsymbol{\xi} + \mathbf{q}]dt \quad (\text{Ito}). \quad (2.32)$$

Following a similar procedure as in Sec. 2.1.4, one deduces the corresponding dynamic

equation for the probability measure p described by Eq. (2.32):

$$\dot{p}(\mathbf{x}, t) = -\nabla \cdot (\mathbf{f}p) + \frac{1}{2} \nabla \otimes \nabla \cdot [\underline{\mathbf{g}}(\mathbf{x}) \underline{\mathbf{g}}(\mathbf{x})^T p(\mathbf{x}, t)] + \int [p(\mathbf{x} - \mathbf{y}, t) \lambda(\mathbf{x} - \mathbf{y}) - p(\mathbf{x}, t) \lambda(\mathbf{x})] P_\beta(\mathbf{y}) d\mathbf{y}. \quad (2.33)$$

The last term can be interpreted as probability source and sink. The source term (positive contribution) integrates over all situations, in which the process jumps from states $\mathbf{x} - \mathbf{y}$ to \mathbf{x} , whereas the sink (negative contribution) refers to the situation, when the process jumps away from \mathbf{x} with rate λ . In general, λ can be a function of \mathbf{x} . An integration over the whole space yields

$$\begin{aligned} \int d\mathbf{x} \int d\mathbf{y} [p(\mathbf{x} + \mathbf{y}) \lambda(\mathbf{x} + \mathbf{y}) - p(\mathbf{x}) \lambda(\mathbf{x})] P_\beta(\mathbf{y}) = \\ \int d\mathbf{y} P_\beta(\mathbf{y}) \int d\mathbf{x} [p(\mathbf{x} + \mathbf{y}) \lambda(\mathbf{x} + \mathbf{y}) - p(\mathbf{x}) \lambda(\mathbf{x})] = 0, \end{aligned}$$

where we switched integrals and exploited translational invariance. Since also the divergence part vanishes when integrating Eq. (2.33), we have shown that the total probability mass is conserved.

As an example, we present the Ornstein-Uhlenbeck equation in one dimension:

$$\dot{\eta} = -\gamma(\eta - \eta_0) + q(t), \quad (2.34)$$

where η_0 is the rest state of the process. After the occurrence of a shot, the process equilibrates back to η_0 with typical time $1/\gamma$. When defining $\tilde{\eta} := \eta - \eta_0$, we see that Eq. (2.34) is equivalent to Eq. (2.3) up to different noise sources. The OU-process with Gaussian white noise as noise source is in fact the original Ornstein-Uhlenbeck equation [59]. We obtain the analogous solution to Eq. (2.8):

$$\eta(t) = \eta_0 + \eta(0) \exp(-\gamma t) + \int_0^t \exp[-\gamma(t - t')] q(t') dt'.$$

In Fig. 2.3 we see numerical realizations of the Ornstein-Uhlenbeck process with Gaussian white noise, with shot noise, and with both processes as noise sources.

Time varying shot rate λ

In practical situations the rate λ might be a function of time, $\lambda(t) > 0$. Then we can construct a Poisson process in a similar way as before by setting for each time interval $[t, t + \Delta t]$ the probability for a shot to $\Delta t \lambda(t)$. Let U_i be stochastic variables, which assume the value 1 with probability p and the value 0 with probability $1 - p$. Since we can write the Poisson process as limit of an infinite series of such random variables, we can calculate:

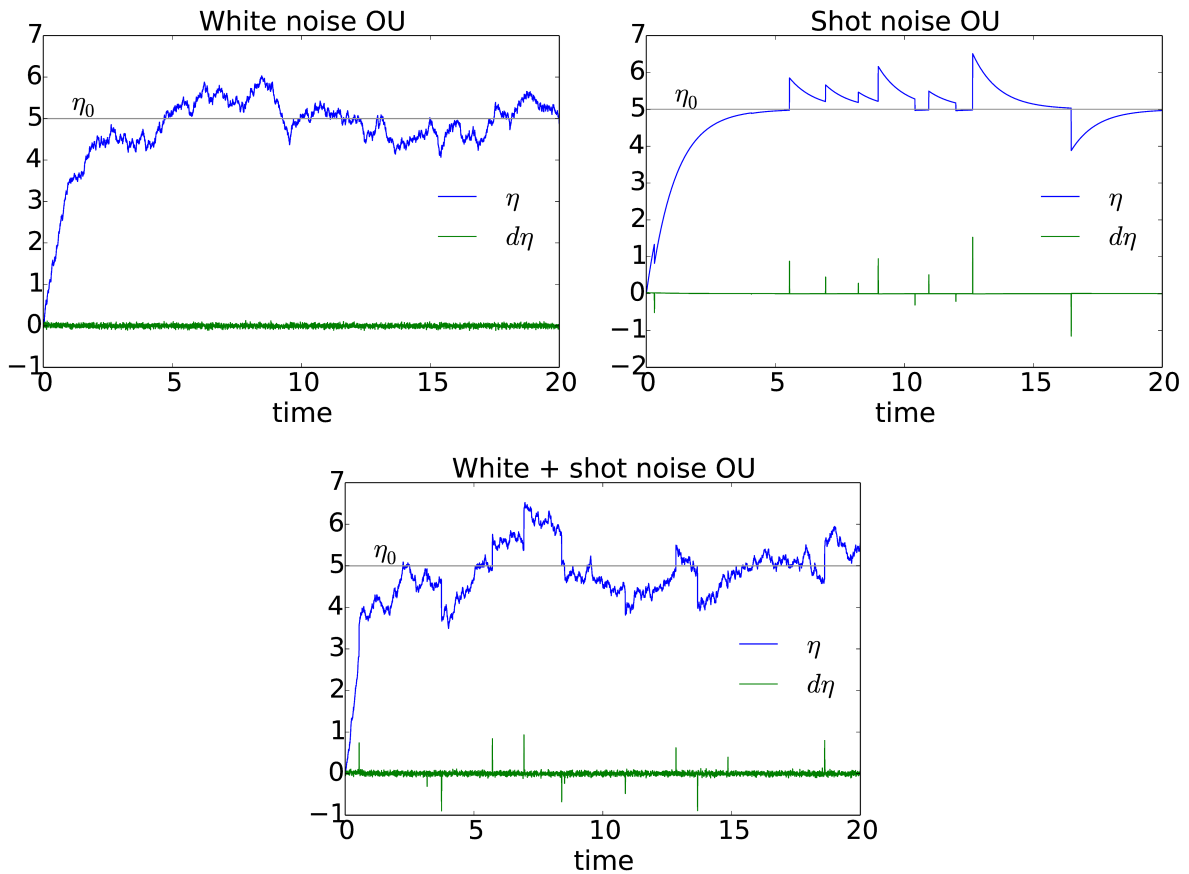


Figure 2.3.: Simulation of Ornstein-Uhlenbeck processes η as in Eq. (2.34) with various noise sources. The blue graph refers to η , whereas the green one to its finite differential $d\eta = \eta(t + 0.005) - \eta(t)$. Top left: Gaussian white noise as noise source. Parameters are: $\eta_0 = 5$, $\eta(0) = 0$, diffusion $D = 0.5$. Top right: Shot noise as noise source. Parameters are $\eta_0 = 5$, $\eta(0) = 0$, $\lambda = 0.5$, β uniformly distributed in $[-2, 2]$. Bottom: Shot and Gaussian white noise as noise sources. Parameters: $\eta_0 = 5$, $\eta(0) = 0$, $\lambda = 0.5$, β uniformly distributed in $[-1, 1]$, diffusion $D = 0.125$.

$$\langle Q^{\lambda(t)}(t) \rangle = \lim_{\Delta t \rightarrow 0} \left\langle \sum_{i=0}^{t/\Delta t} \beta_i U_i^{\Delta t \lambda(t)} \right\rangle = \lim_{\Delta t \rightarrow 0} \sum_{i=0}^{t/\Delta t} \langle \beta \rangle \langle U_i^{\Delta t \lambda(t)} \rangle = \langle \beta \rangle \lim_{\Delta t \rightarrow 0} \sum_{i=0}^{t/\Delta t} \lambda(t) \Delta t = \langle \beta \rangle \int_0^t \lambda(s) ds.$$

A similar calculation reveals:

$$\langle [Q^{\lambda(t)}(t)]^n \rangle = \langle \beta^n \rangle \int_0^t \lambda(s) ds. \quad (2.35)$$

We see that we recover Eq. (2.30) when $\lambda(t)$ is constant. The Poisson process with time-dependent $\lambda(t)$ is also called *inhomogeneous Poisson process*.

2.1.6. Kramers-Moyal coefficients

Here, we present another method to describe a stochastic process. For this approach, its probability density is expressed by a possibly infinite series of conditioned moments, also referred to as Kramers-Moyal coefficients. We will show how the connection of this representation with the Fokker-Planck framework is established and how the moments can be used in experiments.

Let $p(x, t)$ be the probability density of a stochastic process at time t and $p(x, t + \Delta t | x - \Delta x, t)$ the conditioned probability density for x at time $t + \Delta t$ conditioned on the state $x - \Delta x$ at time t . Integrating over all possible conditions $x - \Delta x$ yields [58]:

$$\begin{aligned} p(x, t + \Delta t) &= \int p(x, t + \Delta t | x - \Delta x, t) p(x - \Delta x, t) d\Delta x \\ &= \int \sum_{n=0}^{\infty} \frac{(-1)^n}{n!} (\partial_x)^n \Delta x^n p(x + \Delta x, t + \Delta t | x, t) p(x, t) d\Delta x, \end{aligned} \quad (2.36)$$

where we performed a backward Taylor expansion for the last equation. Next, we introduce the finite conditioned moments for a stochastic process X with density p :

$$m_{\Delta t}^n(x, t) := \left\langle \frac{[X(t + \Delta t) - X(t)]^n}{\Delta t} \middle| X(t) = x \right\rangle \quad (2.37)$$

Then, the moments can be written by means of the density p :

$$m_{\Delta t}^n(x, t) = \frac{1}{\Delta t} \int (\Delta x)^n p(x + \Delta x, t + \Delta t | x, t) d\Delta x \quad (2.38)$$

Upon interchanging summation and integration in Eq. (2.36) and substituting the last equation in it, we obtain:

$$p(x, t + \Delta t) = p(x, t) + \sum_{n=1}^{\infty} \frac{(-1)^n (\partial_x)^n}{n!} m_{\Delta t}^n(x, t) \Delta t p(x, t), \quad (2.39)$$

The term $p(x, t)$ is the zeroth order term from the Taylor expansion. Dividing Eq. (2.39) by Δt on both sides and taking the limit $\Delta t \rightarrow 0$, leads to the celebrated *Kramers-Moyal expansion*:

$$\dot{p}(x, t) = \sum_{n=1}^{\infty} \frac{1}{n!} (-\partial_x)^n [m^n(x, t)p(x, t)] \quad (2.40)$$

with

$$m^n(x, t) := \lim_{\Delta t \rightarrow 0} m_{\Delta t}^n(x, t). \quad (2.41)$$

Comparing this result with the Fokker-Planck equation (2.25) associated to the Ito SDE (2.18) in one dimension, readily gives:

$$m^1(x, t) = f(x) \quad (2.42)$$

$$m^2(x, t) = g(x)^2 \quad (2.43)$$

$$m^n(x, t) = 0 \quad \text{for } n > 2. \quad (2.44)$$

Interestingly, it turns out that the case, in which all components but the first second vanish, is a very general one. More precisely, the *Pawula theorem* states that if one of the components for $n > 2$ is zero, then likewise are all the others for $n > 2$. In Chap. 5 we will calculate (absolute) finite conditioned moments for shot noise, Gaussian white noise, and the sum of both.

2.2. Active Motion

In this section, we introduce the concept of active motion, which has recently been extensively discussed in the context of statistical mechanics. First, we motivate the concept, then we introduce a model to describe it, and finally we discuss a typical system with collective motion of active particles.

2.2.1. Active motion in biology and synthetic systems

The motion of a particle can be called *active*, when energy from the environment is transformed to generate the motion. Hence, by definition, there is a steady energy input such that the system never reaches equilibrium and the phenomenon needs to be studied in the context of *far-from-equilibrium statistical physics*. Consequently, familiar properties known from equilibrium systems no longer hold. For example, the *fluctuation-dissipation theorem* is violated. As a consequence, the diffusion constant is no longer given by the Stokes-Einstein relation (2.14).

Living organisms are standard examples for active particles. They metabolize nutrients and use the resulting energy to move actively. On the micron scale many bacteria move by virtue of one or several flagella attached to their body. These flagella are helices, which effectively work like a corkscrew to propel the organism forward [45] or backward [69]. Eukaryotic cells like *Dictyostelium discoideum* typically crawl on tissue by protrusion and retraction based on transformations of their extracellular matrix [70]. Parasites like *Trypanosoma brucei* move by a beating eukaryotic flagellum attached along the cell body [71]. On larger length scales, fish move by beating their elastic body. Birds flap their wings to move up- and forward. Apparently, active motion is ubiquitous in nature, which has inspired scientists to imitate it with synthetic matter [72]. Prominent examples are colloidal particles in rod-like or round shape, which actively propel forward due to thermo-, electro- or diffusiophoretic effects [9, 14]. Covered by two different materials on each of their half sides, they create temperature and chemical gradients or electric fields along their surfaces. This leads to pressure gradients in the ambient fluid, in which colloids swim, and eventually to active phoretic motion (more information and references in Chap. 4).

In equilibrium, work cannot be extracted from systems with many particles and there are neither fluxes nor huge density fluctuations. This may change in assemblies of active particles. In intriguing experiments Leonardo et al. [73] showed that an asymmetrically shaped rotor in a bath of randomly moving bacteria rotates, a phenomenon which is forbidden by the second law of thermodynamics in equilibrium (e.g., for dead particles). In equilibrium, the number fluctuations ΔN typically scale with the overall particle number N as $\Delta N \sim N^\alpha$ with $\alpha = 0.5$ due to the central limit theorem. *Large* or even *giant number fluctuations* refer to systems with $\alpha > 0.5$. Such a situation has been observed in experiments of vibrated rods [74] or with gliding bacteria [75]. In both, a short-ranged alignment mechanism between the rod-shaped particles can be observed and stems from friction during collisions. However, as we will see for the example of self-propelled hard discs (Sec. 2.2.3) alignment, is not a necessary condition for phase separation and large density fluctuations to show up.

We proceed by presenting a basic model for a self-propelling or active particle.

2.2.2. A model for an active swimmer

In the year 2000 a model was proposed for *active Brownian motion* introducing an internal energy depot [76]. The activity was introduced by a novel friction term, which for slow velocity \mathbf{v} accelerates and for large velocity breaks. For certain parameters this was shown to lead to persistent motion. Recently, a simpler version of such an approach to model *active motion* has become increasingly popular. First, one separates the directional motion from speed assuming that their fluctuations are uncorrelated [77]. This assumption holds only because of the out-of-equilibrium nature of active motion, otherwise rotational and translational fluctuations would be coupled. Then, the underdamped

dynamics of an active particle can be written as:

$$\dot{\mathbf{r}} = \mathbf{v}, \quad (2.45)$$

$$M\dot{\mathbf{v}} = -\gamma(\mathbf{v} - v_0\mathbf{e}) - \nabla U(\mathbf{r}) + \boldsymbol{\xi}, \quad (2.46)$$

$$\dot{\mathbf{e}} = \mathbf{e} \times \boldsymbol{\mu} \quad (S), \quad (2.47)$$

Here, $\boldsymbol{\xi}$ is the translational and $\boldsymbol{\mu}$ the rotational noise source, both of which being white noise processes as introduced in Sec. 2.1.2 or Sec. 2.1.5. The (S) in the last equation indicates that this multiplicative stochastic differential equations is interpreted in the Stratonovich sense. Furthermore, v_0 is the speed of the object, which we assume as constant within this section. \mathbf{e} is the active moving direction of the particle with $|\mathbf{e}| = 1$, M is its mass, and U is an external potential. We can interpret Eq. (2.46) as Ornstein-Uhlenbeck equation with separate speed and orientation. For microscopically small particles, such as bacteria and colloids, the mass is small and friction dominates. In this limit, one neglects $M\dot{\mathbf{v}}$ to obtain the overdamped dynamic equations for an active particle:

$$\dot{\mathbf{r}} = v_0\mathbf{e} - \nabla U(\mathbf{r}) + \boldsymbol{\xi} \quad (2.48)$$

$$\dot{\mathbf{e}} = \mathbf{e} \times \boldsymbol{\mu} \quad (S). \quad (2.49)$$

The Eq. (2.49) contains multiplicative noise. We chose the Stratonovich interpretation since the ordinary differential rules apply and *only* in this case the normalization condition $|\mathbf{e}| = 1$ is guaranteed:

$$\partial_t(\mathbf{e} \cdot \mathbf{e}) = 2\dot{\mathbf{e}} \cdot \mathbf{e} = 2(\mathbf{e} \times \boldsymbol{\mu}) \cdot \mathbf{e} = 0 \quad (2.50)$$

Furthermore, one can show that in two dimensions, when introducing the directional angle α with $\mathbf{e} = [\cos(\alpha), \sin(\alpha)]$, Eq. (2.49) becomes [78]:

$$\dot{\alpha} = \mu, \quad (2.51)$$

i.e., additive noise with no need for stochastic interpretation. We want to study two cases. First, we assume μ to be Gaussian white noise with rotational diffusion constant D_{rot} . For the second case we set $\mu(t) = q(t)$ with q being shot noise as introduced in section 2.1.5. It is defined by its shot rate λ and the shot amplitude β , which we assume to be the uniform distribution on the interval $[0, 2\pi)$. The active Brownian random walk can be associated with self-propelling colloids, whereas the second models approximately a run-and-tumble random walk of a Bacterium like *E. coli*, which will be discussed in Sec. 3.2.1.

In Fig. 2.4 we plot two realizations of a Brownian active walker and the shot noise walker. The microscopic dynamics are apparently very different, however, the large

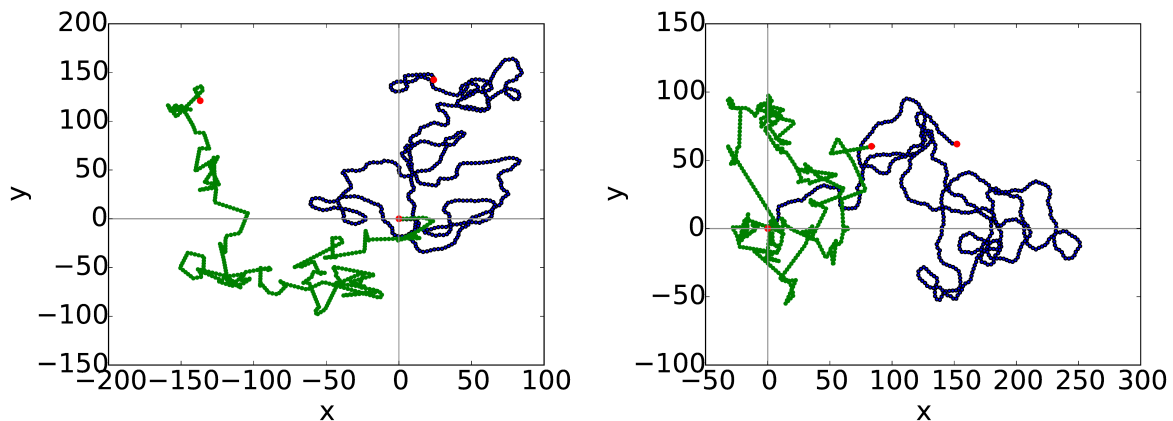


Figure 2.4.: Two realizations of a Brownian active walker (blue) and a shot noise walker (green). Red points are start and end point. The effective diffusion D_{eff} is chosen to be the same.

scale behavior looks similar. In the following, this general observation is quantified by calculating the mean square displacement of the two walkers. The Fokker-Planck equation corresponding to Eq. (2.49) is given by

$$\dot{p}(\mathbf{e}, t) = D_{\text{rot}} \mathcal{R}^2 p \quad (2.52)$$

with $\mathcal{R} := \mathbf{n} \times \partial_{\mathbf{n}}$. As for the derivation of the mean square displacement of a passive walker [see Eq. (2.13)], we first need to calculate the velocity autocorrelation function:

$$\langle \mathbf{v}(t) \cdot \mathbf{v}(t') \rangle = v_0 \langle \mathbf{e}(t) \cdot \mathbf{e}(t') \rangle \quad (2.53)$$

Taking the time derivative and making use of Eq. (2.52) one obtains:

$$\partial_t \langle \mathbf{e}(t) \cdot \mathbf{e}(t') \rangle = \int \int \mathbf{e} \cdot \mathbf{e}' \dot{p}(\mathbf{e}, t) p(\mathbf{e}', t') d\mathbf{e} d\mathbf{e}' = D_{\text{rot}} \int \int \mathbf{e} \cdot \mathbf{e}' \mathcal{R}^2 p(\mathbf{e}, t) p(\mathbf{e}', t) d\mathbf{e} d\mathbf{e}' \quad (2.54)$$

Next, we apply two times partial integration and use the formula $\mathcal{R}^2 \mathbf{e} = -(d-1)\mathbf{e}$:

$$\partial_t \langle \mathbf{e}(t) \cdot \mathbf{e}(t') \rangle = D_{\text{rot}} \int \int -(d-1) \mathbf{e} \cdot \mathbf{e}' p(\mathbf{e}, t) p(\mathbf{e}', t) d\mathbf{e} d\mathbf{e}' = -D_{\text{rot}} (d-1) \langle \mathbf{e}(t) \cdot \mathbf{e}(t') \rangle. \quad (2.55)$$

This equality poses a linear ordinary differential equation, which, together with the initial condition $\langle \mathbf{e}(t') \cdot \mathbf{e}(t') \rangle = 1$, is solved to

$$\langle \mathbf{e}(t) \cdot \mathbf{e}(t') \rangle = \exp[-(d-1)D_{\text{rot}}(t-t')]. \quad (2.56)$$

Hence, $\tau_p := \frac{1}{(d-1)D_{\text{rot}}}$ can be interpreted as typical persistence time of the particle. Plugging Eq. (2.56) in Eq. (2.12), we obtain for the mean square displacement:

$$d_m^2(s, t) = \langle |\mathbf{r}(t) - \mathbf{r}(s)|^2 \rangle = 2v_0^2 \tau_p \left[(t - s) + \tau_p (-1 + \exp[-\tau_p^{-1}(t - s)]) \right]. \quad (2.57)$$

There are two time regimes: When expanding Eq. (2.57) for $\frac{t-s}{\tau_p} \ll 1$, we obtain $d_m^2 \sim (t - s)^2$, while for large $t - s$ we have

$$d_m^2 = 2\tau_p(t - s)v_0^2 \quad (2.58)$$

Hence, the motion of an active Brownian particle is ballistic for short times and becomes diffusive for time intervals with $t - s \gg \tau_p$. Based on this observation, we can define an *effective diffusion constant*

$$D_{\text{eff}} = \lim_{t \rightarrow \infty} \frac{d_m^2(0, t)}{2td} = \frac{v_0^2}{(d-1)dD_{\text{rot}}}. \quad (2.59)$$

However, even in stationary state ($s \rightarrow \infty, t \rightarrow \infty$) the ballistic component plays a crucial role since $d_m^2(s, t) = d_m^2(t - s)$. This is in contrast to the underdamped Brownian walker with friction as can be seen in Eq. (2.13). There, the initial energy input in form of $\mathbf{v}(0)$ is dissipated after some time (in the overdamped limit this time even vanishes) and the motion becomes *purely* diffusive in stationary state. In the following section, we will see that this difference has striking implications for the collective behavior of active particles.

When the noise source μ in Eq. (2.49) is shot noise, we can, by a similar calculation as for the Gaussian case, derive an effective rotational diffusion constant. In Sec. 3.2.4 we present a somewhat different ansatz, which gives the result:

$$D_{\text{eff}} = \frac{v_0^2}{d\lambda}.$$

In Fig. 2.4 we choose the parameters such that the effective diffusion turns out to be the same. One clearly sees the analogy of both active motions in the long time behavior.

2.2.3. Collective motion of active particles

In 2012 the announcement of phase separation in a system of active particles without alignment or attraction by Ref. [34] attracted considerable attention of the statistical physics community. The theoretical system consists of active particles in disc shape, which move randomly through the two-dimensional space occasionally hitting each other. During such collisions they interact via a repulsive potential U , which leads to no or small overlaps between particles. The observed phase separation typically consists of

one big cluster with nearly hexagonal structure and a gas state with low particle density. Furthermore, large number fluctuations were reported, which is a clear signal for the system being out of equilibrium.

What is the reason for the observed emergent structure in such a minimal system? As it turns out, the short-time ballistic motion of the active particles plays the decisive role here. To illustrate this, one can employ a time scale argument [21]. Assume a small conglomeration of particles, which just emerges due to fluctuations. When a particle swims into it, it gets stuck until it reorients out of the cluster. As discussed in the previous chapter, a typical time for random reorientation is $\tau_p = \frac{1}{D_{\text{rot}}}$, hence $t_{\text{out}} \sim \frac{1}{D_{\text{rot}}}$. On the other hand, the time for a second particle to run into a small nucleus and possibly block it can be estimated as $t_{\text{in}} \sim \frac{1}{\tilde{\rho}v_0}$ with $\tilde{\rho}$ being the particle density and v_0 their velocity. If the ratio

$$\frac{t_{\text{out}}}{t_{\text{in}}} = \frac{v_0\rho}{D_{\text{rot}}} \quad (2.60)$$

is very large, one expects cluster formation and possibly phase separation.

This is a remarkable statement. In the previous section, we introduced the effective diffusion for an active particle $D_{\text{eff}} = \frac{v_0^2}{d(d-1)D_{\text{rot}}}$ (Eq. (2.59)). Invoking the Stokes-Einstein relation (valid for equilibrium systems) diffusion is proportional to temperature $D_{\text{eff}} \sim T_{\text{eff}}$. Hence, we obtain $v_0^2 \sim T_{\text{eff}}$. Substituting this into Eq. (2.60), we obtain a seemingly paradox scaling: the larger the (effective) temperature, the *more* clustering! Typically, in equilibrium, increasing temperature leads to less order.

Hence, we have shown that the ballistic motion on short time scales of active particles may lead to clustering, thereby counteracting the diffusive character on long time scales of active motion. In particular, the notion of an “effective temperature” may be misleading. In 2014 this seemingly paradox scaling as well as the onset of phase separation was indeed confirmed experimentally [79]. Earlier in 2012, in experiments with a dilute suspension of active colloids a linear dependence of cluster size and active velocity of colloids was shown [14] and it was explained along the lines above. However, in Sec. 4.5.3 we show that in the dilute regime different arguments based on diffusiophoretic motion need to be considered to explain increasing cluster sizes with increasing activity.

The above argumentation is an explanation for the occurrence of phase separation, but it is not a theory. A series of publications [37–39, 80, 81] shed light on the observed phenomenology. In the following, we sum up a possible line of argumentation. One starts with Eqs. (2.48) and (2.49) for each of the N particles with $\boldsymbol{\mu}$ being Brownian white noise and U a repulsive interaction potential due to close neighboring particles. The associated Fokker-Planck equation reads:

$$\dot{\rho}(\mathbf{e}, \mathbf{r}, t) = -\nabla \cdot [\mathbf{F} + v_0\mathbf{e}\rho - D\nabla\rho] + \mathcal{R}^2\rho. \quad (2.61)$$

ρ is the one-particle probability density of some particle. The particles are assumed to be identical, for which reason we do not use indices. There are different ways to proceed

at this point. In Ref. [81] and [37] it is typically assumed that the interaction force \mathbf{F} acts along \mathbf{e} and depends on the particle density, $\mathbf{F} = \mathbf{F}(\rho)$, thus:

$$\dot{\rho}(\mathbf{e}, \mathbf{r}, t) = -\nabla \cdot [v(\rho)\rho\mathbf{e} - D\nabla\rho] + \mathcal{R}^2\rho \quad (2.62)$$

where v_0 is absorbed by the general speed function v . The reason for such a choice is obvious. As soon as a particle moves into a crowded region with high density, collisions occur, which reduce its moving speed. However, this phenomenological reasoning gives no explanation about how to choose the function $v(\rho)$. In Ref. [38] a more quantitative approach is proposed for two dimensions. First of all, in the overdamped regime forces translate directly in velocities because inertia is neglected. With this, it is shown that the force \mathbf{F} in Eq. (2.61) leads to a velocity in \mathbf{e} -direction such that:

$$v = v_0 - \tilde{\rho}\zeta \quad (2.63)$$

with directional anisotropy parameter:

$$\zeta := \int_0^\infty dr r [-\partial_r U(r)] \int_0^{2\pi} d\theta \cos(\theta) g(r, \theta). \quad (2.64)$$

Here, g is the conditioned probability to find two particles at a distance $r = |\mathbf{r} - \mathbf{r}'|$ with angle θ between \mathbf{e} and $\mathbf{r} - \mathbf{r}'$. Note that $g = \text{const}$ implies $\zeta = 0$. Hence, only an anisotropic density of neighbors around a given particle leads to a reduction of speed. Clearly, for an active particle it is more likely to find a neighbor in its front than in the back leading to a non-zero ζ .

To make further progress, one expands the particle density ρ in spherical harmonics:

$$\rho(\mathbf{r}, \mathbf{e}, t) = P_0(\mathbf{r}, t) + \mathbf{P}_1(\mathbf{r}, t) \cdot \mathbf{e} + \mathbf{P}_2(\mathbf{r}, t) : (\mathbf{e} \otimes \mathbf{e} - \mathbb{1}/d) + O(\mathbf{P}_3). \quad (2.65)$$

with local density $P_0(\mathbf{r}, t) = \int \rho(\mathbf{e}, \mathbf{r}, t) d\mathbf{e}$, the polar $\mathbf{P}_1(\mathbf{r}, t) = \int \mathbf{e} \rho d\mathbf{e}$ and the nematic $\mathbf{P}_2(\mathbf{r}, t) = \int (\mathbf{e} \otimes \mathbf{e} - \frac{\mathbb{1}}{d}) \rho d\mathbf{e}$ order parameter. Integrating Eq. (2.62) over \mathbf{e} yields:

$$\dot{P}_0 = -\nabla \cdot (v\mathbf{P}_1) + D\nabla^2 P_0. \quad (2.66)$$

Multiplying Eq. (2.62) with \mathbf{e} and integrating over it gives:

$$\dot{P}_1 = -\frac{1}{d}\nabla \cdot (v\mathbf{P}_0) - (d-1)D_{\text{rot}}P_1 + D\nabla^2 P_1 - \nabla v\mathbf{P}_2. \quad (2.67)$$

Up to now, no approximations have been applied. After long times we assume P_1 and P_2 to have reached a stationary state, such that we neglect the time derivatives \dot{P}_1 and \dot{P}_2 . To close the equations, one also needs to discard gradients of \mathbf{P}_1 and of \mathbf{P}_2 . This is a strong approximation, which might fail in very dense regions, i.e., clusters. However,

with this approximations one can solve for \mathbf{P}_1 in Eq. (2.67) and substitute it in Eq. (2.66) to obtain:

$$\dot{P}_0 = \nabla \cdot \left[v(\tilde{\rho}) \nabla \left(\frac{v(\tilde{\rho})}{d(d-1)D_{\text{rot}}} P_0 \right) + D \nabla P_0 \right] \quad (2.68)$$

$$= \nabla \cdot \left[D + \frac{(v_0 - P_0 \zeta)(v_0 - 2P_0 \zeta)}{2D_{\text{rot}}} \right] \nabla P_0. \quad (2.69)$$

For the last equation, Eq. (2.63) is substituted, where the global density $\tilde{\rho}$ Eq. (2.63) was replaced by the local one $P_0(\mathbf{r})$. This assumption might be true when P_0 does not vary strongly, for example, before the onset of an instability at nearly homogeneous particle density. If one is not convinced by this assumption, one can still consider $v \approx v_0 - \zeta P_0$ as a first order approximation of a possibly non-linear speed function v . Performing a linear stability analysis of the homogeneous ground state $P_0(\mathbf{r}) = \tilde{\rho}$, we obtain as instability condition for the active velocity $v_- < v_0 < v_+$:

$$v_{+-} = 1.5\zeta\tilde{\rho} \pm \sqrt{\frac{1}{4}\zeta^2\tilde{\rho} - 2DD_{\text{rot}}}. \quad (2.70)$$

Hence, there is only an instability when $\frac{1}{4}\zeta^2\tilde{\rho} - 2DD_{\text{rot}} > 0$. We draw two conclusions from this result. First, the overall density for a given ζ needs to be sufficiently large compared to the noise for an instability to occur. Second, the active velocity v_0 needs to be chosen in the right parameter range: As predicted by the time scale argument above, it needs to be sufficiently large. On the other hand, too large v_0 prevents an instability.

Chemotaxis and diffusiophoresis

Having reviewed the statistical physics of active motion, we now draw our attention to the main topic of this thesis, which is *chemotaxis*. The terminus originally is used for cells and refers to their directed motion along a chemical gradient. Chemotaxis is based on a complex biomolecular signal transduction within the cell, which we will roughly introduce in Sec. 3.2.2. Recently, the terminus chemotaxis has also been used in the context of colloidal, i.e., synthetic particles, which move along chemical gradients. In this case, the reason is found to be of physical origin, namely diffusiophoresis, which will be discussed in Sec. 3.3.

We start this chapter with a coarse-grained model for chemotaxis.

3.1. Macroscopic perspective: Keller-Segel model

We consider an assembly of cells. In Sec. 2.2.2 we have seen that their active motion is diffusive on large time scales. Hence, a diffusive flux $J_D = -D_{\text{eff}}\nabla\rho$ with diffusion constant D_{eff} , as in Eq. (2.57), is expected. ρ denotes the bacterial density. Furthermore, we consider a chemotactic flux along the chemical gradient $J_c = \zeta\rho\nabla c$, where c represents the concentration of the chemical, which can be an attractant ($\zeta > 0$) or a repellent ($\zeta < 0$). Assuming the total number of cells to be conserved, one obtains:

$$\dot{\rho} = D_{\text{eff}}\nabla^2\rho - \zeta\nabla\cdot\rho\nabla c. \quad (3.1)$$

The concentration field c develops according to a diffusion equation. We assume that the cells produce the chemical themselves with rate k and that the chemical degrades with rate γ . One obtains:

$$\dot{c} = D_c\nabla^2c + k\rho - \gamma c. \quad (3.2)$$

Typically, D_c is much larger than the effective diffusion of cells, i.e., $D_{\text{eff}} \ll D_c$ because the molecules of the chemical c are supposed to be much smaller than the cells. The two equations (3.1) and (3.2) constitute the celebrated *Keller-Segel model* [41]. Typically, one adds no-flux boundary conditions of c and ρ along a smooth boundary $\partial\Omega$ and assumes some starting fields c_0, ρ_0 .

As it turns out, the behavior of the system strongly depends on its dimension. In three dimensions, a so-called *chemotactic collapse* is expected for any parameter set [82]. In such a case, the solution develops a δ -function in finite time, i.e., it becomes singular. For one dimension, no such collapse occurs in finite time. In two dimensions, which is

the case we will deal with throughout this thesis, there exists a threshold condition [83]:

$$b(\Omega) < \frac{\sigma \zeta k}{D_c D_{\text{eff}}}, \quad (3.3)$$

where σ refers to the total density of cells. Whenever the value b , which only depends on the the region Ω , fulfills the above condition, a chemotactic collapse is expected. Condition 3.3 is true whenever chemotaxis dominates over diffusion. In this case, diffusion, which tends to smear out the solution, does not act fast enough to prevent the positive feedback of chemotactic agglomeration: particles accumulate in regions with higher c , more chemical is produced in this region (by virtue of the term $k\rho$ in Eq. (3.2)), the gradients ∇c become steeper, more particles move to this region etc. However, this phenomenological explanation does not account for dimensions, it only explains why agglomeration occurs for a sufficiently strong chemotactic flux in the first place. For mathematical derivations of collapse solutions we refer to Refs. [82, 83].

We simulate Eqs. (3.1),(3.2) in two dimensions for a situation where the inequality 3.3 holds (Fig. 3.1, right column) and another one, where it is violated (Fig. 3.1, left column). The initial field $\rho(0)$ is homogeneous with a small peak in the middle of the square box, while c is chosen uniformly. We see that in the first case the blow-up in the center occurs in finite time, whereas in the second diffusion smears out the initial disturbance.

Note that in condition (3.3) γ does not appear. For $\Omega = \mathcal{R}^d$, with d being the dimension of the system, the situation is different. Indeed, performing a standard linear stability analysis of Eqs. (3.1) and (3.2) one finds that for small enough γ a collapse always emerges. In experiments with colonies of *E.coli*, the theoretically predicted collapse has indeed been observed [84]. Recently, the Keller-Segel model has been proposed to describe super-nova explosions due to thermophoresis [9] or clustering of colloids [14]. In Chap. 4.7 we will show how to derive the Keller-Segel equations for an assembly of active colloids which interact via diffusiophoresis.

3.2. Chemotaxis in bacterial systems

In this section, we first discuss the stochastic random walks of the bacteria *E.coli* and *P.putida* and how the walk of *E.coli* is biased in order to perform chemotaxis. Next, the biochemical signaling mechanism, which enables *E.coli* to perform chemotaxis, is presented and the chemotactic response function is introduced. We present a method how to infer it from experimental trajectories and, finally, discuss how its shape affects chemotaxis.

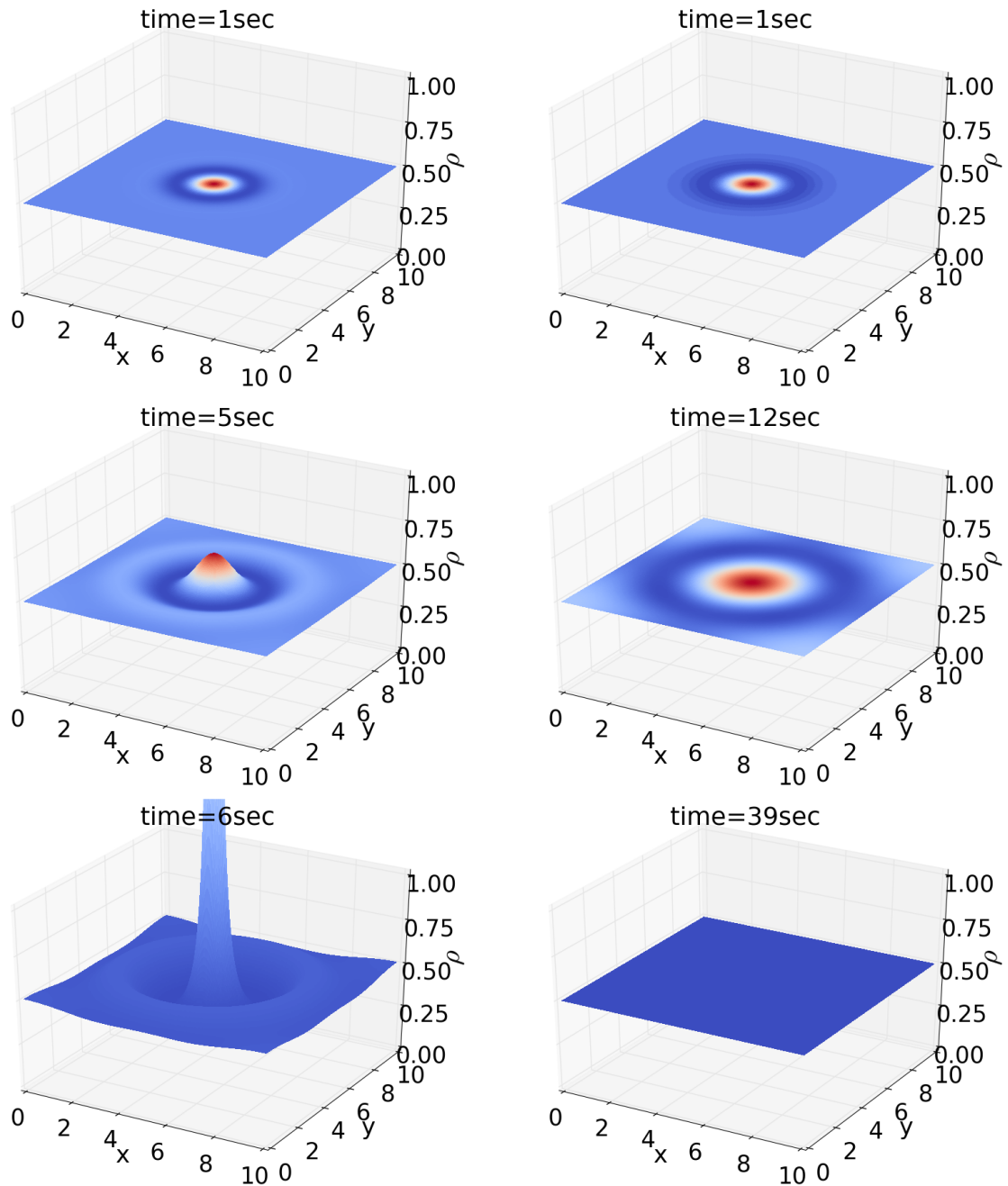


Figure 3.1.: Simulation snapshots of Eqs. (3.1) and (3.2) in two dimensions. Bacterial density ρ is plotted in the plane for different time points in the simulation. Colors represent ρ , they serve to better distinguish the shape of the graphs. Left column: Condition (3.3) fulfilled. Right column: Condition (3.3) not fulfilled.

3.2.1. Random Walk of the bacteria *E.coli* and *P.putida*

In the early seventies, Howard C. Berg and others started to investigate quantitatively the motion and chemotactic behavior of *E. coli* [46]. The natural habitat of this bacterium are mammal's guts. It has a rod-like shape with a length of about 2 up to 6 μm and about 1 μm width, and carries one up to ten [85] flagella spread all over the body (see a portrait in Fig. 3.2). When it swims, each flagellum rotates counterclockwise (CCW) and the flagella collect to one single bundle to effectively thrust the cell forward. After an exponentially distributed time T (with $\langle T \rangle \approx 1 \text{ sec}$) a so-called *tumble* occurs. This happens when at least one flagellum changes rotation direction to clockwise (CW), after which the whole bundle gets disrupted. During a tumble, the bacterium reorients with a certain tumble angle β in a new, random direction. The distribution of this angle, P_β , has a skewed shape with $\langle |\beta| \rangle \approx 68^\circ$, a maximum at about 50° , and it vanishes at 180° as well as 0° [see Fig. 3.3, left]. As will be discussed further in Sec. 5.4, the latter is a consequence of the fact that the angle was measured in three dimensions. The whole random walk is termed *run-and-tumble* motion [45].

The bacterium *P.putida* (Fig. 3.2, right) typically lives in the soil, in water, or on plants and animals [86]. It has a similar shape as *E.coli* and is a multi-flagellated bacterium, too. However, the flagella are polar, meaning that they are located at one of its extreme ends. The swimming behavior of this bacterium is particular. First of all, the run times are γ -distributed [87], and hence, they are not memoryless (Sec. 2.1.5). As discussed in Sec. 2.1.5, this means that if the bacterium has not yet tumbled t seconds after the last tumble, then the probability that it tumbles in the next instance of time *does* depend on t . The most striking characteristics of their random walk are the *reverse events*, during which the bacterium reverses its motion, i.e., $\beta \approx 180^\circ$.

For chemotaxis, the run-and-tumble random walk is biased such that the bacterium runs longer in gradient direction than against it. For *E.coli* the biochemical mechanism, which enables the bacterium to perform chemotaxis, is known to great detail [88]. In the following, we give a short introduction to the chemotaxis of *E.coli*.

3.2.2. Chemotaxis of *E.coli*

Here, we present the basic biochemical processes enabling the bacterium *E.coli* to perform chemotaxis [88]. At the outer surface of the membrane (periplasmic domain), various so-called methyl-accepting chemotaxis proteins (MCP) are located, which act as receptors for attaching molecules (or ligands). If the ligand turns out to be a nutrient, it might bind to a receptor with a probability that depends on the receptor's methylation level m . Large m decreases the probability of binding. Binding inhibits the autophosphorylation of the histidine protein kinase (HPK) CheA, which is attached to the receptor. The phosphorylated molecule CheA_p activates the so-called response regulator CheY. Finally, the activated CheY, called CheY_p, diffuses through the bacterial cytoplasm to a flagella

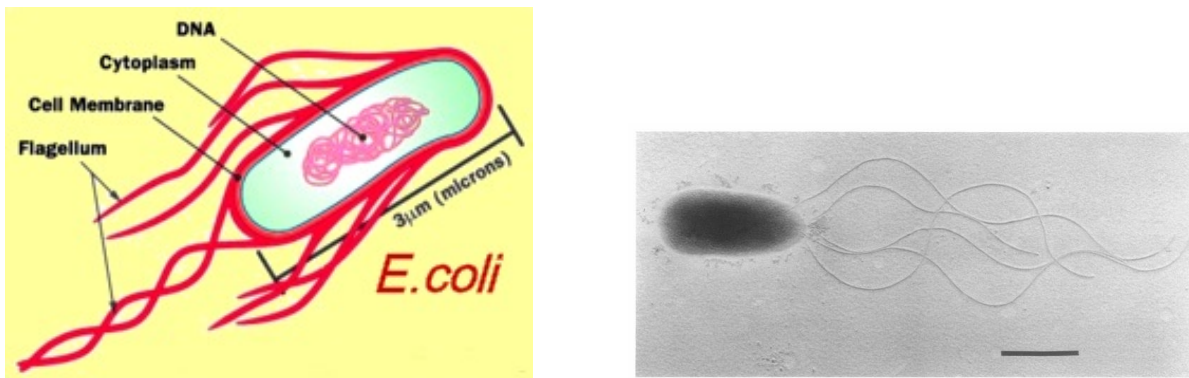


Figure 3.2.: Left: A schematic drawing of *E. coli* [89]. One sees that the flagella are spread all over the membrane. Right: An electron micrograph of *P. putida* from [90]. The bar below corresponds to $1\mu\text{m}$. The flagella are attached on one end of the cell.

motor, where it increases the probability of turning clockwise, thereby initiating a tumble event. This is the first part of the story: The more nutrients arrive, the less tumbling occurs, because bound nutrients inhibit autophosphorylation of CheA. This process is very fast, such that a sudden increase of nutrient concentration leads to a rapid decrease of the tumble rate.

However, two proteins, called CheR and CheB, balance this effect after a certain time. CheR methylizes the receptors with a rate independent of the signaling process making binding less probable. On the other hand, CheB becomes phosphorylated by CheA_p (like CheY) and effectively demethylizes the receptor (lowers m). Hence, when many ligands arrive at the receptor, m increases, since only few CheB_ps demethylize MCPs and methylation due to CheR dominates. High m leads to less binding of ligands and, therefore, higher activity of CheA, which effects a higher tumble rate. In this situation, the tumble rate turns out to be even larger than before the nutrient increase, i.e., the reduction of CheB_ps leads to an overshoot. Eventually, methylation and demethylation level out and the system returns to its initial state. Summing up, the processes in temporal order after a sudden nutrient increase are:

1. In about 0.2 seconds the tumble rate strongly decreases
2. After about $\tau_o \approx 1$ sec. the tumble rate overshoots because of suppressed demethylation of CheB leading to high m and active CheAs.
3. After about $\tau_r \approx 3 - 10$ sec. recurrence to the initial state since demethylation starts to work again triggered by more CheA_p

Experiments, which quantitatively measured the chemotactic response to external stimuli, were performed in the early eighties [47]. Bacteria were tethered near a pipette,

which at some point in time injected a nutrient pulse. The bacterial response is pictured in Fig. 3.3 on the right. The curve $R(t)$, called the *response function*, represents the difference of the equilibrium tumble rate (the tumble rate without stimulus) minus the measured tumble rate at a time t after the stimulus at time zero. We identify the three temporal states listed above: sudden response, overshoot, and recurrence. In addition, one finds

$$\int_0^\infty R \approx 0 \quad (3.4)$$

meaning that the response at different background concentrations is always the same. This very important property of chemotaxis is called *adaptedness*. Note that a bacterium like *E.coli* may be adapted to some chemicals, such as *glucose*, but, at the same time, it might be imperfectly adapted to other chemicals, which is the case for *E.coli* with the nutrient *serine* [48].

Its shape was verified recently [48] in experiments with a non-invasive inference method, which is reviewed in the following section. It was also shown that the chemotactic response varies strongly within one *E.coli* population of the same genotype, which is indicated by the strongly varying recurrence time τ_r . Indeed, molecular noise in the concentrations of CheR and CheY_p are responsible for the large fluctuations in τ_r [91]. Assuming a linear response to the concentration field, which the bacterium experienced along its recent past, one uses R to quantify the chemotactic response in terms of tumble rate:

$$\lambda(t) = \lambda_{\text{equ}} - \int_{-\infty}^t c[\mathbf{r}(t')]R(t-t')dt'. \quad (3.5)$$

This equation explains the term “adapted”. Indeed, when Eq. 3.4 holds, the response is independent of different background concentrations C with $c(t) = C + \tilde{c}(t)$.

Next, we present an inference method to determine R , while in Sec. 3.2.4 we will discuss the chemotactic behavior for two different simplified response functions.

3.2.3. Inference of the response function

As we have mentioned in the previous chapter, in Ref. [48] a Bayesian inference procedure was presented to determine the bacterial response function without actively interfering with the experiments. It is presented within this section.

We assume that a dataset is available containing sufficiently long trajectories of a bacterium, which performs run-and-tumble motion in a linear chemical concentration gradient. For notational transparency, we describe the treatment for one particular trajectory, in practice one of course needs to repeat it with several more tracks. Each trajectory point, recorded with sampling rate $1/\Delta t$, is determined to be either in a running state or in a tumbling state. To this end, Ref. [48] uses a heuristic tumble recognizer very similar to the one explained in Sec. 5.4.

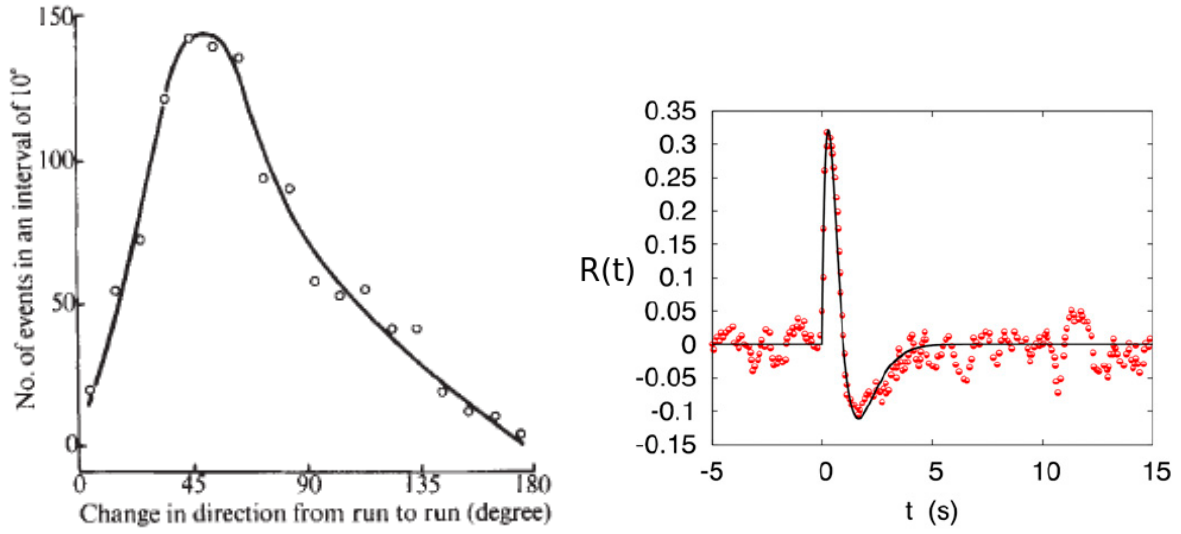


Figure 3.3.: Left: The tumble angle as measured by H.Berg et al. [46]. It is skewed and resembles a gamma-distribution. Right: Response function R measured experimentally by H.Berg et al. [47], figure extracted from Ref. [48].

After all, one obtains two vectors \mathbf{c} and \mathbf{t} . Their size is equal to $\lceil T/\Delta t \rceil$ with T being the trajectory time length. \mathbf{c} represents the nutrient concentration at each trajectory point, while \mathbf{t} carries the tumble information with elements being either 1 for “tumble” or 0 for “run”. Determining the response function R means, in Bayesian nomenclature, searching for the R which is most probable given the observables \mathbf{c} and \mathbf{t} . As usual, $P(a|b)$ refers to the probability of an object (one or many values, vectors, or functions) a conditioned on b . An application of Bayes’ formula yields:

$$P(R|\mathbf{t}, \mathbf{c}) = \frac{P(\mathbf{t}, \mathbf{c}|R)P_0(R)}{P(\mathbf{t}, \mathbf{c})}. \quad (3.6)$$

Here, P_0 is called the prior, which assigns probabilities to different response functions R . In Ref. [48] no prior information is assumed, hence P_0 is uniform. The denominator is a normalization. The important quantity is the so-called *likelihood* $P(\mathbf{t}, \mathbf{c}|R)$, the probability that the observables \mathbf{t} and \mathbf{c} are both true, given a particular response function R . The total likelihood calculates to a multiplication of the single event likelihoods at each time point:

$$P(\mathbf{t}, \mathbf{c}|R) = \prod_{t=0}^{T/\Delta t} p_r(t), \quad (3.7)$$

with $r \in \{0, 1\}$. If at $t - \Delta t$ there is a run-point, i.e., $\mathbf{t}(t - \Delta t) = 0$, one obtains:

$$p_0(t) = \begin{cases} \frac{1 - C_T(t) \cdot \Delta t}{\tau_r} & \text{if } \mathbf{t}(t) = \text{tumble} \\ 1 - \frac{1 - C_T(t) \cdot \Delta t}{\tau_r} & \text{if } \mathbf{t}(t) = \text{run} \end{cases}, \quad (3.8)$$

where $C_T(t) := \sum_{t'=0}^{\lceil t/\Delta t \rceil} \mathbf{c}(t')R(t - t')\Delta t$ and τ_r represents the mean run length. Note that these likelihoods are directly obtained from Eq. (3.5).

Otherwise, i.e., for $\mathbf{t}(t - \Delta t) = 1$, the single event likelihood is independent of the concentration history. This is because experiments indicate that the duration of the tumbling event, the tumble time, is not affected by the track history [46]. The tumble time is rather exponentially distributed such that one obtains:

$$p_1(t) = \begin{cases} \frac{\Delta t}{\tau_t} & \text{for } \mathbf{t}(t) = \text{tumble} \\ 1 - \frac{\Delta t}{\tau_t} & \text{for } \mathbf{t}(t) = \text{run} \end{cases}, \quad (3.9)$$

with τ_t representing the mean tumble time.

Next, one seeks to maximize the total likelihood 3.7 by varying the response function. In order to reduce the search space of R , the function is parametrized as:

$$R_{\mathbf{p}}(t) := \exp(\gamma t)(a_0 - a_1 \gamma t), \quad (3.10)$$

with the parameter vector $\mathbf{p} = (a_0, a_1, \gamma)$. An appropriate optimization routine then searches for the parameter vector \mathbf{p}_{opt} , which maximizes the likelihood:

$$\mathbf{p}_{\text{opt}} = \arg \max_{\mathbf{p}} P(\mathbf{t}, \mathbf{c} | R_{\mathbf{p}}). \quad (3.11)$$

Here, $\arg \max$ yields the argument at which the maximum is assumed. Because the prior $P_0(R)$ has been chosen flat, the maximization of the likelihood maximizes also the posterior distribution $P(R | \mathbf{t}, \mathbf{c})$ in Eq. (3.6). Therefore, the result of the Bayesian inference is $R_{\mathbf{p}_{\text{opt}}}$.

3.2.4. Chemokinesis vs. Chemotaxis

In the year 2004, Pierre-Gilles de Gennes calculated the *chemotactic velocity* v_c , with which an *E.coli* bacterium climbs up a chemical gradient [92]. He drew an intriguing conclusion: v_c becomes maximal when $R(t) = \alpha \delta(t)$. Plugging this into Eq. (3.5) we obtain:

$$\lambda[\mathbf{r}(t)] = \lambda_{\text{equ}} - \alpha c[\mathbf{r}(t)]. \quad (3.12)$$

Hence, the response to the concentration field is instantaneous and independent of its gradient. This strategy is called *chemokinesis*. As discussed in Sec. 3.2.2, the biological response function has a different shape and serves essentially to detect ∇c . Hence, one

may ask, why bacteria developed a complex response mechanism with memory, if it is sufficient to just measure the present background concentration. We will see that the answer may be found by inspecting the distribution of the stationary state position of such a kinesis random walker, which turns out to be not so beneficial.

To see this, consider an active walker which moves with a certain space-dependent velocity $v(\mathbf{r})$ and occasionally tumbles in a random direction with a space-dependent tumble rate $\lambda(\mathbf{r})$. The tumbles are modeled as shots in the angular direction of the walker. The corresponding equation of the probability density $\rho(\mathbf{e}, \mathbf{r}, t)$ for its moving direction \mathbf{e} and position \mathbf{r} at time t is obtained when transforming the model for an active shot-walker (Eqs. 2.48, 2.49) into the generalized Fokker-Planck equation (2.33). In this case, the shots occur in the variable \mathbf{e} , so that we integrate over all possible jumps from direction $\mathbf{e} - \mathbf{e}'$ to \mathbf{e} :

$$\dot{\rho} = -\nabla \cdot (\rho v(\mathbf{r})\mathbf{e}) + \int P_\beta(\mathbf{e}')\lambda(\mathbf{r})[\rho(\mathbf{r}, \mathbf{e} - \mathbf{e}') - \rho(\mathbf{r}, \mathbf{e})]d\mathbf{e}'. \quad (3.13)$$

The distribution of the tumble angles was assumed as uniform, hence, we have $P_\beta(\mathbf{e}) = \frac{1}{A}$ with A being the surface of the sphere in d dimensions. Upon setting $P_0 := \int \rho d\mathbf{e}$ we obtain:

$$\dot{\rho} = -\nabla \cdot (\rho v(\mathbf{r})\mathbf{e}) - \lambda(\mathbf{r})\rho + \frac{P_0\lambda(\mathbf{r})}{A}.$$

Next, one expands in spherical harmonics [80]. After neglecting higher order gradient terms and closing the hierarchy of moments as in Sec. 2.2.3, one obtains a closed formula for the density in d dimensions:

$$-\nabla \cdot \mathbf{J} = \dot{P}_0 = \nabla \cdot \frac{v(\mathbf{r})}{d\lambda(\mathbf{r})} \nabla [v(\mathbf{r})P_0]. \quad (3.14)$$

Note that in the system of repulsive colloids from Sec. 2.2.3 the analogous expression (2.68) for Brownian walkers appears. We search for stationary solutions, i.e., $\dot{P}_0 = 0$ possibly with finite flux \mathbf{J} . We introduce the effective diffusion coefficient for shot-walkers $D_{\text{eff}} := \frac{v^2}{d\lambda}$. Then, we distinguish several cases:

1. $v(\mathbf{r}) = v$ is constant. In this case we obtain $\dot{P}_0 = \nabla \cdot D_{\text{eff}}(\mathbf{r})\nabla P_0$. The stationary density P_0 is constant.
2. $\lambda(\mathbf{r}) = \lambda_{\text{equ}}$ is constant. From Eq. (3.14) we see that a stationary solution is $P_0 = \frac{1}{v}$.
3. The mean free path $\frac{v(\mathbf{r})}{\lambda(\mathbf{r})}$ is constant. Again a stationary solution is $P_0 = \frac{1}{v}$ and after some algebra one obtains $\dot{P}_0 = \nabla^2 D_{\text{eff}}(\mathbf{r})P_0$.

Remarkably, in none of the cases the stationary distribution for the bacterium depends on the space-dependent tumble rate. Therefore, a strategy based on adapting the tumble rate to $c(\mathbf{r})$, i.e., chemokinesis, does not lead it to higher concentration fields. In fact, due to the finite tumble time the effective speed of the bacterium is higher when it tumbles less, i.e., in high nutrient concentration regions. This leads to case 2 or 3 in which the bacteria accumulate in *low* concentration regions.

The cases classified above can be related to different interpretations of one single multiplicative stochastic differential equation

$$d\mathbf{x} = g(\mathbf{X})d\mathbf{B}(t), \quad (3.15)$$

with $g(\mathbf{x}) := v(\mathbf{x})\sqrt{\frac{2}{d\lambda(\mathbf{x})}}$. Indeed, case 1 is the FPE of Eq. (3.15) in Klimontovich interpretation, case 2 in Stratonovich and case 3 in Ito interpretation. As discussed in Sec. 2.1.3, when only the Brownian noise coefficient g is known, one faces the Ito-Stratonovich dilemma, i.e., the interpretation of Eq. 3.15 remains obscure. Here, we have presented an example, where additional microscopic information connects three interpretations of an SDE with their respective physical or biological meaning.

Going back to the perspective of chemotactic response, we can study the simplified case of $R(t) := \partial_t \delta(t)$.¹ Note that the derivative of a delta function captures key features of the real biological response function: it has a positive as well as a negative lobe and its integral vanishes. By plugging this response function into Eq. (3.5) and assuming constant speed $v = v_0$, we obtain:

$$\lambda(\mathbf{e}, t) = \lambda_{\text{equ}} - \dot{\mathbf{r}}(t) \cdot \nabla c = \lambda_{\text{equ}} - v_0 \mathbf{e} \cdot \nabla c. \quad (3.16)$$

Upon substituting this expression for the tumble rate in Eq. (2.33) and replacing the position x with direction \mathbf{e} , one obtains:

$$\begin{aligned} \dot{\rho} &= -\nabla \cdot (\rho v_0 \mathbf{e}) - \lambda(\mathbf{e}, t)\rho + \frac{P_0 \lambda_{\text{equ}}}{A} - \frac{v_0}{A} \nabla c \cdot \int \rho(\mathbf{e}' - \mathbf{e}, \mathbf{r}, t)(\mathbf{e}' - \mathbf{e}) d\mathbf{e}' \\ &= -\nabla \cdot (\rho v_0 \mathbf{e}) - \lambda_{\text{equ}}\rho + \frac{P_0 \lambda_{\text{equ}}}{A} + v_0 \mathbf{e} \cdot \nabla c \rho - \frac{v_0}{A} \nabla c \cdot \mathbf{P}_1, \end{aligned} \quad (3.17)$$

where for the last equation we used translational invariance and defined the polarization $\mathbf{P}_1 = \int \mathbf{e} \rho(\mathbf{e}) d\mathbf{e}$. After another expansion into moments and appropriate approximations [80], we see that the polarization term translates into flow upwards the concentration gradient:

$$-\nabla \cdot \mathbf{J} = \dot{P}_0 = \nabla \cdot \left[\frac{v_0 \nabla [v_0 P_0]}{d\lambda_{\text{equ}}} - \frac{v_0 P_0 \nabla c}{d\lambda_{\text{equ}}} \right]. \quad (3.18)$$

¹Here, we again refer to a distributional derivative. Indeed, in the following calculations, we will only make use of partial integration, which is used to define the distributional derivative.

Since v_0 and λ_{equ} are constants, the first term translates into regular diffusion with effective diffusion constant D_{eff} . Assuming a linear gradient $\nabla c = \mathbf{g}$, the second term represents a flow in some direction \mathbf{g} . Hence, the problem is analogous to a classical sedimentation problem with gravity field \mathbf{g} . In this situation, it is known that the particle density builds up an exponential profile with the effective sedimentation length $\frac{v_0 d}{\lambda_{\text{equ}} D_{\text{eff}}}$. Indeed, an exponential density profile is found in experiments with *E. coli* [93].

Concluding, the presented analysis shows that successful nutrient harvesting requires knowledge of the gradient direction, when not only the chemotactic velocity but also the stationary state distribution is considered.

3.3. Diffusiophoresis: How chemical gradients lead to colloidal motion

In Sec. 3.2.2 we have seen how *E. coli* performs chemotaxis, i.e., how it recognizes chemical gradients and adapts its swimming behavior accordingly. In this section, we focus on non-living matter, in particular, on colloidal particles which have a similar size like *E. coli* ($\sim 1\mu\text{m}$ [14]). We will show that under certain conditions the synthetic colloids also swim along chemical gradients thereby mimicking the chemotactic cellular behavior. The underlying physical effect is called *diffusiophoresis*, which we elaborate in the following. We start to introduce basic concepts from hydrodynamics.

3.3.1. Basic hydrodynamics: Navier-Stokes and Stokes equations

We assume the colloid of interest to be immersed in an incompressible fluid, which can be described by two coupled equations. The first derives from momentum conservation and the second captures incompressibility by means of a divergence-free fluid velocity field \mathbf{v} [94]:

$$\rho \frac{D\mathbf{v}}{Dt} = \mathbf{f} + \nabla \cdot \underline{\boldsymbol{\sigma}}, \quad \nabla \cdot \mathbf{v} = 0. \quad (3.19)$$

Here, $\frac{D}{Dt}$ is the total derivative, \mathbf{f} a force, for example, gravity, and $\underline{\boldsymbol{\sigma}}$ the stress tensor. The first equation states that the change of momentum at a point in space is caused, first, by an external force and, second by stress, which is exerted by the fluid. We assume a Newtonian fluid for which linear pressure P and a change of the flow velocity directly translates into a deformation of the fluid at a given point:

$$\underline{\boldsymbol{\sigma}} = -P\mathbf{1} + \mu(\nabla \otimes \mathbf{v} + \nabla^T \otimes \mathbf{v}). \quad (3.20)$$

Here, μ is the shear viscosity quantifying the strength of the force which is needed to shear the fluid. Plugging this into Eq. (3.19), we obtain the celebrated *Navier-Stokes equations*

$$\rho[\dot{\mathbf{v}} + (\mathbf{v} \cdot \nabla)\mathbf{v}] = \mathbf{f} - \nabla P + \mu \nabla^2 \mathbf{v}, \quad \nabla \cdot \mathbf{v} = 0. \quad (3.21)$$

This is a system of non-linear partial differential equations of second order. Its existence and smoothness for high initial velocity \mathbf{v}_0 in three dimensions have not yet been proven rigorously [95]. There are several numerical solving techniques such as multi-particle-collision dynamics [96] or lattice Boltzmann approaches [97]. In order to reduce the complexity of the equation, one can compare the strength of inertia to the viscous forces:

$$\frac{|\rho \mathbf{v} \cdot \nabla \mathbf{v}|}{|\mu \nabla^2 \mathbf{v}|} \approx \frac{\rho v_0^2 / l}{\mu v_0 / l^2} = \frac{v_0 \rho l}{\mu} =: \text{Re}, \quad (3.22)$$

where we introduced the so-called *Reynolds number* Re . v_0 is a typical velocity and l a typical length scale. We choose the colloidal velocity $v_0 \sim 4\mu\text{m/s}$ from experiments [14] and their radius $l = 1\mu\text{m}$. Assuming the particle to swim in water ($\mu = 0.001\text{ kg/ms}$), we obtain:

$$\text{Re} = \frac{(4 \cdot 10^{-6}) \times (10^3) \times (10^{-6})}{0.001} = 4 \times 10^{-6} \ll 1. \quad (3.23)$$

If we rescale space with l , velocity with v_0 , and time with the diffusive time scale τ , we obtain:

$$\frac{\rho_0 a^2}{\tau \mu} \dot{\mathbf{v}} + \text{Re}(\mathbf{v} \cdot \nabla)\mathbf{v} = \mathbf{f} - \nabla P + \mu \nabla^2 \mathbf{v}. \quad (3.24)$$

We see that for small Re we may drop the unpleasant non-linear inertia term. Moreover, when we are only interested in stationary solutions, we can also drop the time derivative on the left hand side. We remain with the so-called Stokes equations:

$$0 = \mathbf{f} - \nabla \cdot \underline{\boldsymbol{\sigma}} = \mathbf{f} - \nabla P + \mu \nabla^2 \mathbf{v} \quad \nabla \cdot \mathbf{v} = 0. \quad (3.25)$$

They build a common framework to describe microscopic entities in fluids and their ambient flow in the *overdamped regime* where inertia can be neglected. One particularity is the invariance under time change $t \rightarrow -t$ meaning that motion is exactly reversible provided that \mathbf{f} does not depend on time. In particular, a reciprocal cyclic movement pattern cannot lead to directed flow, which is the content of the famous Scallop theorem. The scallop is a valve which actively moves forward. For this purpose, it absorbs water slowly and spills it out much faster. Due to inertia a net motion follows. However, for low Reynolds numbers this would not be the case since the strategy is exactly time reversible [98]. The pollen's jittery motion from section 2.1.1 can also be considered as overdamped which is why we neglected inertia in our argumentation. We next want to employ Eqs. 3.25 to deduce the swimming velocity of a colloid immersed in a liquid, which carries a concentration gradient of another solute.

3.3.2. Slip velocity \mathbf{v}_s

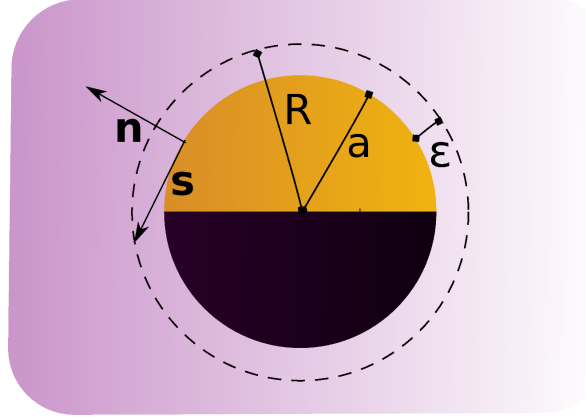


Figure 3.4.: Schematics of a so-called Janus particle which is a colloid with two different covers on each half-sphere. The dashed line is what we call the outer surface with radius $R = a + \epsilon$. \mathbf{n} is the outer normal, while \mathbf{s} represents the tangential space attached at a random point on the surface.

In Fig. 3.4 we show a colloid with radius a . The colloid is immersed in a fluid, which carries a concentration gradient of a chemical field $c(\mathbf{r})$. Each chemical particle experiences a short-range attraction (or repulsion) from the colloidal surface, which is described by the potential $U(\mathbf{r})$. We introduce a small outer surface layer with width ϵ , the length scale of the potential U . Furthermore, we define $R = a + \epsilon$. Since $\epsilon \ll a$, we can assume the surface as flat and define a Cartesian coordinate system on it. The two vectors \mathbf{s} span the tangential and \mathbf{n} points in normal direction. The coordinate in normal direction is called z , while the coordinates in tangential direction shall be subsumed in the vector \mathbf{s} such that $\mathbf{r} = (\mathbf{s}, z)$.

Within the thin surface layer we expect a rapid equilibration of the field c . Indeed, one approximates it to build up instantaneously. Then, close to the surface, we obtain a stationary Boltzmann distribution:

$$c(\mathbf{s}, z) = c(\mathbf{s}, R) \exp[-(k_B T)^{-1} U(\mathbf{s}, z)], \quad (3.26)$$

with $z \in [a, R]$. Each chemical molecule exerts a force on a fluid element so that the force becomes:

$$\mathbf{f}(\mathbf{s}, z) = -c(\mathbf{s}, z) \nabla U = -c(\mathbf{s}, z) (\partial_z U) \mathbf{n}. \quad (3.27)$$

The last equation originates from the fact that the potential U only varies in normal direction. Making use of Eq. 3.26, we can alternatively write

$$\mathbf{f}(\mathbf{s}, z) = k_B T \partial_z c(\mathbf{s}, z) \mathbf{n}. \quad (3.28)$$

With this expression we obtain the following version of the Stokes-equation:

$$0 = k_B T \partial_z c \mathbf{n} - \nabla P + \mu \nabla^2 \mathbf{v}. \quad (3.29)$$

We separate normal velocity ($v_z = \mathbf{n} \cdot \mathbf{v}$) from the tangential velocity $\mathbf{v}_s = (\mathbf{1} - \mathbf{nn})\mathbf{v}$. For v_z the Stokes-equation reads

$$0 = -\partial_z P + \mu \nabla^2 v_z - k_B T \partial_z c. \quad (3.30)$$

We neglect the second term on the right-hand side since there are no major fluctuations in the outward fluid velocity v_z on the small length scales we work on. Then, we can integrate Eq. (3.30) to obtain

$$P(\mathbf{s}, z) = P(\mathbf{s}, R) + k_B T c(\mathbf{s}, R) \left(\exp \left[- (k_B T)^{-1} U(\mathbf{s}, z) \right] - 1 \right). \quad (3.31)$$

Equipped with an explicit equation for the pressure, we now want to calculate the so-called *slip velocity* \mathbf{v}_s . This is the tangential velocity of the fluid relative to the colloidal particle at distance R from the surface (see again Fig. 3.4). What is typically referred to as the slip velocity, i.e., the tangential relative fluid velocity at the very particle surface, is of course zero. In tangential direction, there acts no force. Therefore, the Stokes equation of \mathbf{v}_s reads

$$0 = -\nabla_s P + \mu \nabla^2 \mathbf{v}_s, \quad (3.32)$$

so that we obtain flow by virtue of pressure gradients on the colloidal surface. By substituting Eq. (3.31) in the previous equation, we obtain:

$$0 = \mu \partial_z^2 \mathbf{v}_s + k_B T \nabla_s c(\mathbf{s}, R) \left(\exp \left[- (k_B T)^{-1} U(\mathbf{s}, z) \right] - 1 \right),$$

where we neglected the slip velocity variations along the outer surface: $\mu \nabla_s^2 \mathbf{v}_s = 0$. Integrating twice and making use of $\mathbf{v}_s(\mathbf{s}, 0) = 0$ (slip velocity at inner surface), $\partial_z \mathbf{v}_s(\mathbf{s}, R) = 0$ and $\nabla_s P(\mathbf{s}, R) = 0$, leads to:

$$\mathbf{v}_s = -\frac{k_B T}{\mu} \nabla_s c(\mathbf{s}, R) \int_a^R z \left[\exp \left[- (k_B T)^{-1} U(\mathbf{s}, z) \right] - 1 \right] dz = -\nabla_s c(\mathbf{s}, R) \zeta(\mathbf{s}), \quad (3.33)$$

where we introduced the slip velocity coefficient

$$\zeta = \frac{k_B T}{\mu} \int_a^R z \left(\exp \left[- (k_B T)^{-1} U(\mathbf{s}, z) \right] - 1 \right) dz. \quad (3.34)$$

Summing up, we have shown how pressure gradients along the surface arise due to forces exerted by a concentration field close to the surface. These pressure gradients then lead to slip flow with velocity \mathbf{v}_s . Next, we will make use of \mathbf{v}_s , which will be interpreted as boundary condition for the flow velocity in order to calculate the velocity of the colloidal particle.

3.3.3. Swimming velocity and torque

Let \mathbf{V} be the translational velocity of a colloid and $\mathbf{\Omega}$ its angular velocity. Then, at distance R from the colloidal center, i.e., at the outer surface, we have:

$$\mathbf{v} = \mathbf{V} + \mathbf{r} \times \mathbf{\Omega} + \mathbf{v}_s. \quad (3.35)$$

Naively starting, we would have to calculate the entire fluid velocity field \mathbf{v} in order to obtain \mathbf{V} . Fortunately, the so-called *Lorentz reciprocity theorem* [99] can be invoked to solve directly for \mathbf{V} and $\mathbf{\Omega}$. For this purpose, we consider two systems. Both are described by the Stokes equations (3.25) and contain one colloid immersed in the fluid. In the first, there is no external force, i.e., $\mathbf{f} = 0$, and there is a slip velocity \mathbf{v}_s as in Eq. (3.33). This situation represents a force-free swimmer. We obtain the velocity field \mathbf{v} as solution of the Stokes equations. In the second system, we assume an external force $\tilde{\mathbf{f}}$ and no-slip boundary condition leading to a solution $\tilde{\mathbf{v}}$. With $\tilde{\boldsymbol{\sigma}}$ and $\boldsymbol{\sigma}$ representing the respective stresses of the two systems, the Lorentz reciprocity theorem states [99]:

$$\int_{S(t)} \mathbf{n} \cdot \tilde{\boldsymbol{\sigma}} \cdot \mathbf{v} dS = \int_{S(t)} \mathbf{n} \cdot \boldsymbol{\sigma} \cdot \tilde{\mathbf{v}} dS. \quad (3.36)$$

Since $\tilde{\mathbf{v}} = \tilde{\mathbf{V}}$ on S (no-slip) and the first colloidal swimmer is force-free ($\int \mathbf{n} \cdot \boldsymbol{\sigma} = 0$), the right-hand side vanishes. Substituting Eq. (3.35) for \mathbf{v} yields [100]

$$\tilde{\mathbf{f}} \cdot \mathbf{V} = - \int_S \mathbf{n} \cdot \tilde{\boldsymbol{\sigma}} \cdot \mathbf{v}_s dS. \quad (3.37)$$

Making use of the known formulae for the Stokes drag force $\tilde{\mathbf{f}} = -6\pi\mu a \tilde{\mathbf{V}}$ and the surface stress $\mathbf{n} \cdot \boldsymbol{\sigma} = -\frac{3\mu}{2a} \tilde{\mathbf{V}}$, one finally obtains:

$$\mathbf{V} = -\frac{1}{4\pi a^2} \int_S \mathbf{v}_s dS. \quad (3.38)$$

Thus, as particle velocity we obtain the negative average slip velocity on the particle surface.

To determine the angular velocity $\mathbf{\Omega}$, we proceed similarly. In particular, in the first system we assume the colloid to be torque-free, while in the second an external torque $\tilde{\mathbf{T}}$ is applied, which leads to an angular velocity $\tilde{\mathbf{\Omega}}$. Then, we obtain similar to Eq. (3.37):

$$\tilde{\mathbf{T}} \cdot \mathbf{V} = - \int_S \mathbf{n} \cdot \tilde{\boldsymbol{\sigma}} \cdot \mathbf{v} dS. \quad (3.39)$$

For a rotating sphere we have $\tilde{\mathbf{T}} = -8\pi\mu a^3 \tilde{\mathbf{\Omega}}$ and $\mathbf{n} \cdot \tilde{\boldsymbol{\sigma}} = 3\mu \tilde{\mathbf{\Omega}} \times \mathbf{n}$. Then, from Eq. (3.39) the angular velocity is calculated to

$$\mathbf{\Omega} = \frac{3}{8\pi a^3} \int_S \mathbf{n} \times \mathbf{v}_s dS. \quad (3.40)$$

Next, we plug the slip velocity as in Eq. (3.33) into the solutions (3.38) and (3.40) to obtain surface integrals of the form $\int_S \nabla c \zeta dS$. The field c needs to fulfill a no flux boundary condition on the colloidal surface for which reason it will deviate from an undisturbed field c_∞ . Still, we can expand c in surface harmonics and express it in terms of c_∞ [101], where we will neglect terms of order $O(\nabla \otimes \nabla c_\infty)$ or higher. We introduce the surface average $\langle \mathbf{s} \rangle := \frac{1}{A(S)} \int_S \mathbf{s} dS$ and obtain

$$\mathbf{V} = [\langle \zeta \rangle \mathbb{1} - \frac{1}{2} \langle (3\mathbf{n} \otimes \mathbf{n} - \mathbb{1}) \zeta \rangle] \cdot \nabla c_\infty \quad (3.41)$$

$$\mathbf{\Omega} = \frac{9}{4a} \langle \mathbf{n} \zeta \rangle \times \nabla c_\infty. \quad (3.42)$$

This result allows for some insight into the nature of diffusiophoretic motion. First of all, whenever there is a chemical gradient ∇c_∞ , a translational velocity \mathbf{V} of the particle emerges, which is proportional to ∇c_∞ . Furthermore, assume the quadrupole on the right-hand side of Eq. (3.41) vanishes, which is the case for a Janus-particle as in Fig. 3.4. Then, for $\langle \zeta \rangle > 0$ the velocity \mathbf{V} will point in the chemical gradient direction, otherwise, it points against it. This can be understood as follows: When the potential U between chemical c and colloidal surface is attractive, we have $\langle \zeta \rangle > 0$. On the upper gradient side of the colloid are more attractive chemical molecules, which pull collectively stronger than the ones on the other side. This leads to a net motion towards increasing concentration.² An analogous argumentation explains motion against gradient direction in the case of repulsive interactions.

On the other hand, for constant ζ we have $\mathbf{\Omega} = 0$ because $\langle \mathbf{n} \rangle = 0$. This changes in general when the slip velocity coefficient ζ varies along the surface. Then, we expect an orientational alignment with the chemical gradient according to Eq. (3.42). Such a situation will be discussed in Chap. 4 for Janus particles.

²This is a simplified explanation since the forces are rather transmitted by the fluid as pressure gradients.

Dynamic clustering and chemotactic collapse in a system of active colloids

This chapter is essentially based on the material presented in my publications Ref. [52] and [53]. First, a model is established taking into account activity and chemical field gradients leading to diffusiophoresis. We investigate dynamic clustering as well as collapse behavior. Furthermore, the connection to bacterial chemotaxis is established by mapping our model to the celebrated Keller-Segel equations. Last, we discuss so-called reaction rates for cluster growing and shrinking showing that they represent an appropriate measure to describe dynamic clustering.

4.1. Introduction

The collective motion of synthetic microswimmers has recently gained increasing attention [6, 7, 22, 23]. Already in relatively simple setups these systems give rise to surprising phenomena. Phase separation [20, 21, 37–39, 81, 102], large density fluctuations [35, 103], pump formation in a harmonic trap [104, 105], periodic motion in Poiseuille flow [106–109], and active sedimentation under gravity [110–112] are among the plethora of non-equilibrium effects. In biology, collective motion of motile organisms forms intriguing dynamic patterns such as flocking of birds [24], phase separation in mussel beds [113], traveling waves in penguin huddles [114], swarming of midges [26], or turbulence in bacterial colonies [115].

A common property of these biological and synthetic systems is the active motion of their individual agents, as discussed in Sec. 2.2. Furthermore, biological as well as synthetic microswimmers are able to sense field gradients and move along them. For example, cellular organisms perform chemotaxis by detecting chemical gradients via multiple transmembrane receptors (see Sec. 3.2.2). Other types of taxis, like gravitaxis [116, 117] or thermotaxis [118], refer to directed motion in a gravitational field or along temperature gradients. Recently, active particle systems have been explored in connection with thermophoresis [9, 119–121] or diffusiophoresis [14, 35, 40, 122]. As discussed in Sec. 3.3, diffusiophoretic motion originates from chemical gradients along the particles surfaces. In fact, active colloids consume chemicals from the ambient fluid and thereby generate chemical field gradients themselves, which influences the swimming paths of neighboring particles and gives rise to collective motion.

Experiments with active Janus colloids or light-activated particles show pronounced *dynamic clustering* [14, 35]. Dynamic clusters of colloids (at low densities) are very dy-

dynamic structures, they form and dissolve again. This is in stark contrast to the relatively static clusters observed when active colloids, interacting only by hard-core potentials, phase-separate at large densities. The work presented here has very much been inspired by the experiments of the Lyon group [14]. As in their experiments, we will focus on so-called Janus particles which are covered with different materials on their two half-spheres.

In the following section, we briefly introduce the experimental setup of Ref. [14], which we model in Sec. 4.3. We will show how diffusiophoretic theory and the theory of active particles can be combined to formulate a model for such an assembly of interacting colloids. Afterwards we will present a state diagram which gives an overview of the system's phase behavior when varying the two relevant phoretic parameters. In particular, dynamic clustering is investigated, which needs to be subdivided in dynamic clustering 1 and 2 depending on their respective cluster-size distribution functions. Furthermore, we will study various collapse regimes in which particles gather in one large cluster. As we shall show, depending on the system parameters such a cluster may fluctuate, build a cloud or even oscillate. A moment-expansion maps our model to the Keller-Segel model. Last, we will show that studying fission and fusion rates of dynamic clusters provide local measures to distinguish the dynamic clustering 1 and 2 states.

4.2. Lyon Experiments

Here, we briefly review the experiments performed in Lyon reported in Ref. [14]. They shall be interpreted and modeled in the following section. The experiments consist of an assembly of Janus particles covered with platinum on one half of their surface and gold on the other half. The particles are immersed in a liquid containing H_2O_2 and they are confined in a rectangular cell. Since they are heavy, they quickly sink on its ground.

The first notable observation, which was already reported in Ref. [110], is that the particles instantaneously start to self-propel when inserted in the liquid. They do so with an average velocity of about $3\mu\text{m/s}$, which corresponds to three times their radius per second. When the cell is slightly tilted, the particles sediment downwards and shape an exponential sedimentation profile [110]. Hence, in what respects sedimentation, the active particles yield the results expected from equilibrium systems in a gravitation field.

However, when concentrating on the dynamics of the particles, one observes surprising collective behavior. Some particles merge into small and large clusters, others keep swimming without aggregating. The clusters have nearly crystalline structure surrounded by single particles forming a phase reminiscent of a gas. Analyzing the temporal evolution of the clusters, one observes growing but also shrinking clusters as well as single particles attaching and leaving clusters. Examples of such temporal evolutions are depicted in Fig. 4.1 on the left. The authors term these observations *dynamic clustering*.

Another intriguing experimental measurement is the linear relation of cluster size and

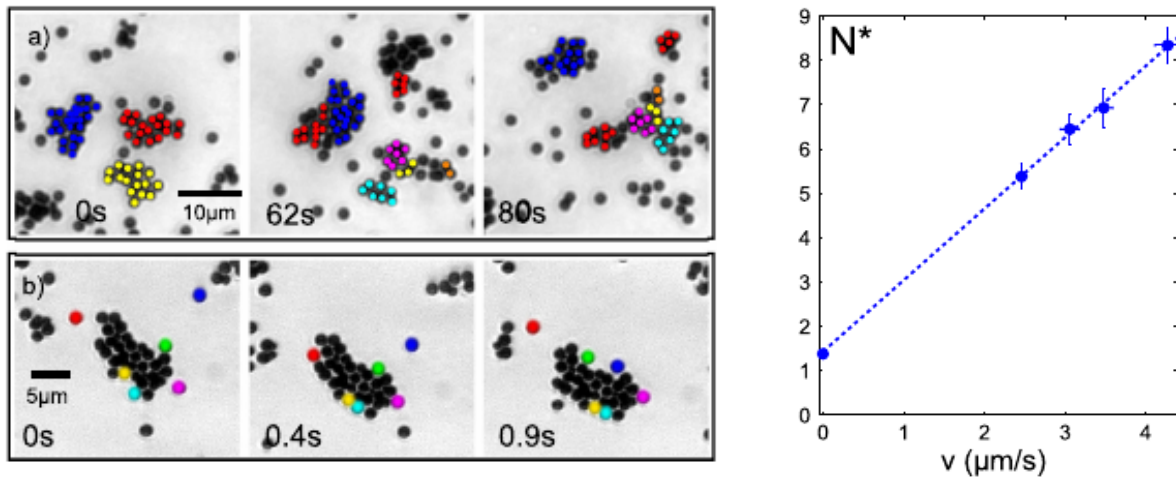


Figure 4.1.: Plots are extracted from Ref. [14]. Left: Two temporal sequences of system snapshots. The colors tag particular particles and clusters. In the top sequence clusters form, break and reassemble. In the bottom sequence single particles attach to, move along and detach from clusters. Right: The mean cluster size is plotted vs. the active swimming velocity of particles revealing a linear relation.

active velocity (Fig. 4.1, right). Indeed, such a relation was predicted for systems with active particles in high density assemblies (Sec. 2.2.3). However, the experiments presented here are conducted at a relatively low area fraction $\sigma = 0.05$. In the following sections, we elaborate an alternative explanation for the observed linear relation relying on diffusiophoresis.

4.3. Model for active colloids with interactions transmitted by a chemical field

We model a system of N active colloids that effectively interact via diffusiophoretic forces induced by a chemical field. Our model system resembles the experimental setup of Ref. [14] consisting of a collection of Janus-particles half covered with gold on one side and platinum on the other.

4.3.1. Derivation of the model equations

Typically, the colloids are heavier than the suspending solvent. They settle to the bottom of the experimental cell, where they form a colloidal monolayer. To induce activity, Ref. [14] employs gold particles half covered with platinum, which catalyzes the separation of H_2O_2 towards water and oxygen. Through a combination of self-diffusio- and elec-

trophoresis the particles self-propel (see i.e., [123–125]) with a swimming speed v_0 along direction \mathbf{e} , which we assume to be fixed in the particle. During the catalytic reactions at the surfaces of the colloids fuel is converted into several chemical products. This has two consequences. First of all, in the surrounding of the particles fuel is diminished. If the swimming speed is very sensible to the fuel concentration, particles will move slower in regions with large colloidal density. As we have seen in Sec. 2.2.3 a sufficiently strong slow-down at regions with higher density leads to phase separation. However, in the experiments of Ref. [14] a 20-fold increase of the fuel was needed to increase v_0 by a factor of about 2.5. Thus small inhomogeneities of the chemical field do not strongly alter the colloidal velocity. Applying the nomenclature of Sec. 3.2.4, we can thus neglect chemokinesis. On the other hand, as we shall see, chemotaxis does play a crucial role.

A second consequence of the particles consuming fuel is that spatial gradients of reactants and products form around them. They induce diffusiophoretic motion of neighboring particles. Eq. (3.41) states the translational swimming velocity resulting from diffusiophoresis. We neglect the quadrupolar term for our half-coated Janus particles. Defining $\zeta_{\text{tr}} := -\langle \zeta \rangle$ with the slip velocity coefficient given by Eq. (3.34), we obtain:

$$\mathbf{v}_D = -\zeta_{\text{tr}} \nabla c. \quad (4.1)$$

Defining the rotational diffusiophoretic parameter ζ_{rot} via $(9/4a)\langle \zeta \mathbf{n} \rangle = -\zeta_{\text{rot}} \mathbf{e}_i$ with \mathbf{e}_i being the swimming direction of the i -th particle, Eq. (3.42) takes the form:

$$\boldsymbol{\omega}_D = -\zeta_{\text{rot}} \mathbf{e}_i \times \nabla c. \quad (4.2)$$

The slip velocity coefficient ζ depends on the surface potential, with which the solute interacts with the colloid surface. So, by choosing appropriate materials for the Janus colloids and their caps, the phoretic parameters ζ_{rot} and ζ_{tr} might each be tuned to have a positive or negative value. The phoretic parameters also depend on the geometry and number of caps covering the colloidal surface [40].

We now formulate the overdamped Langevin equations for position \mathbf{r}_i and orientation \mathbf{e}_i of the i -th colloid. Adding up active and phoretic contributions, the deterministic translational velocity becomes $\dot{\mathbf{r}}_i = v_0 \mathbf{e}_i + \mathbf{v}_D$, and the time variation of the orientation vector is described by the kinematic equation $\dot{\mathbf{e}}_i = \boldsymbol{\omega}_D \times \mathbf{e}_i$. Then, we use Eqs. (4.1) and (4.2) together with $(\mathbf{e}_i \times \nabla c) \times \mathbf{e}_i = (\mathbf{1} - \mathbf{e}_i \otimes \mathbf{e}_i) \nabla c$ to write down the overdamped Langevin equations for each colloid:

$$\dot{\mathbf{r}}_i = v_0 \mathbf{e}_i - \zeta_{\text{tr}} \nabla c(\mathbf{r}_i) + \boldsymbol{\xi}_i, \quad (4.3)$$

$$\dot{\mathbf{e}}_i = -\zeta_{\text{rot}} (\mathbf{1} - \mathbf{e}_i \otimes \mathbf{e}_i) \nabla c(\mathbf{r}_i) + \boldsymbol{\mu}_i \times \mathbf{e}_i. \quad (4.4)$$

Here, $\boldsymbol{\xi}_i$ is translational and $\boldsymbol{\mu}_i$ rotational Gaussian white noise with zero mean and respective time correlation functions $\langle \boldsymbol{\xi}_i(t) \otimes \boldsymbol{\xi}_i(t') \rangle = 2D_{\text{tr}} \mathbf{1} \delta(t-t')$ and $\langle \boldsymbol{\mu}_i(t) \otimes \boldsymbol{\mu}_i(t') \rangle = 2D_{\text{rot}} \mathbf{1} \delta(t-t')$, where we have introduced the translational (D_{tr}) and rotational (D_{rot})

diffusion coefficients. We consider here their thermal values, but they will differ from the usual bulk coefficients since the colloids move close to the bottom boundary. Since the Reynold's number for our colloidal system is much smaller than one (see Eq. (3.23)), the dynamics can be assumed to be overdamped. Furthermore, because colloids move in a plane, we introduce an orientation angle φ_i for each colloid and the Cartesian components of the orientation vector become $e_i^x = \cos(\varphi_i)$ and $e_i^y = \sin(\varphi_i)$. Using the angle, we may rewrite Eq. (4.4) as

$$\partial_t \varphi_i = \zeta_{\text{rot}} \partial_\varphi \mathbf{e}_i \cdot \nabla c + \mu_i. \quad (4.5)$$

Other than, for example Ref. [40], we consider only the chemical concentration field c which is diminished by the fuel consumption of the colloidal particles. It evolves according to the diffusion equation:

$$\dot{c}(\mathbf{r}) = D_c \nabla^2 c - k \sum_{i=1}^N \delta(\mathbf{r} - \mathbf{r}_i), \quad (4.6)$$

where the colloids enter as sinks diminishing the field with rate k . Typically, the chemical diffuses much faster along a particle radius than the swimming colloids need for the same distance. So, we can neglect the time derivative of c in Eq. (4.6) meaning that each colloid instantly establishes a static chemical sink around itself, which moves with the colloid. The chemical diffuses in three dimensions and we use the static solution of Eq. (4.6), $c_{3d}(\mathbf{r}) = c_0 - (k/4\pi D_c) \sum_{i=1}^N 1/|\mathbf{r} - \mathbf{r}_i|$, where c_0 is the background chemical concentration. Strictly speaking, we would need to implement a non-flux boundary condition at the boundary of the infinite half-space, but this will not change the basic $1/r$ dependence of the chemical field. To introduce a two-dimensional concentration field, in which the colloidal monolayer moves, we integrate over a thin layer of thickness $h = 2a$ and obtain $c_{2d}(\mathbf{r}) = \int_0^h c_{3d}(\mathbf{r}) dz \approx h c_{3d}$. Finally, the chemical concentration field reads:

$$c_{2d}(\mathbf{r}) = h c_0 - \frac{kh}{4\pi D_c} \sum_{i=1}^N \frac{1}{|\mathbf{r} - \mathbf{r}_i|}. \quad (4.7)$$

So, self-phoretic colloids induce long-range chemical concentration gradients and via Eq. (4.3) and (4.4) long-range interactions between the colloids, which have indeed been experimentally measured by Ref. [35].

We modeled each particle as a chemical sink. Hence, if the translational diffusio-phoretic parameter ζ_{tr} is positive, the diffusiophoretic velocity \mathbf{v}_D from Eq. (4.1) is directed towards the neighboring particles and it acts as an effective attraction, while $\zeta_{\text{tr}} < 0$ gives rise to an effective repulsion. Similarly, a positive rotational parameter ζ_{rot} in Eq. (4.2) rotates the swimming direction of an active colloid towards a neighboring chemical sink and the colloid moves towards the neighbor. Hence, rotational phoresis

also acts like an attractive colloidal interaction while it becomes repulsive for $\zeta_{\text{rot}} < 0$. Tuning the signs of the phoretic parameters, one can realize different types and combinations of effective interactions and, as we shall show in the following chapters, thereby induce a variety of collective dynamics.

4.3.2. Rescaling

To reduce the parameters of our system, we rescale time by $t_r = 1/(2D_{\text{rot}})$ and length by $l_r = \sqrt{D_{\text{tr}}/D_{\text{rot}}} = 2.33a$ such that the rescaled diffusion constants are set to one in the Langevin equations (4.3) and (4.4). Using the thermal values from the Stokes-Einstein relations for the diffusion coefficients, one has $\sqrt{D_{\text{tr}}/D_{\text{rot}}} = 1.15a$. Since the colloids move close to the bottom wall, this value is changed. Indeed, in the experiments of Ref. [14] $l_r = 1.79a$ is measured. For historical reasons, we use here $l_r = 2.33a$, which does not change the qualitative behavior of our system. The actual value of l_r is needed for implementing screening of the phoretic interaction inside a colloidal cluster, as explained above. After rescaling we are left with four relevant system parameters: the Péclet number $\text{Pe} = v_0/(2\sqrt{D_{\text{tr}}D_{\text{rot}}})$, the rescaled translational diffusiophoretic parameter $\zeta_{\text{tr}}kh/(8\pi D_{\text{tr}}D_c) \rightarrow \zeta_{\text{tr}}$, the rescaled rotational diffusiophoretic parameter $\zeta_{\text{rot}}kh/(8\pi D_c\sqrt{D_{\text{tr}}D_{\text{rot}}}) \rightarrow \zeta_{\text{rot}}$, and the area fraction σ defined as the projected area of all particles divided by the area of the simulation box. Note that the factor $kh/(4\pi D_c)$ from Eq. (4.7) is subsumed into the rescaled diffusiophoretic parameters, when using $\nabla c_{2d}(\mathbf{r}_i)$ in the Langevin equations (4.3) and (4.4).

4.3.3. Screening, repulsive particle-particle and particle-wall interactions

The particles with radius a interact via a hard-core repulsion. Whenever they overlap during the simulations, we separate them along the line connecting their centers. We have also tested a hard-core potential of the form $U = \sum_i \sum_j (2a/|\mathbf{r}_i - \mathbf{r}_j|)^{36}$ revealing essentially the same results.

When colloids form compact clusters, the chemical substance cannot diffuse freely between the particles. Therefore, we implement a screened chemical field as follows. Whenever a colloid is surrounded by six closely packed neighbors with distances below $r_s = 2a(1 + \epsilon)$, we replace the term $1/|\mathbf{r} - \mathbf{r}_i|$ in Eq. (4.7) by

$$\frac{\exp[-(r - \xi)/\xi]}{|\mathbf{r} - \mathbf{r}_i|}, \quad (4.8)$$

where we introduce the screening length $\xi := r_s$. We set $\epsilon = 0.3$ and checked that our results do not change, if ϵ varies by 50%. In Ref. [40] screening occurs if the reaction rate k depends on concentration c . However, as we have discussed before, this does not apply to the experimental situation of Ref. [14], which we model.

Last, we need to specify the boundary and starting conditions. At time 0 all particles are ordered on a square lattice pointing in random directions. The particles move within a square box. When they hit the boundaries, they are redirected in a random direction away from the wall. The size of the box in the experiments of Ref. [14] is similar to the one of our simulation box for which reason there is no need to consider periodic boundary conditions.

In fact, wall interactions of active particles is a highly discussed topic [31][126]. As shown in Ref. [31], the detention time can be extended significantly but also reduced, such that it almost vanishes, depending on the propulsion mechanism of the particle. We tested the scenario when the particles stick to the wall for some finite time. In this case cluster aggregation emerges at the walls. This, however, has not been observed in experiments, for which reason we chose the random boundary condition. A more detailed description of the wall-particle interaction could be an interesting extension of our work.

4.3.4. Numerical implementation

We implemented a numerical solution of the Langevin equations in a two-dimensional square simulation box. To study different area fractions σ , we always use 800 particles and adapt the box size. In two dimensions, the moving direction is controlled by one angle, which we call φ . With $\mathbf{e} = [\cos(\varphi), \sin(\varphi)]$ the equations (4.3) and (4.4) are integrated by an Euler scheme:

$$\begin{aligned}\varphi_i(t + dt) &= \varphi_i(t) - dt\zeta_{\text{rot}} [-\sin(\varphi), \cos(\varphi)] \cdot \nabla c(\mathbf{r}_i) + \sqrt{2dtD_{\text{rot}}}\mathcal{N}_{\text{rot}}, \\ \mathbf{r}_i(t + dt) &= \mathbf{r}_i(t) + dt[v_0\mathbf{e}_i - \zeta_{\text{tr}}\nabla c(\mathbf{r}_i)] + \sqrt{2dtD_{\text{rot}}}\mathcal{N}_{\text{tr}}\end{aligned}$$

where we made use of equation (2.51). After updating the position \mathbf{r}_i for each particle i , we check for overlaps with other particles or the wall. The hardcore interaction that we apply acts only on particles with distance $|\mathbf{r}_i - \mathbf{r}_j| < 2a$, i.e., it is strictly short-ranged. The systems we study contain typically large clusters, which implies many particle-particle interactions. To resolve them accurately, we apply a small time step of $dt = 5 \cdot 10^{-6}$ sec, which makes the hard-core interactions the numerically most expensive part of the program. Naively coding, for each time step the hard-core interactions have numerical complexity $O(N^2)$. To reduce it, we calculate so-called *neighbor lists*. To this end, we subdivide the box in smaller boxes with width $2a$ and assign each particle to one of these boxes [with complexity $O(N)$]. Then, neighbors for a particle i are in one of the 8 neighboring boxes, each of which maximally contains one particle (given that there are no overlaps). Hence, the total numerical complexity to search for possibly overlapping particles is $O(N + 8N) = O(N) < O(N^2)$. For the $\nabla c(\mathbf{r}_i)$ term, we need to consider the contribution of each particle j (see Eq. 4.7) due to the long-ranged nature of the interactions. Hence, the numerical complexity is necessarily $O(N^2)$. However, we perform the update of $c(\mathbf{r}_i)$ only every 50th time step saving computational time again.

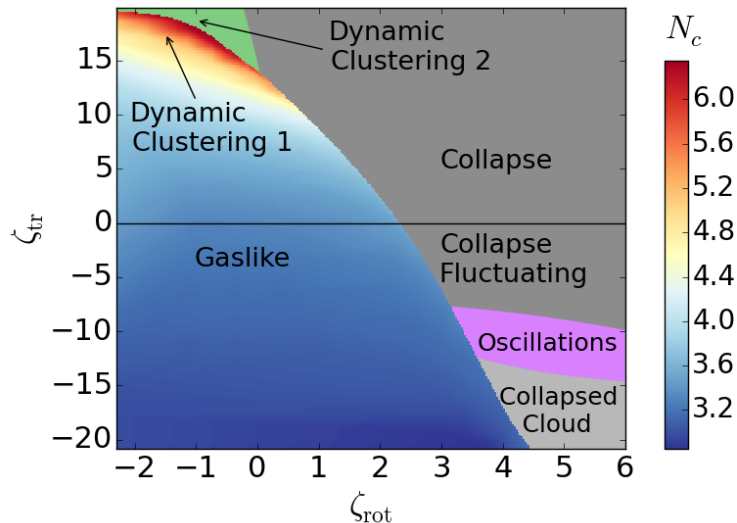


Figure 4.2.: Full state diagram ζ_{tr} versus ζ_{rot} at $Pe = 19$ and density $\sigma = 0.05$. More details are given in the main text.

4.4. Statediagram: Overview of the phenomenology

First, we concentrate on the state behavior of our system at low area fraction $\sigma = 0.05$. If not stated otherwise, throughout this thesis we set $Pe = 19$, which is a typical value in experiments [14]. We have checked that the state diagram of Fig. 4.2 does not change qualitatively for sufficiently large Péclet numbers. Only the parameter regions in ζ_{rot} and ζ_{tr} , where the states are found, are different. This will be discussed in greater detail in Sec. 4.5.3. In addition, we will show in Sec. 4.5.2 that increasing the area fraction also does not change the system's behavior qualitatively, as long as phase separation does not occur.

In Fig. 4.2 we depict the state diagram of the two phoretic parameters ζ_{rot} and ζ_{tr} . We find that, for ζ_{rot} and ζ_{tr} both positive, a sudden transition occurs from a gaslike to a collapsed state, in which all particles are packed into one single cluster. This behavior is reminiscent of the chemotactic collapse in bacterial systems [41, 127]. For $\zeta_{rot} > 0$ and $\zeta_{tr} < 0$ we find the collapse to become unstable. For ζ_{rot} sufficiently large and increasingly negative ζ_{tr} we traverse the following collapsed states:

- *Fluctuating collapse*: Some particles at the rim of the collapsed cluster occasionally leave it
- *Oscillations*: The collapsed cluster pulses with some regular frequency ω_{max} meaning that it breaks and regroups periodically in time

- *Collapsed cloud*: The particles gather in a collapsed cluster, their mutual distance increases when approaching the rim of the cluster as shown in Fig. 4.14(b)

For $\zeta_{\text{rot}} < 0$ and $\zeta_{\text{tr}} > 0$, when rotational diffusiophoresis acts repulsively, we find dynamic clustering as observed in experiments [14]. As we will see in Sec. 4.5, using the shapes of the cluster-size distribution functions in the stationary state, we can distinguish between three cluster states, namely gaslike (blue in Fig. 4.2), dynamic clustering 1 (orange and red), and dynamic clustering 2 (green). To determine the mean cluster size N_c , we define a cluster as an assembly of more than two colloids and average over many snapshots at different times. Thus, by definition $N_c \geq 3$. In Fig. 4.3 we illustrate typical particle configurations for increasing translational diffusiophoretic parameter ζ_{tr} and $\zeta_{\text{rot}} < 0$. At $\zeta_{\text{tr}} = 0$ (upper left) the active colloids hardly cluster since there is no phoretic attraction between them. They assume a gaslike state with a mean cluster size N_c close to 3. In contrast, at large ζ_{tr} (bottom right) the system collapses into a single large cluster similar to the chemotactic collapse which occurs in bacterial systems (see Sec. 3.1). In between, we observe dynamic clustering (Fig. 4.3 top right and bottom left) with many motile clusters that strongly fluctuate in shape and size in time.

In the following two sections we characterize the dynamic clustering states and collapse regimes in detail.

4.5. Gas phase, Dynamic clustering 1 and 2

We here introduce the gaslike state as well as dynamic clustering 1 and 2. We start in the dilute regime and later show how a larger area fraction σ , which we also call density in the following, effects the states.

4.5.1. Dilute regime: $\sigma = 5\%$

Inspecting the state diagram 4.2 at the top left, for small or even negative phoretic parameters the system assumes a gaslike state with mean cluster size N_c close to 3. The active colloids hardly cluster since there is no phoretic attraction between them. At $\zeta_{\text{rot}} = 0$ the maximal dynamic cluster size just before the collapse is $N_c \approx 5$. The case $\zeta_{\text{rot}} > 0$ will be treated in the following section “Collapse regimes”. Here, we consider the case $\zeta_{\text{rot}} < 0$ and $\zeta_{\text{tr}} > 0$ in which dynamic clustering occurs. Due to $\zeta_{\text{rot}} < 0$ active particles rotate away from chemical sinks and thus an effective repulsion is introduced. On the other hand, due to $\zeta_{\text{tr}} > 0$, it is attracted towards other particles, and, in particular, to clusters. In consequence, an active colloid likely joins a cluster, but soon its swimming direction rotates outwards and the colloid can leave the cluster again if the translational phoretic attraction is not too large. This balance of effective phoretic attraction and repulsion is the cause for pronounced dynamical clustering with large

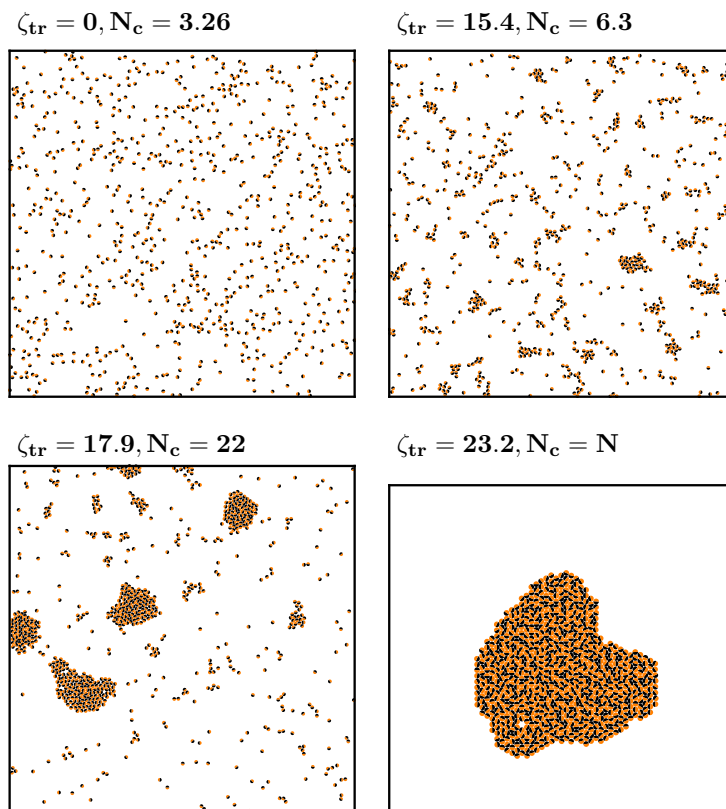


Figure 4.3.: Snapshots of colloid configurations for increasing ζ_{trans} at $\zeta_{rot} = -0.38$ and $Pe = 19$. Top left: gaslike state, top right: dynamic clustering 1, bottom left: dynamic clustering 2, bottom right: collapsed state. N_c is the mean cluster size.

cluster sizes. Interestingly, the state diagram in Fig. 4.2 indicates two clustering states: one where cluster sizes up to 6.5 are observed (see snapshot top, right in Fig. 4.3) and a second clustering state where much larger dynamic clusters occur (see snapshot bottom, left in Fig. 4.3). In Fig. 4.5 (dark curve) the mean cluster-size is plotted against ζ_{tr} . One recognizes the drastic but smooth increase of N_c at the dynamic clustering regimes. However, based on this continuous curve alone, one could not distinguish between two clustering states, one rather needs to dig deeper in the clustering statistics.

Hence, to further quantify the two dynamic clustering states 1 and 2, we determine the cluster-size distribution $P(n)$. In Fig. 4.6(a) we plot it for fixed rotational phoretic parameter $\zeta_{rot} = -0.38$ and increasing translational coupling ζ_{tr} . For pure steric interaction ($\zeta_{tr} = 0$, blue curve), an exponential decay is predominant. In fact, in various tests we have found that this shape is characteristic for the whole gaslike state. Closer to the transition line between dynamic clustering states 1 and 2 in Fig. 4.2, the distribution follows a power-law at small n , before it falls off exponentially [orange and red curves in Fig. 4.6(a)].

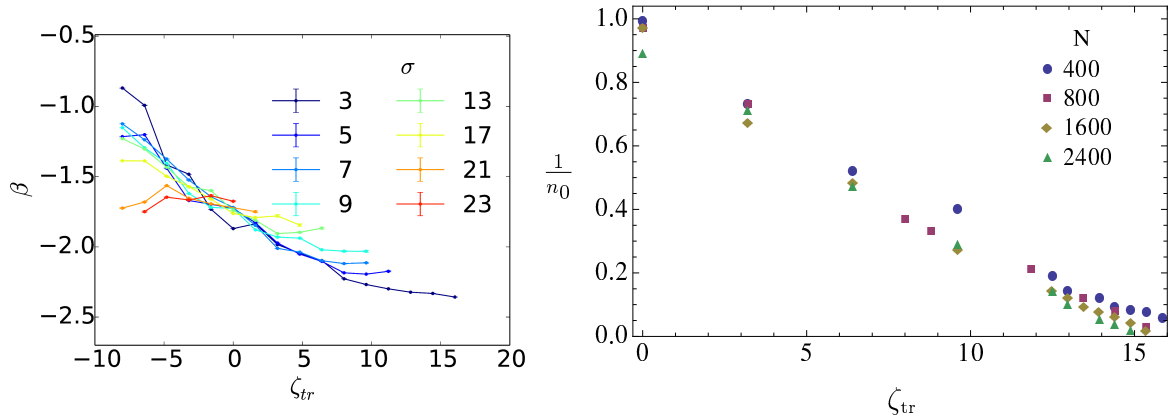


Figure 4.4.: Left: The exponent β from Eq. (4.9) vs. ζ_{tr} in the gaslike and dynamic clustering 1 regime for various area fractions σ . Right: Inverse cut-off parameter $1/n_0$ of the cluster size distribution function $P(n) = c_0 n^{-\beta} \exp(-n/n_0)$ plotted versus ζ_{tr} . Results are shown for different system sizes with total particle number N always at the same area fraction of 5%.

Indeed, in the gaslike and dynamic clustering 1 states we can fit our results by:

$$P(n) = c_0 n^{-\beta} \exp(-n/n_0) \quad (4.9)$$

with exponent $\beta = 2.1 \pm 0.2$. In the gaslike state and in particular for $\zeta_{tr} < 0$ the exponent is slightly smaller than in the dynamic clustering regime as can be seen in Fig. 4.4 on the left. Furthermore, β decreases for more negative ζ_{rot} . In the gaslike state n_0 is small and the exponential dominates [blue and gray curves in Fig. 4.6(a)]. In the dynamic clustering state 1, n_0 is large and for $n < n_0$ the power-law is observed by the linear decrease in the double-logarithmic plot [orange and red curves in Fig. 4.6(a)]. The fit Eq. (4.9) is robust against increasing particle number. In Fig. 4.4 on the right we plot n_0^{-1} vs. ζ_{tr} in systems with varying particle numbers. We observe that n_0 mostly increases with particle number N , in particular, for $\zeta_{tr} > 10$, where pronounced clustering occurs. Also, the transition to dynamic clustering state 2 is slightly shifted to smaller ζ_{tr} . However, the plot clearly shows that the cluster-size distribution with its distinct regimes, gaslike for small n_0 and dynamic clustering for large n_0 , is a distinct feature of our system which persists also for larger system sizes.

In the dynamic clustering state 2 the cluster-size distributions develop an inflection point [green curves in Fig. 4.6(a)], which we fit by a sum of two power-law-exponentials:

$$P(n) = c_1 n^{-\beta_1} \exp(-n/n_1) + c_2 n^{-\beta_2} \exp(-n/n_2) \quad (4.10)$$

with $\beta_1 = 2.1 \pm 0.2$ and $\beta_2 \approx 1.5$. This defines the dynamic clustering state 2, where very large clusters coexist with smaller ones and individual particles. The transition in the cluster-size distribution is observed for all negative ζ_{rot} .

Note that screening of the chemical field within clusters in our model is essential for dynamic clustering. As shown in Sec. 4.8, without screening the clustering state 2 disappears completely.

4.5.2. Dynamic clustering for varying area fractions σ

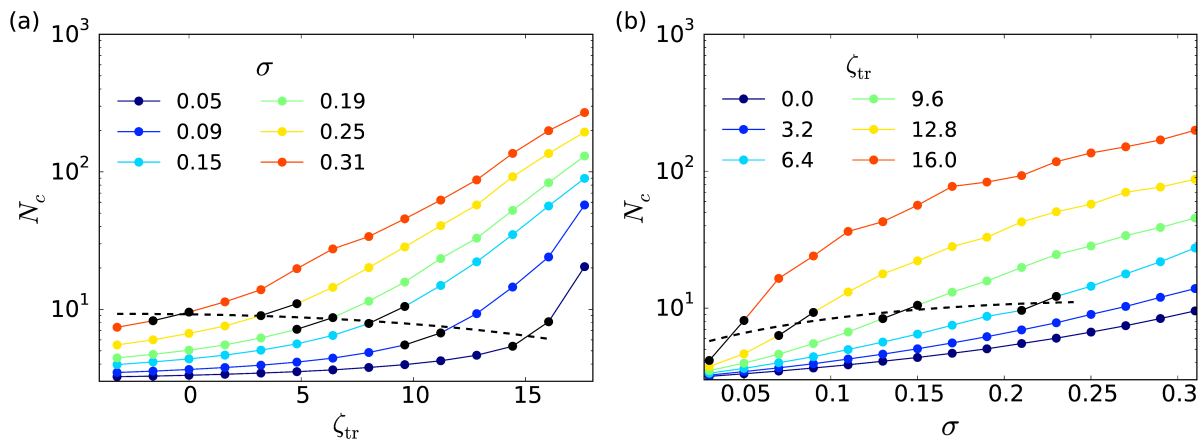


Figure 4.5.: (a) Mean cluster size N_c plotted against ζ_{tr} for different areal fractions σ . (b) N_c plotted against σ for different ζ_{tr} . In both plots the dashed line indicates the transition between dynamic clustering states 1 and 2. The rotational diffusiphoretic parameter is $\zeta_{rot} = -0.38$.

In Fig. 4.5(a) we plot the mean cluster size N_c against ζ_{tr} at fixed area fraction σ . The dashed line roughly indicates the transition between dynamic clustering states 1 and 2. In the case of lowest density $\sigma = 0.05$, N_c grows strongly when entering the regime of dynamic clustering 2. The mean cluster sizes increase with density and the transition point between the two dynamic clustering states is strongly shifted to smaller ζ_{tr} . Moreover, at larger densities the growth of N_c at the transition point becomes smoother. In Fig. 4.6(b) we plot the cluster-size distributions for $\sigma = 0.19$. Compared to $\sigma = 0.05$ both dynamic clustering states occur at smaller phoretic strength ζ_{tr} and the main signature of dynamic clustering state 2, the inflection point, is less pronounced. The exponents in the power-law-exponential fits of Eqs. (4.9) and (4.10) are smaller compared to $\sigma = 0.05$. We find $\beta = 1.7 \pm 0.15$ in the dynamic clustering state 1 and $\beta_1 = 1.7 \pm 0.2$ and $\beta_2 = 1.1 \pm 0.2$ for dynamic clustering 2.

In Fig. 4.5(b) we plot N_c versus density σ at different phoretic strengths ζ_{tr} . As before, mean cluster sizes grow with increasing σ and ζ_{tr} . Note, when the strengths of phoretic forces increase, the curvature of the curves in the semi-logarithmic plot changes. For small ζ_{tr} we observe a convex shape, while at larger ζ_{tr} it becomes concave.

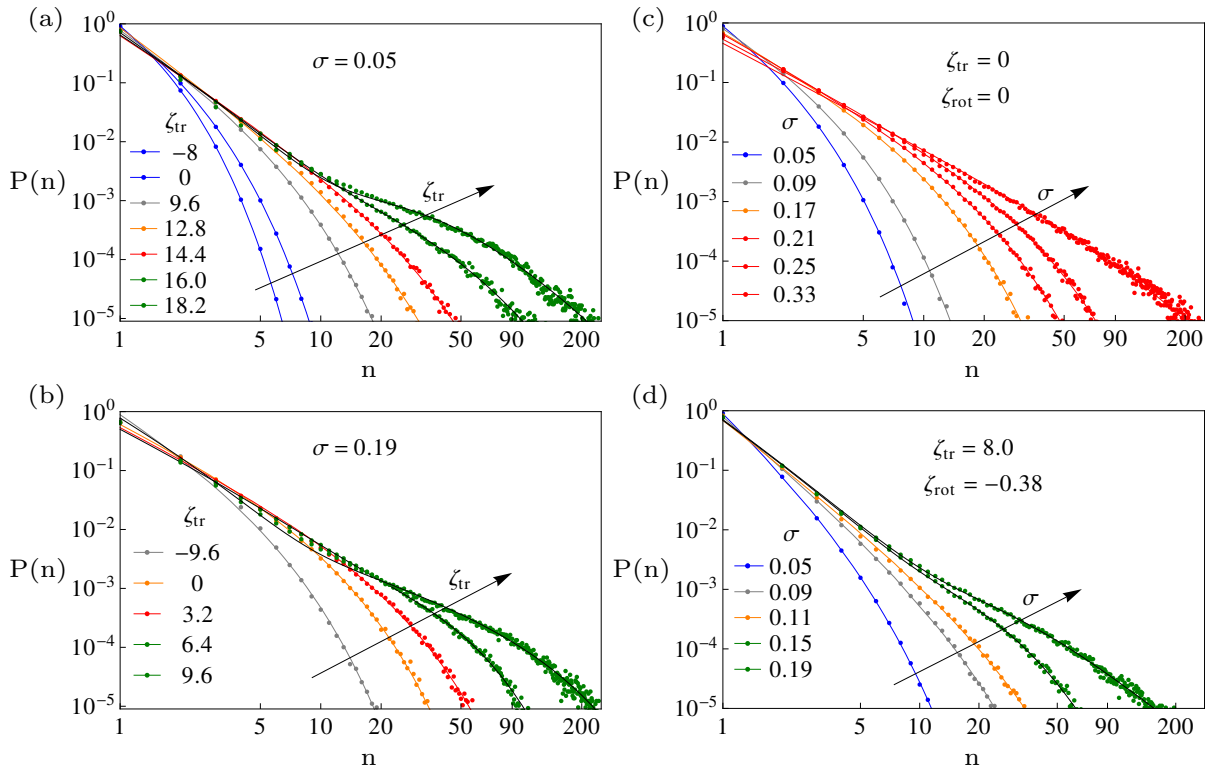


Figure 4.6.: Cluster-size distribution functions for varying ζ_{tr} at densities (a) $\sigma = 0.05$ and (b) $\sigma = 0.19$ and for different densities (c) without phoretic interactions ($\zeta_{tr} = \zeta_{rot} = 0$) and (d) at moderate phoretic interactions with $\zeta_{tr} = 8.0$ and $\zeta_{rot} = -0.38$. Furthermore $\zeta_{rot} = -0.38$. Color code: blue/gray: gaslike state; orange/red: dynamic clustering 1; green: dynamic clustering 2

Furthermore, in Fig. 4.6 we compare the case without phoretic interactions (c) to a case with moderate phoretic strength (d). While in the latter, for increasing density σ a transition between the two dynamic clustering states occurs, in the first, no curve with inflection point appears (compare also their derivatives in Fig. 4.7). Hence, when particles interact only by a repulsive hard-core potential, no dynamic clustering 2 emerges. Indeed, we can fit all curves by the power-law exponential curve $P(n) = c_0 n^{-\beta} \exp(-n/n_0)$ with exponent $\beta \approx 1.77 \pm 0.05$. The distributions approach a clear power-law at large densities. At even larger densities phase separation into large clusters with a gaslike phase in between occurs, a situation which we discussed in Sec. 2.2.3. In Ref. [128] it is shown that there is a sudden transition to the phase separation state, possibly a first order phase transition.

We conclude that the dynamic clustering 2 state is unique to phoretic systems and its occurrence indicates that phoretic interactions are present.

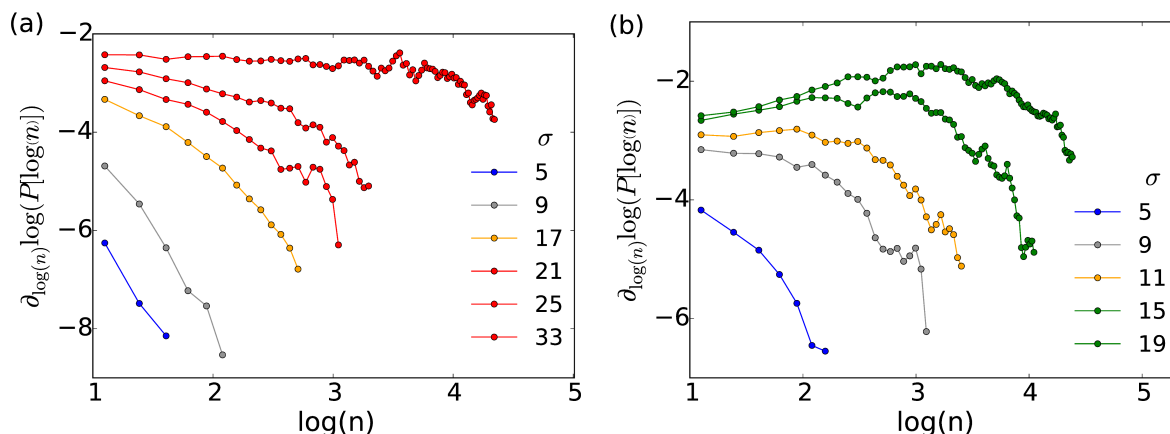


Figure 4.7.: Derivatives of cluster-size distribution functions in Fig. 4.6(c) and (d). We see that without phoresis in (a) the curves approach a constant whereas in the phoresis case there is a clear maximum in the dynamic clustering 2 state.

4.5.3. Dynamic clustering for varying Péclet number

In the experiment Ref. [14] the arguably most surprising result is the proportional relation of Péclet number and mean cluster size, i.e., $Pe \sim N_c$. In Sec. 2.2.3 we have presented the case of purely active and repulsive particles, in which such a relation has been rationalized. However, in the dilute case of area fraction $\sigma = 0.05$ there is no significant clustering without phoresis (compare Fig. 4.2) irrespective of the Pe-number.

In Fig. 4.8 we choose $\zeta_{\text{rot}} = -0.38$ as usual and plot the state diagram in the parameters ζ_{tr} and Pe. Clearly, for constant ζ_{tr} large clusters disappear with increasing Pe. Hence, upon fixing the phoretic parameters, we rather find the opposite scaling than in the experiments. Furthermore, from the statediagram 4.8 we extract that sufficiently large activity Pe is necessary for observing dynamic clustering. At small Pe only small cluster sizes occur with increasing ζ_{tr} , while at sufficiently large Pe we observe both dynamic clustering states.

So, how do we rationalize the experimental scaling prediction? The key observation is that, in order to obtain larger swimming velocities of the colloids, the fuel concentration needs to be increased considerably. More fuel leads to a higher reaction rate k on the colloidal surface, and therefore not only to more self-activity, but also to larger phoretic forces by virtue of Eq. (4.7). This is reflected in our rescaling of the parameters ζ_{rot} and ζ_{tr} since the rescaled phoretic parameters depend linearly on k . With c_0 denoting the fuel concentration, we therefore not only have $Pe \sim c_0$ [10], but also $\zeta_{\text{tr}} \sim \zeta_{\text{rot}} \sim k \sim c_0$. With this, the linear dependence of the parameters Pe, ζ_{tr} , and ζ_{rot} on c_0 defines a line in the parameter space. In this space the dynamic clustering states 1 and 2 are separated by a plane. We choose different lines which always hit the transition plane and plot in

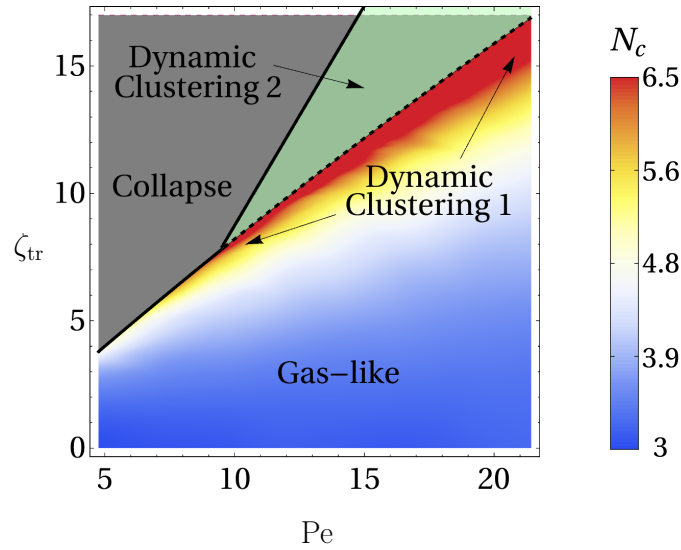


Figure 4.8.: State diagram plotting mean cluster size N_c against Péclet number Pe and chemotactic control parameter ζ_{tr} . $\zeta_{rot} = -0.38$. The color code indicates the mean number of particles N_c in a dynamic cluster.

Fig. 4.9 the mean cluster size N_c versus Pe along the lines. The blue and purple curves show the strong increase of N_c when the clustering state 2 is entered, since the respective lines hit the transition plane under angles closer to 90° . Making this angle smaller, the increase is less steep. In particular, the green graph shows an almost linear increase of N_c in the Pe range from 10 to 20. Concluding this discussion, Fig. 4.9 demonstrates that, depending on the exact relations of fuel concentration, activity and phoresis, the Pe vs. N_c plot might take very different forms. In particular, faster than linear increases with rapid transitions from dynamic clustering 1 to 2 are predicted by our model.

4.6. Collapse Regimes

For sufficiently large ζ_{tr} or ζ_{rot} all N particles in the system collapse and accumulate in one single cluster (see Fig. 4.3, bottom right). To quantify the crystalline hexagonal order in such a cluster, we introduce the global 6-fold bond orientational parameter

$$q_6 := \left| \frac{1}{N} \sum_{k=1}^N q_6^{(k)} \right| \in [0, 1] \quad \text{with} \quad q_6^{(k)} := \frac{1}{6} \sum_{j \in \mathcal{N}_6^{(k)}} e^{i6\alpha_{kj}}. \quad (4.11)$$

Here, $\mathcal{N}_6^{(k)}$ is the set of six nearest neighbors of particle k and α_{kj} is the angle between the vector connecting particle k to j and some prescribed axis [102]. The local bond

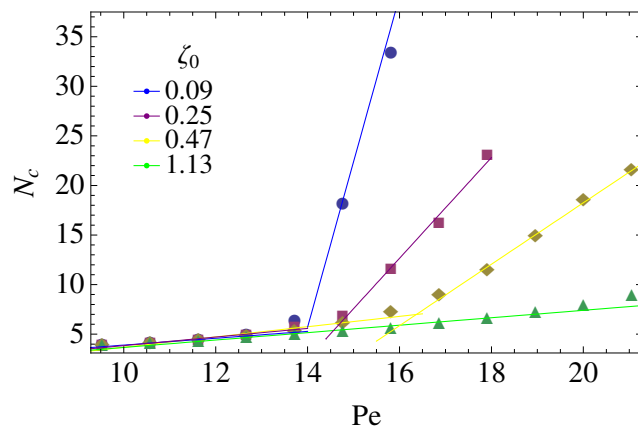


Figure 4.9.: Mean cluster size N_c versus Pe for different lines in the full parameter space defined via a parametrization with $x \in [0, 1]$. We vary Pe as in experiments of Ref. [14], $Pe = 9.5 + 11.5x$, and choose $\zeta_{tr} = 4.8 + 16.6x$ and $\zeta_{rot} = -0.16 - \zeta_0 x$, where the parameter ζ_0 defines the different graphs. The transition between clustering states 1 and 2 roughly occurs at the intersection of the two straight lines.

parameter $q_6^{(k)}$ becomes one if all six nearest neighbors form a regular hexagon around the central colloid and the global order parameter becomes one in a hexagonal lattice.

We now use the temporal behavior of q_6 to identify different regimes in the collapsed state, as indicated in the state diagram of Fig. 4.2. In Fig. 4.10(a) we plot q_6 versus time for several ζ_{tr} . We set $\zeta_{rot} = 4.5$ to a sufficiently large value to guarantee the collapse of the system for all chosen ζ_{tr} . For positive ζ_{tr} we find the order-parameter value $q_6 \approx 0.89$ nearly constant in time. In this situation all particles are packed in one crystalline cluster and q_6 is only smaller than 1 since colloids at the rim of the cluster are not surrounded by six particles on a hexagon. Already for $\zeta_{tr} = 0$ small fluctuations in the order parameter are visible. The cluster is no longer static. It even can become more circular in shape and q_6 assumes values above 0.89. The fluctuations increase for $\zeta_{tr} < 0$, i.e., when the particles effectively repel each other due to translational phoretic motion. Single particles or even clusters occasionally leave the main large cluster and rejoin it after a while. For decreasing ζ_{tr} the fluctuations in q_6 strongly increase. For example, for $\zeta_{tr} = -6.4$ the main cluster's integrity is occasionally disrupted, which is reflected by a q_6 significantly varying in time.

Upon further decreasing ζ_{tr} one enters a regime, where these fluctuations transform into surprisingly regular oscillations, which marks the oscillation regime in the state diagram of Fig. 4.2. The origin of these oscillations in q_6 is the following cyclic process: one large cluster evolves dynamically (large q_6), it resolves and particles disperse (small q_6), they rejoin to form the cluster again, and so on. More precisely, the cluster oscillates between a crystalline structure and a cloud of confined colloids. In the crystalline cluster the diffusiophoretic interaction is strongly screened and the particles are not perfectly

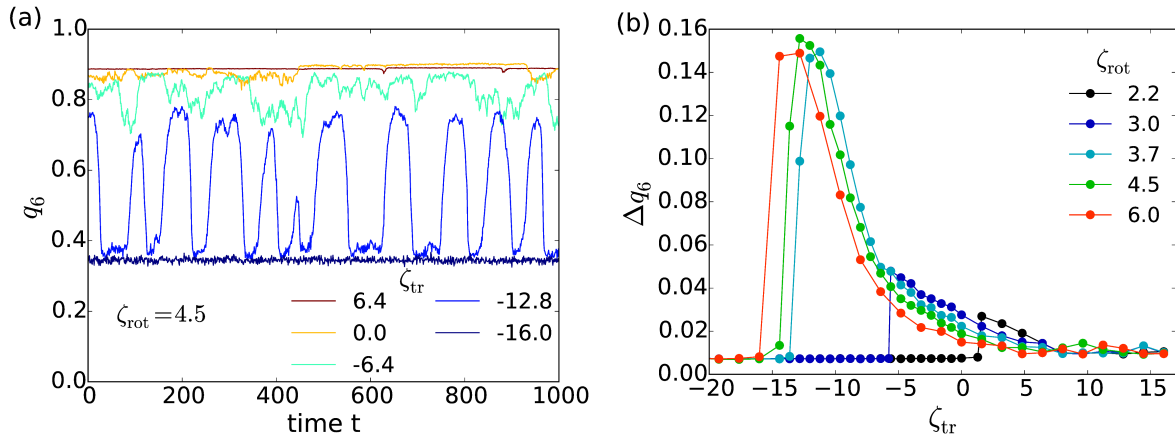


Figure 4.10.: (a) Time evolution of the bond orientational parameter q_6 for different ζ_{tr} . Further parameters are $Pe = 19$, $\zeta_{rot} = 4.5$, and $\sigma = 0.05$. (b) Standard deviation Δq_6 of the fluctuating q_6 plotted versus ζ_{tr} for different ζ_{rot} . The curve at $\zeta_{rot} = 4.5$ quantifies the fluctuations in the graphs of (a).

oriented towards the cluster center. Thermal fluctuations locally disturb the hexagonal packing such that the screening is weakened. Consequently, the repulsion due to translational diffusiophoresis becomes more long-range. This destabilizes the cluster, which appears more like a cloud [a situation similar to Fig. 4.14(b)]. Now, the long-range diffusiophoretic interaction orients all particles back to the cloud center and the compact cluster forms again. Therefore, essentially the pulsating takes its origin in two different time-scales with which the particles respond to a sudden change of ∇c . The translational repulsion acts immediately, whereas the orientational attraction acts only after a typical reorientation time.

For very negative ζ_{tr} no oscillations occur any more. The translational repulsion forces are strong and lead to separation of particles, as shown in the snapshot of Fig. 4.14(b). In this collapsed cloud the hexagonal bond order nearly vanishes leading to $q_6 \approx 0.35$, which is close to the value $q_6 = 1/3$ for systems with homogeneous particle distribution.

To quantify the fluctuations of the bond orientational order parameter q_6 , we plot its standard deviation $\Delta q_6 := [(\langle (q_6 - \langle q_6 \rangle)^2 \rangle)]^{1/2}$ in the full range of ζ_{tr} in Fig. 4.10(b). For large values of ζ_{rot} fluctuations continuously increase with decreasing ζ_{tr} and then when entering the collapsed-cloud regime a sharp decrease occurs. However, the fluctuations do not indicate the transition to the oscillatory regime. The dependence on ζ_{tr} is smooth at the transition between fluctuating and oscillating clusters. Note that for $\zeta_{rot} = 2.2$ and 3.0 the sharp drop with decreasing ζ_{tr} indicates the transition into the gaslike state.

To identify the oscillating regime we determine the power spectrum of the bond orientational parameter. For this purpose, we first define the time-autocorrelation function

$$C(j\tau) = \frac{1}{n} \sum_{i=1}^n \frac{[q_6(t_i + j\tau) - \langle q_6 \rangle][q_6(t_i) - \langle q_6 \rangle]}{(\Delta q_6)^2}. \quad (4.12)$$

Here, $\{t_1, \dots, t_n\}$ is a set of equally spaced time points from the stationary state with n typically around 10000, $\tau = t_i - t_{i-1}$, and j ranges from 1 to 1000. We perform a discrete Fourier transform,

$$Q_6(\omega) = \sum_{j=1}^k C(j\tau) \exp(-i\omega j\tau), \quad (4.13)$$

which, according to Wiener-Khinchine's theorem, is equal to the power spectrum of q_6 . The results for different ζ_{tr} are plotted in Fig. 4.11(a). We fit the spectrum with a non-normalized Gaussian function and detect its maximum at the position ω_{max} . In the fluctuating-cluster regime no peak in the power spectrum can be distinguished, rather more, the curve for $\zeta_{\text{tr}} = -3.2$ decreases monotonically. By contrast, in the oscillating-cluster regime a clear maximum at non-zero frequency ω_{max} exists. We identify the oscillation state in the state diagram if $\omega_{\text{max}} > 0.01$. This value is slightly larger than zero, in order to being able to clearly identify a maximum. In Ref. [40] the authors formulated continuum equations for diffusiophoretically coupled active colloids. In the case where the diffusiophoretic translational velocity acts repulsively, i.e., for $\zeta_{\text{tr}} < 0$, they predict an instability with the onset of spontaneous oscillations. We have shown that oscillations persist in steady state in a certain region in the state diagram.

As it turns out, activity, rather than phoresis, determines the frequency of the pulsating cluster. In Fig. 4.11(b) we plot ω_{max} versus ζ_{tr} . From above (fluctuating cluster) and from below (collapsed cloud) a sharp increase of ω_{max} indicates the onset of the oscillation regime. The curves for ω_{max} display a plateau-like maximum with a value essentially independent of ζ_{rot} . For example, the curves in Fig. 4.11(b) belong to $\text{Pe} = 19$ and we find $\omega_{\text{max}} \approx 0.012 \pm 0.002$ for the maximum value. Indeed, the oscillation frequencies are strongly determined by the activity of the particles. In the inset of Fig. 4.11(b) we plot the maximum value of ω_{max} versus Pe . Beyond the regime where thermal fluctuations dominate, which is set by a defined threshold value $\text{Pe} \approx 20$, the characteristic frequency exhibits a nearly linear increase in Pe . So, the oscillations become faster if the active colloids are faster.

We note, that upon increasing Pe the phoretic strengths need to be adjusted as well to reach the oscillation state. This common scaling of the parameters Pe , ζ_{rot} and ζ_{tr} was rationalized in Sec. 4.5.3.

4.7. Relation to the Keller-Segel model

Considering Eq. (4.3) (without active term) and (4.6), our model for phoretic colloids is reminiscent of the Keller-Segel model (see Sec. 3.1). Indeed, in Ref. [129] it was shown

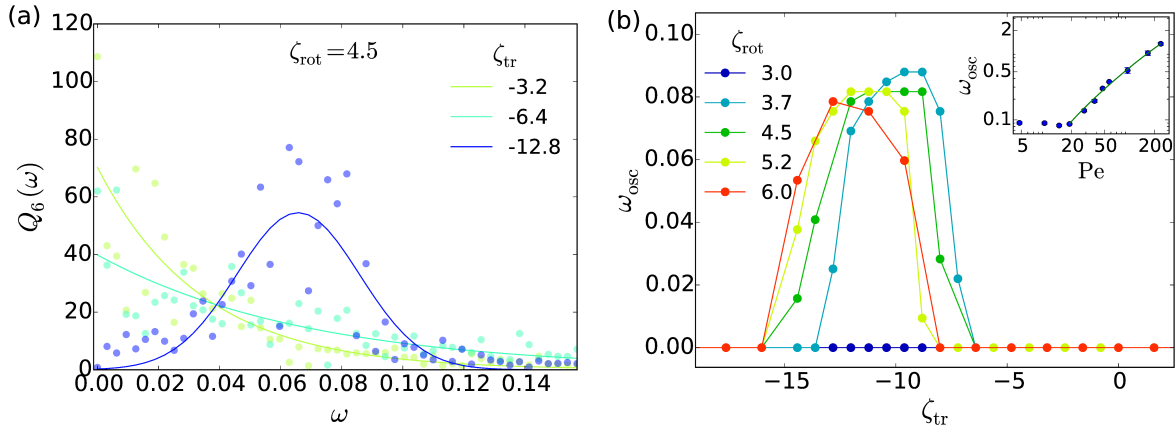


Figure 4.11.: (a) The power spectrum $Q_6(\omega)$ of the bond orientational parameter plotted against frequency ω (symbols) for different ζ_{tr} at $\zeta_{rot} = 4.5$. The lines are fits with a non-normalized Gaussian distribution in order to determine the characteristic frequency ω_{max} . (b) Characteristic frequency ω_{max} of the oscillating cluster plotted against ζ_{tr} . Inset: ω_{max} versus Péclet number Pe in a double logarithmic plot. The error bars show the standard deviation of ω_{max} of the maximum values for each Pe .

that such a system can be mapped to the Keller-Segel setup assuming a typical mean field assumption, according to which the two-body position probabilities factorize. However, in our setup we also consider activity and rotational phoresis, which leads to an additional SDE 4.4 for the direction angle φ . In this section, we show how our Langevin equations transform to the celebrated Keller-Segel model by means of a moment expansion. Then, we discuss the implications for our colloidal system.

4.7.1. Mapping of the colloidal model to the Keller-Segel equations

First, we transform the equations 4.3 and 4.5 to their assigned Fokker-Planck equation:

$$\begin{aligned} \partial_t P(\mathbf{e}, \mathbf{r}, t) = & -v_0 \nabla \cdot (P\mathbf{e}) + \zeta_{tr} \nabla \cdot (P\nabla c) + D_{tr} \nabla^2 P \\ & + \zeta_{rot} \partial_\varphi [(\partial_\varphi \mathbf{e}) \cdot \nabla c P] + D_{rot} \partial_\varphi^2 P \end{aligned} \quad (4.14)$$

We then derive dynamic equations for the colloidal density $P_0(\mathbf{r}, \mathbf{t}) = \int P(\mathbf{e}, \mathbf{r}, t) d\varphi$, as well as the polar [$\mathbf{P}_1(\mathbf{r}, t) = \int \mathbf{e} P d\varphi$] and the nematic [$\mathbf{P}_2(\mathbf{r}, t) = \int (\mathbf{e} \otimes \mathbf{e} - \frac{1}{2}) P d\varphi$] order parameter.

Integrating Eq. (4.14) over φ leads to

$$\partial_t P_0(\mathbf{r}, t) = -v_0 \nabla \cdot \mathbf{P}_1 + \zeta_{tr} \nabla \cdot (P_0 \nabla c) + D_{tr} \nabla^2 P_0 \quad (4.15)$$

The term with the polarization \mathbf{P}_1 will ultimately lead to renormalized chemotactic and diffusion coefficients. To derive a dynamic equation for \mathbf{P}_1 , we evaluate $\int \mathbf{e} \text{Eq.}(4.14) d\varphi$

and obtain

$$\begin{aligned} \partial_t \mathbf{P}_1(\mathbf{r}, t) = & -v_0 \nabla \mathbf{P}_2 - \frac{v_0}{2} \nabla P_0 + \zeta_{\text{tr}} \nabla (\mathbf{P}_1 \otimes \nabla c) \\ & + D_{\text{tr}} \nabla^2 \mathbf{P}_1 - D_{\text{rot}} \mathbf{P}_1 + \zeta_{\text{rot}} (\mathbf{P}_2 - \frac{1}{2} P_0 \mathbb{1}) \nabla c \end{aligned} \quad (4.16)$$

where we used $\partial_\varphi^2 \mathbf{e} = -\mathbf{e}$ to simplify the rotational diffusion term and $\partial_\varphi \mathbf{e} \otimes \partial_\varphi \mathbf{e} = \mathbb{1} - \mathbf{e} \otimes \mathbf{e}$ for the term with ζ_{rot} as coefficient. As in the derivation of Sec. 2.2.3 we neglect gradients of \mathbf{P}_1 and \mathbf{P}_2 . However, in our case rotational diffusiophoresis contributes a term proportional to \mathbf{P}_2 . There is no such term in the expansions of Ref. [37] and [9], which is why the dynamic equation of the nematic order parameter can be neglected there. In Ref. [112] it is considered, and in fact our expansion is very much inspired by Ref. [112]. So, we determine the dynamic equation for the nematic order parameter using $\int (\mathbf{e} \otimes \mathbf{e} - \frac{\mathbb{1}}{2}) \text{Eq. (4.14)} d\varphi$. Concentrating on the relevant terms, and using the definition $\mathbf{P}_3(\mathbf{r}, t) = \int (\mathbf{e} \otimes \mathbf{e} \otimes \mathbf{e} - \frac{3}{4} \mathbf{e} \mathbb{1}) P d\varphi$. where $\mathbf{e} \mathbb{1} := \frac{1}{3} (e_\alpha \delta_{\beta\gamma} + e_\beta \delta_{\alpha\gamma} + e_\gamma \delta_{\alpha\beta})$, we obtain:

$$\begin{aligned} \partial_t \mathbf{P}_2(\mathbf{r}, t) = & \nabla(\dots) + \zeta_{\text{tr}} \mathbf{P}_2 \nabla^2 c \\ & - 4D_{\text{rot}} \mathbf{P}_2 + \zeta_{\text{rot}} (2\mathbf{P}_3 - \frac{3}{2} \mathbf{P}_1 \mathbb{1} + \mathbb{1} \otimes \mathbf{P}_1) \nabla c. \end{aligned} \quad (4.17)$$

Now, we close the hierarchy of moment equations by setting $\mathbf{P}_3 = 0$. Furthermore, as in Sec. 2.2.3 we neglect the time derivative of the first and second moments on time scales much larger than the rotational diffusion time $1/D_{\text{rot}}$, discard gradients of \mathbf{P}_1 and of \mathbf{P}_2 in sufficiently dilute suspensions, and also neglect higher-order gradient terms in c . Then we obtain from Eq. (4.17):

$$\mathbf{P}_2 = \frac{\zeta_{\text{rot}}}{8D_{\text{rot}}} (-3\mathbf{P}_1 \mathbb{1} + 2\mathbb{1} \otimes \mathbf{P}_1) \nabla c.$$

We insert this relation into Eq. (4.16). Again, the time derivative is assumed to vanish, gradients of \mathbf{P}_1 and \mathbf{P}_2 are discarded, and we obtain:

$$\begin{aligned} \mathbf{P}_1(\mathbf{r}, t) = & \frac{1}{2D_{\text{rot}}} \left[-v_0 \nabla P_0 - \zeta_{\text{rot}} P_0 \nabla c \right. \\ & \left. + \left(2\zeta_{\text{tr}} \nabla^2 c - \frac{\zeta_{\text{rot}}}{4D_{\text{rot}}} |\nabla c|^2 \right) \mathbf{P}_1 \right] \end{aligned} \quad (4.18)$$

We concentrate here on perturbations around the uniform and isotropic state and therefore neglect in Eq. (4.18) all second-order terms in \mathbf{P}_1 and ∇c . Then the polarization \mathbf{P}_1 just depends on P_0 . We substitute it in Eq. (4.15) to obtain the final equation familiar from the Keller-Segel model:

$$\partial_t P_0 = \zeta_{\text{eff}} \nabla (P_0 \nabla c) + D_{\text{eff}} \nabla^2 P_0. \quad (4.19)$$

Here, $\zeta_{\text{eff}} = \zeta_{\text{tr}} + \frac{\zeta_{\text{rot}} v_0}{2D_{\text{rot}}}$ and $D_{\text{eff}} = D_{\text{tr}} + \frac{v_0^2}{2D_{\text{rot}}}$.

4.7.2. Comparison of mean field equations with simulations

We obtain the Keller-Segel equation (3.1) for the colloidal density ρ with effective chemotactic and diffusion constants. Furthermore the diffusion equation (4.6) can be casted into the second Keller-Segel equation (3.2) by means of the approximation:

$$\rho(\mathbf{r}) = \langle \delta(\mathbf{r} - \mathbf{r}_j) \rangle \approx \frac{1}{N} \sum_{i=1}^N \delta(\mathbf{r} - \mathbf{r}_i),$$

and by setting $\gamma = 0$. As we have discussed in Sec. 3.1, as long as the integration domain is bounded, γ is irrelevant for the collapse behavior.

In two dimensions, the Keller-Segel model exhibits an instability of the uniform state towards a chemotactic collapse when its parameters satisfy $\frac{\zeta_{\text{eff}} k \sigma}{D_c D_{\text{eff}}} > b$, where b is a constant which depends on the geometry of the system (Sec. 3.1). In our unitless parameters the condition becomes

$$\frac{8\pi\sigma(\zeta_{\text{tr}} + \zeta_{\text{rot}}\text{Pe})}{1 + 2\text{Pe}^2} > b. \quad (4.20)$$

Judging from this relation, the transition line between gaslike and the collapsed state for constant Pe parametrized by the parameters ζ_{rot} and ζ_{tr} should be linear. However, for very large $|\zeta_{\text{tr}}|$, the translational phoretic attraction or repulsion between two particles is stronger than the active motion. In such a situation, either particles collapse and never detach again ($\zeta_{\text{tr}} \gg 0$) or they never come close enough to build clusters ($\zeta_{\text{tr}} \ll 0$) irrespective of ζ_{rot} . At the top left and bottom right of the state diagram Fig. 4.2 one clearly distinguishes the initiation of saturation of the transition line. Hence, the prediction of linear dependency can only be valid for not too large $|\zeta_{\text{tr}}|$ and this is indeed approximately the case in Fig. 4.2.

Furthermore, the condition 4.20 does not reproduce the straight transition line in Fig. 4.8. The reason is that at $\zeta_{\text{rot}} < 0$ pronounced clustering occurs before the collapse takes place. When testing the transition for $\zeta_{\text{rot}} > 0$, where dynamic clustering is absent, we indeed find the predicted scaling behavior $\zeta_{\text{tr}} \sim \text{Pe}^2$ and $\zeta_{\text{rot}} \sim \text{Pe}$ of the transition line reproduced. For this purpose, we performed simulations with positive ζ_{rot} and determined the parameters where the collapse occurred. In Fig. 4.12 we plot ζ_{tr} versus Pe^2 for $\zeta_{\text{rot}} = 1.13$. The straight line confirms the expected quadratic behavior. For the inset, we set $\zeta_{\text{tr}} = 0$ and indeed reproduce the predicted linear dependence between ζ_{rot} and Pe.

After all, dynamic clustering cannot be described by the Keller-Segel equation. Clustering occurs when a colloid moves towards the rim of a cluster, then rotates away from it ($\zeta_{\text{rot}} < 0$), and finally a delicate balance between activity and diffusiophoretic attraction sets in: $\text{Pe} \sim \zeta_{\text{tr}} |\nabla c|$. Note that this mechanism crucially depends on ballistic swimming with velocity v_0 . It cannot be described by our Keller-Segel equation since v_0 only appears in effective chemotactic and diffusion parameters, which occur based approximations assuming very long time-scales. Particularly, desintegration of an agglomeration

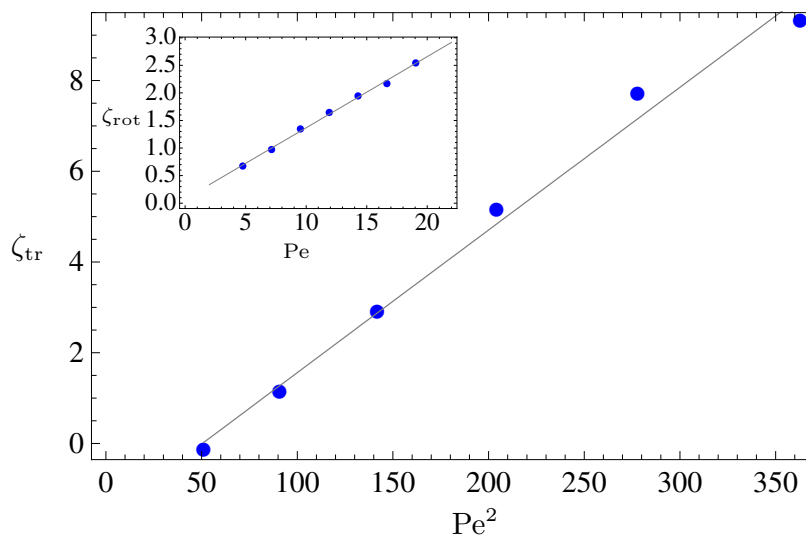


Figure 4.12.: Parameters for which the chemotactic collapse occurs as determined from simulations. Main plot: ζ_{tr} versus Pe^2 at $\zeta_{rot} = 1.13$. Inset: ζ_{rot} versus Pe at $\zeta_{tr} = 0$

occurs only by diffusion, which is controlled by the diffusion constant $D_{eff} \sim Pe^2$. This is the reason that the theoretically predicted collapse line is quadratic in Pe . Assuming that the colloid attaches directly to two particles at the rim of a cluster, we estimate in our reduced units $|\nabla c| \approx 1/(2a/2.33a)^2 = 1/0.73$ and obtain a condition for dynamic clustering: $\zeta_{tr} \approx 0.73Pe$. This simple estimate reproduces the straight transition line between clustering states 1 and 2 in Fig. 4.8 and the region where clustering occurs.

4.8. System without screening

Within a cluster, or more specific, when one particle is closely surrounded by six neighboring particles, the diffusiophoretic interaction between particles is screened. To show the effect of screening, in this section we investigate the system in the absence of it. In this case, the phoretic interactions mediated by c are purely long-ranged.

4.8.1. Dynamic clustering without screening

In Fig. 4.13 we plot the state diagrams Fig. 4.2 and Fig. 4.8 for $\zeta_{tr} > 0$ with the same parameters but without implementing chemical screening in the clusters. The dynamic clustering state 2 vanishes completely and the transition line is shifted to smaller ζ_{tr} . A moderate dynamic clustering still exists with a reduced mean cluster size. Clearly, without chemical screening the diffusiophoretic attraction is stronger, they are purely long-ranged according to Eq. (4.7). Then, a particle arriving at the rim of a cluster

feels each other member and cannot escape any more, even when the cluster is small. Therefore, the chemotactic collapse occurs for smaller ζ_{tr} , which prevents the formation of the clustering state 2.

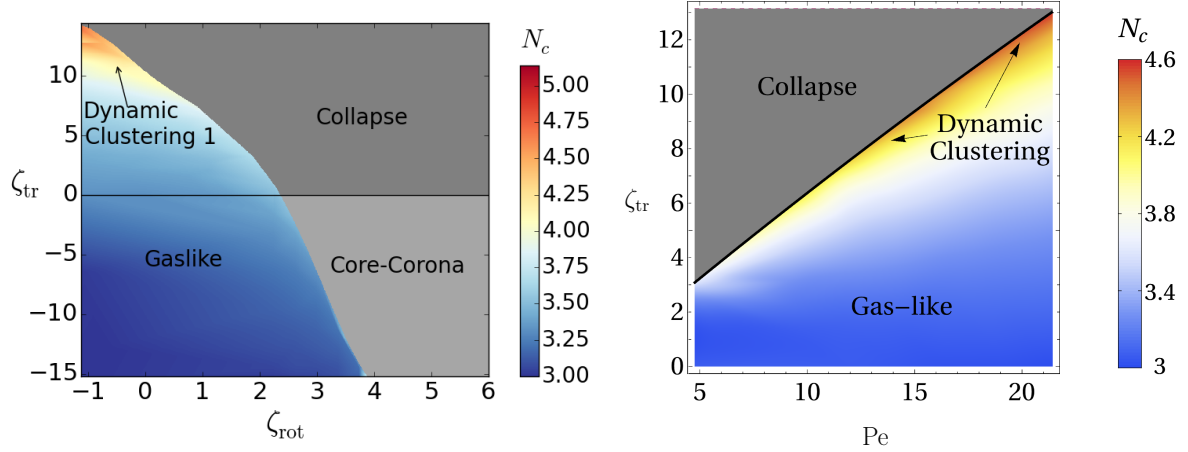


Figure 4.13.: State diagrams ζ_{tr} versus ζ_{rot} (left) and ζ_{tr} versus Pe (right) for the same parameters as Fig. 4.2 and 4.8 when chemical screening in the clusters is not implemented.

4.8.2. Collapse without screening

In the previous section, we have inspected the case $\zeta_{\text{tr}} > 0$ and detected the absence of pronounced dynamic clustering for purely long-ranged interactions. For negative ζ_{tr} the collapsed state also behaves differently. At stationary state, the collapsed cluster has an inner core with radius r_c , where particles are ordered in a two-dimensional hexagonal lattice, surrounded by a corona of particles. The core-corona state, as we call it, is illustrated in Fig. 4.14(a). The core radius r_c becomes smaller with decreasing ζ_{tr} and eventually vanishes. The resulting state resembles very much the collapsed cloud discussed in the case with screening. In Fig. 4.14(b) we show an example, where a compact core is no longer present. So, as long as compact cores in the collapsed state form, screening of the diffusiophoretic interaction leads to fluctuating or oscillating clusters, as we have demonstrated in the previous section, whereas for sufficiently negative ζ_{tr} we observe the static collapsed cloud since screening does not play a role in this configuration.

To quantify the density profile of the core-corona cluster, we determine its center-of-mass location \mathbf{r}_{cm} and calculate the radial distribution function of the particles,

$$g(r) := \frac{1}{r} \sum_{j=1}^N K(r_{jc} - r). \quad (4.21)$$

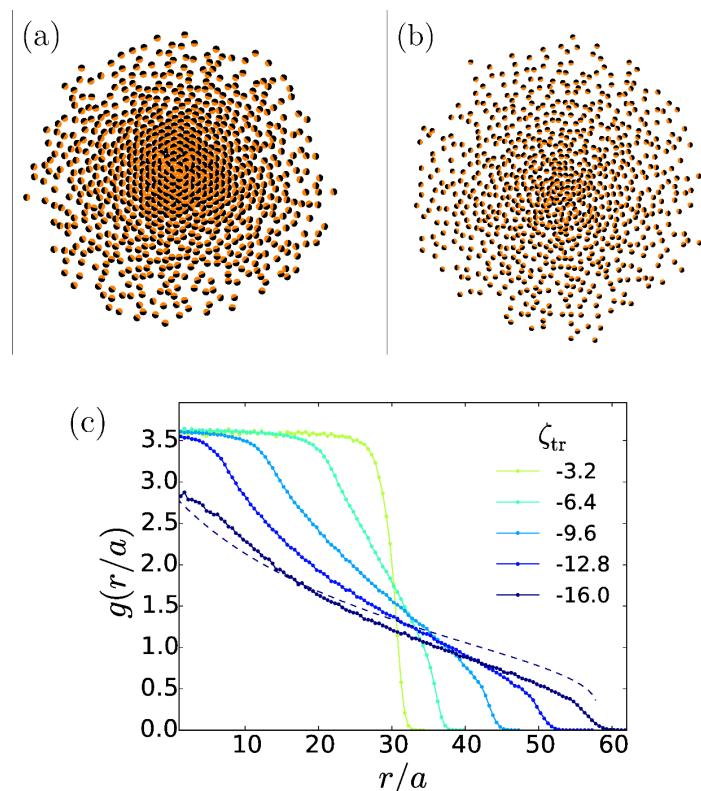


Figure 4.14.: Snapshots of the system in the core-corona state at (a) $\zeta_{\text{tr}} = -6.4$ and (b) $\zeta_{\text{tr}} = -16$. Other parameters are $\text{Pe} = 19$ and $\zeta_{\text{rot}} = 4.1$. (c) Radial particle distribution $g(r)$ plotted for various ζ_{tr} . The dashed line shows an analytic approximation for $\zeta_{\text{tr}} = -16$.

Here,

$$K = \frac{1}{v\sqrt{2\pi}} \exp \left[-\frac{(r_{jc} - r)^2}{2v^2} \right] \quad (4.22)$$

is a 1D Gaussian kernel function with zero mean and width $v = 2a$, where a is the particle radius. Furthermore, $r_{jc} = |\mathbf{r}_j - \mathbf{r}_{cm}|$ is the particle distance to the center of mass. With this definition one obtains $\int g(r)rdr = N$, where N is the total particle number. In Fig. 4.14(c) we plot the radial particle density $g(r)$ for various ζ_{tr} . In the crystalline core at $r < r_c$, $g(r)$ is basically constant. For larger distances r , $g(r)$ drops off, which indicates the increasing distances between particles when approaching the rim of the cluster.

In the following, we seek to quantify $g(r)$ for sufficiently negative ζ_{tr} , where a crystalline core does not exist so that direct contacts between the particle are negligible. We consider the stationary state, where the total velocity of each particle vanishes. Furthermore, we assume that all particles are exactly directed towards the center of the cluster. This is a good approximation in the collapsed cloud state as a closer inspection of the snapshot

in Fig. 4.14(b) reveals (the particles head towards their golden side in the figure). Then, the balance of active and diffusiophoretic velocities for each particle i gives

$$\text{Pe } \mathbf{e}_i = \zeta_{\text{tr}} \nabla_i \sum_{j=1}^N \frac{1}{r_{ij}}, \quad (4.23)$$

where \mathbf{e}_i is a unit vector pointing from particle i to the center of the collapsed cloud and r_{ij} is the distance between particle i and j . Without loss of generality we assume particle i to sit on the y -axis of a cartesian coordinate system at some distance r to the center. Assuming a spherical cluster cloud with radius R , we only consider the y component of Eq. (4.23) and obtain:

$$\begin{aligned} \text{Pe} &= \zeta_{\text{tr}} \partial_r \sum_{j=1}^N \frac{1}{\sqrt{(r - y_j)^2 + x_j^2}} \\ &\approx \frac{\zeta_{\text{tr}}}{\pi a^2} \partial_r \int_0^R \int_0^{2\pi} \frac{g(r') r'}{\sqrt{r^2 + r'^2 - 2 \cos(\phi) r r'}} d\phi dr' \\ &:= F(r) \end{aligned} \quad (4.24)$$

Hence, we search for a radial density distribution $g(r)$ such that the phoretic interactions cancel the active velocity v_0 of every particle.

The corresponding problem in three dimensions is readily solved. In this case, $F_{3d}(r)$ is equivalent to the negative force, which a test particle of unit mass experiences at a distance r from the center of a radially symmetric mass distribution $g_{3d}(r)$. It is well known that

$$F_{3d}(r) = \gamma \frac{M(r)}{r^2}, \quad (4.25)$$

where $M(r) = 4\pi \int_0^r g_{3d}(r') r'^2 dr'$ is the mass inside a sphere of radius r and γ is the gravitational constant. Now, according to Eq. (4.25) a constant gravitational force $F_{3d}(r) = F$ within the whole mass distribution means $M(r) \propto r^2$ which implies $g_{3d}(r) \propto 1/r$. For a uniform mass distribution $g^{\text{hom}}(r) \propto 1$, one obtains $F_{3d}^{\text{hom}} \propto r$, and we can write

$$g_{3d}(r) \propto \frac{F}{F_{3d}^{\text{hom}}(r)}. \quad (4.26)$$

Based on this finding, we suggest an approximate solution for the two-dimensional problem. For a uniform particle density $g^{\text{hom}}(r) \propto 1$, the integral in Eq. (4.24) can be solved and one obtains $F_{2d}^{\text{hom}}(r) = [2\zeta_{\text{tr}} r / (\pi a^2 R)] E[(r/R)^2]$, where $E[m]$ is the complete elliptic integral of the second kind [130]. With $F = \text{Pe}$ we propose in analogy to Eq. (4.26) the approximate solution

$$g(r) = \frac{p \text{Pe}}{1 + F_{2d}^{\text{hom}}(r)}, \quad (4.27)$$

where p is a fitting parameter and the number one in the denominator prevents an unphysical singularity. Fig. 4.14(c) demonstrates that Eq. (4.27) is a good approximation for $g(r)$ determined in our simulations for $\zeta_{\text{tr}} = -16$.

4.9. Cluster dynamics: Fusion and fission rates

Dynamic clustering owes its name to the dynamic nature of the clusters meaning that they constantly assume and release particles. Naturally, this raises the question with which rates agglomeration and dissociation, i.e., fusion and fission, occur.

Cluster-size distribution functions have been studied in a biological context, for example, in Refs. [131–133]. In experiments with a strain of non-chemotactic rod-shaped bacteria, the authors of Ref. [132] measured cluster size distributions for increasing density.¹ For low densities they fit their experimental distributions by a power-law-exponential function, as we have done it for our system. As power-law exponent they obtain $\beta = 1.88 \pm 0.08$ which is comparable to our findings for $\zeta_{\text{tr}} = 0$ (see Fig. 4.4 on the left). The distributions for dynamic clustering 2 are, again as in our case, reproduced by a sum of two power-law-exponential functions. However, in their case a clear maximum emerges for high enough densities, where in our case dynamic clustering 2 is characterized by an inflection point.

In Ref. [134] the authors develop a kinetic model for clustering and predict the distribution functions. They define “reactions” between the clusters by introducing conglomeration and dissociation rates. These quantities can be written as linear functions of a fission function $\rho(n)$, which is the rate with which a cluster or single particle detaches from a cluster of size n , and the fusion rate function $a(n)$, which quantifies the event where a cluster or single particle joins a cluster of size n [131]. Assuming power-law functions for the rate functions [135],

$$\begin{aligned}\rho(n) &= c_1 n^{\gamma_\rho} + c_\rho \\ a(n) &= c_2 n^{\gamma_a} + c_a,\end{aligned}\tag{4.28}$$

Peruani and Bär are indeed able to reproduce the transition from a power-law-exponential to a peaked cluster-size distribution, as observed in the experiments. To do so, the coefficients c_1 and c_2 have to increase with density while the exponents γ_ρ and γ_a are kept constant. In particular, for circular particles in two dimensions one has $\gamma_\rho = \gamma_a = 0.5$. Since particles join or leave a cluster only at its border and fusion as well as fission occur only by physically bumping into the cluster, the rate functions have to grow with the circumference of the cluster $\propto n^{0.5}$.

We study fission and fusion rate functions in our phoretic system at low density $\sigma = 0.05$ and for varying ζ_{tr} . To this end, we take snapshots of our system at different

¹The cluster-size distribution $p(n)$ in Ref. [132] is related to our distribution according to $nP(n) = p(n)$.

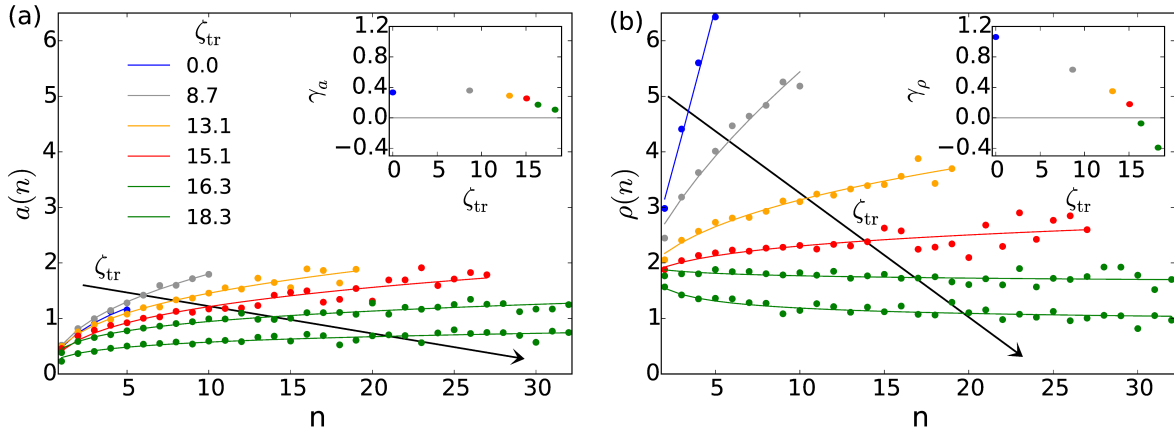


Figure 4.15.: (a) Fusion rate function $a(n)$ for different ζ_{tr} at $\zeta_{\text{rot}} = -0.38$. The solid lines are fits to $c_a + c_2 n^{\gamma_a}$. Inset: γ_a versus ζ_{tr} . (b) Fission rate function $\rho(n)$ for different ζ_{tr} at $\zeta_{\text{rot}} = -0.38$. The solid lines are fits to $c_\rho + c_1 n^{\gamma_\rho}$. Inset: γ_ρ versus ζ_{tr} . The color code refers to the gaslike state (blue, gray), dynamic clustering state 1 (orange, red) and state 2 (green).

times and measure the time intervals between two events, where either a particle or cluster leaves a cluster with size n or merges with it. By averaging over all inverse time intervals, we obtain the respective rate statistics for $a(n)$ and $\rho(n)$. They are plotted in Fig. 4.15 for different ζ_{tr} . For systems with small clusters (gas-like state), we of course obtain little data for the rates at large n . We only plot $a(n)$ and $\rho(n)$, when we have at least 100 data points to average over. Therefore, the curves in Fig. 4.15 do not span the whole size range but cease depending on the mean cluster size.

We find that the rates shown in Fig. 4.15 clearly depend on ζ_{tr} . In particular, the exponents γ_a and γ_ρ plotted in the insets are no longer constant as in the non-phoretic case of [135]. The exponent γ_a [inset of Fig. 4.15(a)] decreases with increasing ζ_{tr} , in particular, in the dynamic clustering 2 state, which is marked in green. The exponent γ_a is always positive meaning that the fusion rates increase with cluster size n . The dependence of the fission rate functions on ζ_{tr} is much more pronounced. The relevant exponent γ_ρ decreases rapidly with increasing ζ_{tr} and becomes negative in the dynamic clustering 2 state as the inset of Fig. 4.15(b) demonstrates. Hence, large clusters have a smaller probability to loose particles than small clusters.

Both exponents, γ_a and γ_ρ , strongly deviate from 0.5 and, therefore, indicate the presence of phoretic interactions. In addition, the exponent γ_ρ of the fission rate $\rho(n)$ clearly signals the transition between the two dynamic clustering states when becoming negative. In contrast to cluster-size distributions, the fission rate is easier to determine since it can be measured locally by monitoring breaking clusters.

4.10. Conclusion

Concluding, we have modeled the collective motion of self-phoretic active colloids. A chemical field mediates diffusiophoretic interactions between the particles. They consist of a translational and an orientational part, which together with the active swimming can act either attractively or repulsively. When they are both attractive, the colloids show a transition from the gas-like to a collapsed state. This behavior is reminiscent of a chemotactic collapse in bacterial systems and, indeed, we established a mapping of our model on the Keller-Segel equations. Hence, the colloidal system mimics chemotaxis in bacterial colonies without relying on a complex signaling pathway necessary for chemotaxis in cells. Thereby, it may help to explore chemotactic structure formation and design novel dynamic patterns in bacterial colonies [51].

By exploring the full state diagram in the translational and rotational phoretic parameters, ζ_{tr} and ζ_{rot} , we have shown that the collapsed state can be further sub-classified by the dynamics of the collapsed cluster. Indeed, its dynamics depends on the translational phoretic strength ζ_{tr} . When particles attract each other ($\zeta_{\text{tr}} > 0$), one large cluster with crystalline order builds up. Gradually decreasing ζ_{tr} to negative values, the colloidal cluster starts to fluctuate strongly and then enters pulsating dynamics, where it oscillates between a compact cluster and a colloidal cloud. Calculating the power spectrum of the bond-orientational order parameter, we were able to determine a characteristic oscillation frequency, which increases with the Peclet number. When the effective repulsion is sufficiently strong, a sharp transition to a static colloidal cloud occurs, where the particles gather in one cluster without crystalline order.

When translational and rotational diffusiophoresis generate counteracting attraction and repulsion, two dynamic clustering states are stabilized very similar to the dynamic clustering observed in the experiments of [14]. In such states large clusters form and break dynamically in time, a property which is a manifestation of the non-equilibrium character of our system. The different states are distinguished by their particular cluster size distribution functions ranging from exponential distributions (gas-phase) to a power-law decay (dynamic clustering 1) up to a distribution with inflection point and large mean value (dynamic clustering 2).

We also studied the dynamic clustering states for increasing densities by determining cluster-size distributions and mean cluster sizes. As expected, we found that dynamic clustering evolves at smaller phoretic strengths. In particular, we showed that dynamic clustering 2 also appears at large densities and only when phoretic interactions are present. So, by determining cluster-size distributions in dense suspensions of active particles, one is able to identify phoretic interactions. Another method is to measure fission and fusion rates for the dynamic clusters, which can be done locally on merging or breaking clusters. The rates even indicate the switch from dynamic clustering 1 to 2. Identifying phoretic interactions in dense suspensions of active colloids is not straight-

forward. In this article we provided methods to do so. It would be interesting to apply them to the experimental system of Ref. [15], where phase separation was observed.

Inference of chemotaxis of the bacteria *E.coli* and *P.putida*

In this chapter, we develop a method to study the tumbling behavior of bacteria based on experimental trajectories. We extend it to define a novel tumble recognizer. Furthermore, we apply it to study chemotaxis as well as chemokinesis for the bacteria *E.coli* and *P.putida*. We start with an introduction and motivation of the topic.

5.1. Introduction

Taxis is the directed motion of a particle along a certain gradient, chemotaxis refers to taxis along chemical gradients. Many species have been shown to perform chemotaxis ([46, 50, 136, 137]), other forms of taxis have also been studied such as gravitaxis [116, 117] or thermotaxis [118]. Even in synthetic systems chemotaxis is possible ([14, 52]). The chemotactic behavior of bacteria is a fascinating topic to study since not only the underlying biochemical signaling pathway but also their active random walk needs to be considered. A very common moving pattern for bacteria is the so-called run-and-tumble random walk. Quantitatively, it was first studied by Howard C. Berg [46] in the early seventies revealing statistics about tumble angles and tumble rates. It was shown that *E.coli* decreases its tumble rate when moving against the chemical gradient direction. Later, the bacterial response to chemical landscapes changing in time and space was studied [47, 48]. In Ref. [51] a bias in the tumble angle was reported, i.e., the mean reorientation angle during tumbling is smaller in gradient direction than against it. This result has not yet been confirmed experimentally to our knowledge.

To separate runs from tumbles in bacterial trajectories, a computer algorithm called *tumble recognizer* has been used [46, 48]. It recognizes tumbles based on direction and possibly speed changes along the bacterial trajectories. When these changes are large compared to a set of threshold parameters, a tumble is detected. These parameters are chosen such that automatized tumble recognition agrees with visual inspections of the trajectories. Hence, there is no general way of how to define them.

Another way to obtain tumbling statistics is the application of *parameter inference* techniques. Therefore, parameters used in theoretical models are determined by numerical optimization procedures such that experimental data is most exactly reproduced. This makes the a priori determination of threshold parameters obsolete. Recently, Bayesian inference techniques have been applied to determine the chemotactic response function of *E.coli* [48] and to obtain statistics of frame-wise turning angles and speed changes [138].

In both cases, the desired output parameters are obtained by maximizing a likelihood function containing all trajectories, which poses a complex numerical task [139].

In this work, we propose a different approach for the inference of tumbling statistics and chemotaxis. It includes an optimization procedure with greatly reduced complexity and operates without the definition of threshold parameters. The key tools used to shrink the extensive data volume are *conditioned moments* (CMs), which resemble the Kramers-Moyal coefficients (Sec. 2.1.6). They are calculated in a minimal stochastic model of run-and-tumble motion including shot-noise, and matched to the ones obtained from experimental trajectories. Thereby, we not only infer tumbling parameters, but also the rotational diffusion constant. Finally, by analyzing appropriate fractions of the experimental CMs, we directly draw conclusions on chemotactic strategies. This provides a method to check the results obtained from parameter inference without relying on computer optimization. In Fig. 5.1 the work flow of the CM method is schematically depicted.

Kramers-Moyal coefficients have been used in experiments before to essentially distinguish a drift component from diffusion in the dynamic behavior of biological organisms or chemicals. For example, random turns of locust swarms [49], moving patterns of the amoeba *Dictyostelium* [50], or gene regulations [140] were studied with this approach. In our case, it turns out that the stochasticity in the system is clearly non-Brownian such that more than the first two Kramers-Moyal coefficients need to be considered.

Our moment method shall be applied to experimentally recorded trajectories of the bacteria *E.coli* and *P.putida* in external chemoattractant gradients. We first infer tumbling parameters neglecting the gradient direction and use them to define a novel tumble recognizer (Sec. 5.4). Next, we make use of the fact that the CMs are conditioned on a certain value of a stochastic processes. Since we infer the tumbling parameters from the CMs, those will depend on such a condition, too. This allows us to draw conclusions on chemotaxis and chemokinesis, which shall be done in three steps.

In Sec. 5.5.1, we condition on the x -coordinate in the channel, which is proportional to the chemical concentration. This reveals whether a particle is *adapted* to the applied chemical, i.e., whether its tumbling behavior depends on the background concentration of the chemical. We will give evidence that *P.putida* is not adapted to the nutrient benzoate. Next, we condition on the moving direction in the time step right before the evaluation of the CMs. As it turns out, this permits us to derive conclusions on chemotactic strategies (Sec. 5.5.2). We first confirm and quantify the classical chemotactic strategy for both bacteria, according to which they adapt their tumble rate in response to the chemical gradient. Moreover, we show that a small average angle bias in response to the gradient, which was found in [51], is, in fact, a considerable bias applied by a small subpopulation of bacteria. These findings are supported by a scaling analysis of the experimentally determined CMs. Last, in Sec. 5.5.3 the notion of Kramers-Moyal coefficients is extended further by conditioning on the entire past path of a bacterium.

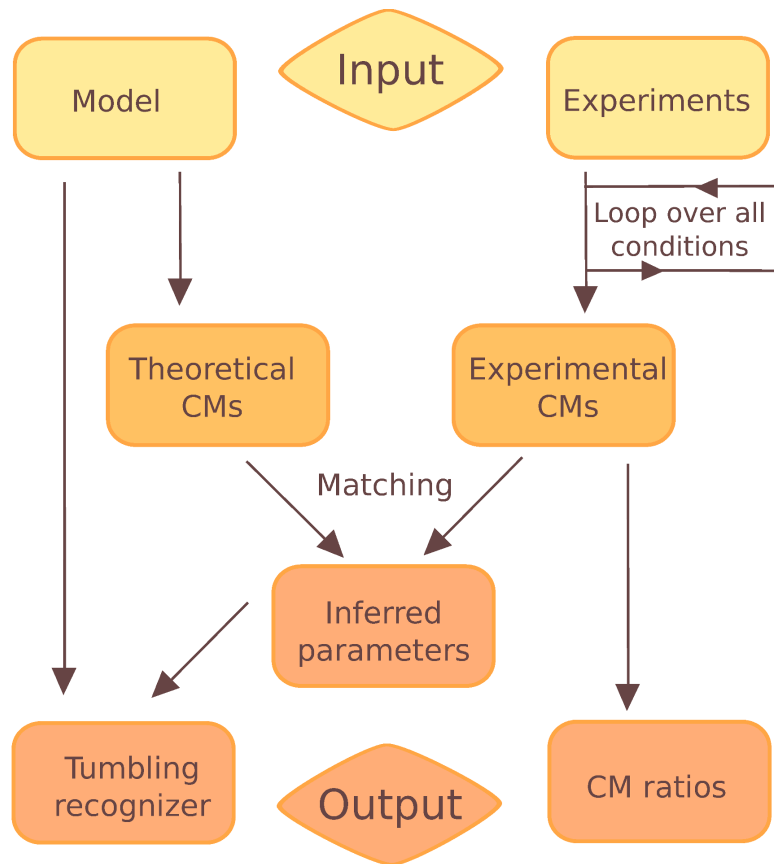


Figure 5.1.: Information flow for our tumbling inference method. As inputs we provide a minimal model for bacterial motion (Sec. 5.2) as well as experimental trajectories from a bacterium (Sec. 5.3.1). From the first we obtain a set of conditioned moments (CMs), which we analytically calculate in Sec. 5.3.2, while the experimental CMs are evaluated as detailed in Sec. 5.3.3. Indeed, these moments are functions of conditions we define in the chemotactic and chemokinesis scenarios of Sec. 5.5. In order to sample these moment functions appropriately, one needs to repeat the experimental moment calculation for sufficiently many conditions, which is indicated by the loop in the graphic. When matching analytical and experimental moments, we infer the model parameters, in particular, the tumble rate $\lambda(c)$ and the mean tumble angle $\langle |\beta| \rangle(c)$ again as functions of the condition c . Once the model parameters are inferred, the tumble angle distribution and the one of thermal angular displacements can be used for a novel tumble recognizer (see Sec. 5.4). Last, the experimental CMs can be exploited by calculating certain ratios of them, which allows to distinguish between different tumble strategies as we will show in Sec. 5.5.2.

5.2. Shot noise model for run-and-tumble motion

A typical moving pattern for bacteria such as *E.coli* is the so-called “run-and-tumble random walk” [45]. It consists of a running state and a tumble state. During the first, the bacterium moves forward on a nearly straight path, only rotational thermal noise affects its persistence. During the tumbling state the bacterium reduces its velocity and reorients rapidly in a new direction with a reorientation angle β . To account for these two systematically different types of motion, we use two stochastic processes q and ξ , which govern the orientational dynamics via the following overdamped Langevin equations:

$$\dot{\mathbf{r}}(t) = v(t)\mathbf{e}(t), \quad (5.1)$$

$$\dot{\Theta}(t) = q(t) + \xi(t), \quad (5.2)$$

where Θ is the bacterium’s orientation angle, \mathbf{r} the two-dimensional position vector, $\mathbf{e} = [\cos(\Theta), \sin(\Theta)]$ and $v(t)$ is the bacterial speed, which we discuss later. ξ is a white noise process which accounts for rotational thermal noise due to the ambient fluid. As usual, it is fully characterized by $\langle \xi(t) \rangle = 0$, $\langle \xi(s)\xi(t) \rangle = 2D_{\text{rot}}\delta(t - s)$. The tumbling events are modeled by a shot noise process [61, 141]:

$$q(t) = \sum_{i=1}^{N^\lambda} \beta_i \delta(t - t_i),$$

which is a train of N^λ delta spikes with amplitude β_i . The random variables $\beta_i \in [-\pi, \pi]$ represent the reorientation angle during a tumble event. They are symmetrically distributed about $\beta_i = 0$, i.e., rightward and leftward tumbling is equally probable. Its probability distribution P_β depends on the particular organism [45, 87]. The tumbles occur randomly at each time step with tumble rate $\lambda(t)$ resulting in a Poissonian distributed number of spikes with mean rate $\bar{\lambda} := \int_0^t \lambda(\tau) d\tau / t$ after time t (see Sec. 2.1.5). We note that our modeling of tumbles as delta spikes is an approximation that neglects the finite tumble time [46].

The tumble rate is typically modeled as a convolution of the chemotactic field experienced along the path $\mathbf{r}(t)$ and the so-called chemotactic response function R [47, 48]:

$$\lambda(t) = \lambda[\mathbf{r}(t)] := \lambda_{\text{equ}} - \int_{-\infty}^t c[\mathbf{r}(t')]R(t - t')dt'. \quad (5.3)$$

We will discuss the Response function R in more detail in Sec. 5.5.3.

Equation (5.2) can be integrated to

$$\Theta(t) = N(t) + B(t), \quad (5.4)$$

where N represents the inhomogeneous Poisson process with rate function $\lambda(t)$ for the tumble events. The rotational Brownian motion B is implemented such that for each time step Δt , the angular step is taken from a normal distribution $P(B(t+\Delta t) - B(t)) = P(dB_{\Delta t}) = \mathcal{N}(0, 2D_{\text{rot}}\Delta t)$, with mean zero and variance $2D_{\text{rot}}\Delta t$.

Finally, we define $v(t)$ to be an Ornstein-Uhlenbeck process with shot noise as in Eq. 2.34:

$$\dot{v} = r[v_0 - v(t)] - \tilde{q}(t), \quad (5.5)$$

which is controlled by the shot noise process $\tilde{q}(t) := \sum_{i=1}^{N^\lambda} v(t)U_i\delta(t - t_i)$, where the spikes correspond to the spikes of q , and each U_i is a uniformly distributed variable in the interval $[0, 1]$. This process leads to a speed track which drops down at random time points and relaxes back to its maximal value v_0 on a time scale determined by the rate r . The speed will be neglected throughout the following chapters. However, when the speed statistics from experimental trajectories are reliable, Eq. 5.5 might serve as a model for parameter inference.

5.3. Inference

In the following, we present a novel inference method for bacterial tumble behavior. We start with a short introduction of the biological experiments, from which we will extract our results.

5.3.1. Experiments

The experiments on bacteria were realized in the university of Potsdam by Marius Hintsche, Zahra Alirezaeizanjani, and Carsten Beta. In the following, I will report essential parts of the setup, which are relevant for our inference procedure. For a detailed explanation of materials and methods concerning the biology of the system, we refer to Appendix A.2. We start with experiments on the bacterium *E.coli*. After this, we report on *P.putida*.

E.coli

The setup consists of two large reservoirs connected by a quadratic channel of about 1mm length and $70\mu\text{m}$ height [see Fig. 5.2(a)]. Bacteria are filled in the reservoir on the right side of the channel at time $T = 0$ minutes. On the left side, the chemical attractant α -methyl-aspartate (short aspartate) is filled in at the same time. The trajectories of bacteria, which swim into this channel, are recorded within a quadratic viewport of about $666\mu\text{m}$ length whenever they swim in the focus plane. One obtains snippets of trajectories with a mean length of about 4 – 5 seconds. Six acquisitions were performed

in one single experiment at 7,12,30,45,60, and 95 minutes after releasing the bacteria. Due to its relatively high diffusion constant $D_c = 820\mu\text{m}^2/\text{s}$ [142], the chemical gradient builds up very quickly and does not change considerably in time [see Fig. 5.2(b)]. The bacteria in the right reservoir sense the chemoattractant, swim into the channel, and move up the gradient. Once they reach the left reservoir, the bacteria get lost, i.e., they typically never swim back into the channel. Hence, there is a constant flow of bacteria swimming from right to left through the channel.

The bacterial density profile needs considerably longer than the chemoattractant to reach a stationary state [Fig. 5.2(c)]. Just after about one hour the number of bacteria in the channel saturates and the bacterial density profile increases in gradient direction (after 95 minutes). Note that close to the observation limits the light is dimmer and therefore less bacteria are recorded. Ignoring this, we can estimate the stationary density profile of the bacteria in one dimension in the presence of a constant flux J . The latter is a sum of diffusion with diffusion constant D_{eff} and a chemotactic drift with chemotactic velocity v_c :

$$J = \rho v_c - D_{\text{eff}} \partial_x \rho, \quad (5.6)$$

where ρ represents the bacterial density. Choosing a starting profile $\rho(0) = \rho_0$, the solution can be written as:

$$\rho = \frac{J}{v_c} + \exp\left(\frac{v_c}{D_{\text{eff}}}\right) \left(\rho_0 - \frac{J}{v_c}\right). \quad (5.7)$$

In the 95 min. profile of Fig. 5.2(c) we indeed find the offset J/v_c due to the flow. However, a clear exponential increase has not yet settled on top of the offset. The non-uniform bacterium density, which slowly changes in time, will not effect our results since we use a *particle-based* method to analyze trajectories.

P.putida

The bacterium *P.putida* (Sec. 3.2.1) is released in the same setup as previously explained for *E.coli*. This time, instead of aspartate, the chemical *benzoate* is used as chemoattractant. Furthermore, three experiments were performed, where different concentrations of benzoate were filled in the left reservoir, one with high concentration (ChanH, 50mM), another with medium concentration (ChanM, 5mM), and a third one with low concentration (ChanL, 0.5mM). In any case, the recordings were taken at least one hour after filling in the bacteria.

5.3.2. Absolute conditioned Moments

The model presented in Sec. 5.2 implements a time-continuous realization of bacterial run-and-tumble motion and effectively separates two time scales, one for running and

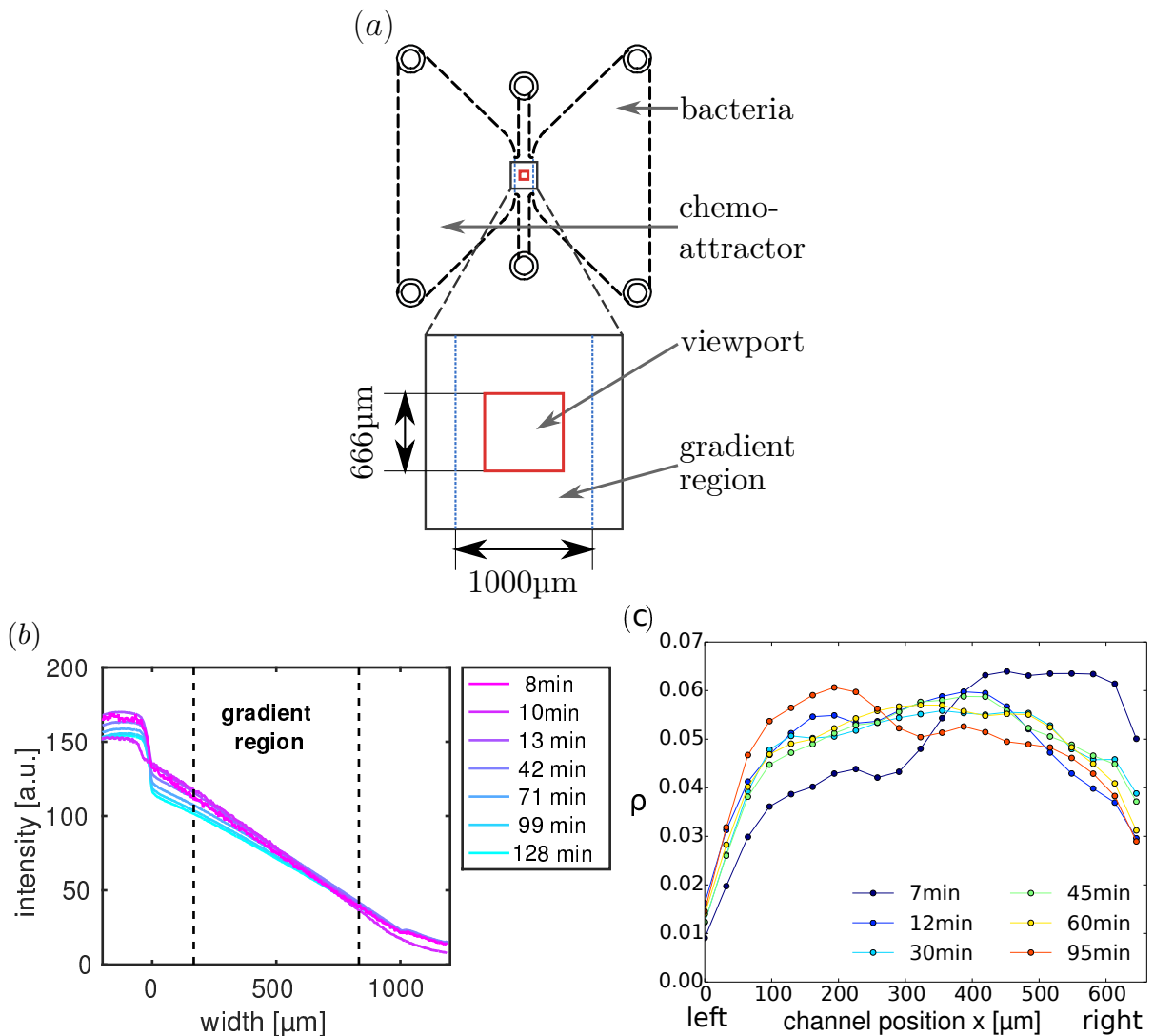


Figure 5.2.: (a) Layout of the chemotaxis assay. Attractant reservoir is on the left, cell reservoir on the right. The borders of the central gradient region is marked in blue, its height is $70\mu\text{m}$, much less than the height of the reservoir chambers. Shortly after filling a linear gradient of the attractant establishes, which points from right to left. Marked in red is the quadratic viewport imaged by the microscope. (b) Temporal evolution of the chemical gradient profile after filling the channel. Already after 8 minutes the gradient is established and changes only slightly during the time period of 2 hours. (c) Temporal evolution of the bacterial density ρ plotted against the x -position (gradient direction) of the channel. The right and left sides correspond to the borders of the observation region, marked as dashed lines in (b).

another for tumbling. We will use the model to infer the statistics of the tumbling behavior of bacteria.

As key tool of our inference, we define the n -th absolute conditioned moment (CM) of the stochastic process $\Theta(t)$ from Eq. 5.2 for a given finite Δt as

$$m_{\Delta t}^n(c)[\Theta] := \left\langle \frac{|\Theta(t + \Delta t) - \Theta(t)|_m^n}{\Delta t} \mid \mathfrak{C}(t) = \mathbf{c} \right\rangle. \quad (5.8)$$

With $|\dots|_m$ we always select the absolute value of the changing angle, which is smaller than π : $|\alpha|_m = \min(|\alpha|, 2\pi - |\alpha|)$. Furthermore, Δt is non-zero and chosen such that it is much larger than the mean tumble time. In Fig. 5.3 we show a part of a bacterial trajectory and define the relevant orientation angles.

We condition the moments on a yet to be defined process $\mathfrak{C}(t) = \mathbf{c}$ such that they become functions of \mathbf{c} . In Sections 5.5.1, 5.5.2 and 5.5.3 we will specify \mathfrak{C} , where it will depend on the biological questions we seek to answer. For example, when dealing with (spatial) chemotaxis we condition on the prior moving direction $\mathfrak{C}(t) := \Theta(t)$ as visualized in Fig. 5.3.

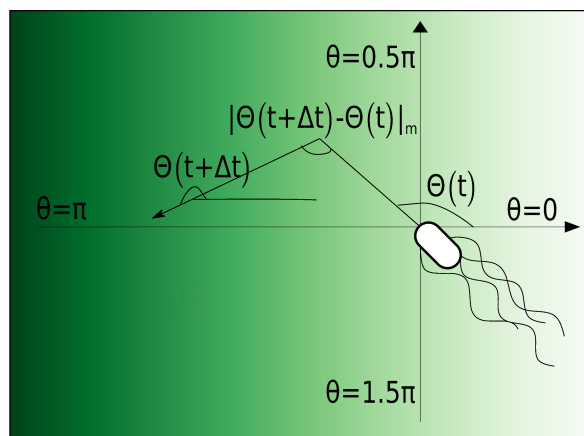


Figure 5.3.: Schematics of a bacterial tumble event: *E.coli* moves in direction $\Theta(t)$, tumbles at time $t + \Delta t$, and moves in the new direction $\Theta_{t+\Delta t}$. Thus, the turning angle becomes $|\Theta_{t+\Delta t} - \Theta_t|_m$.

The CMs are reminiscent of the Kramers-Moyal coefficients (see Sec. 2.1.6). However, they are defined with absolute values and Δt is finite. Without taking the absolute value, the odd moments vanish because both, tumbling and rotational diffusion, occur with equal probability to the left or right. Such vanishing moments, however, are of no use for our inference procedure.

Typically, with the first two moments one distinguishes between the deterministic and stochastic terms in stochastic differential equations [143]. Analyzing the Kramers-Moyal

coefficients, one can explicitly reproduce the drift $[f(x)]$ and diffusion $[g(x)^2]$ functions, which govern the dynamics of various biologic systems. However, for non-Brownian stochastic processes, moments with n larger than 1 or 2 do not necessarily vanish. This is indeed the case for our shot noise process.

The absolute value in the CM of Eq. (5.8) has to be treated with care. Therefore, we first calculate the even CMs for our angular process $\Theta(t)$ governed by Eq. (5.4):

$$m_{\Delta t}^n(\theta)[\Theta] = \left\langle \frac{|d\Theta|_m^n}{\Delta t} \mid \Theta(t) = \theta \right\rangle = \left\langle \frac{(dN + dB)^n}{\Delta t} \mid \Theta(t) = \theta \right\rangle. \quad (5.9)$$

We apply the binomial formula, use that the increments dB and dN are uncorrelated, and obtain

$$m_{\Delta t}^n(\theta)[\Theta] = \frac{\sum_{k=0}^{k=n} \binom{n}{k} \langle dB^k \rangle(\theta) \langle dN^{n-k} \rangle(\theta)}{\Delta t}. \quad (5.10)$$

Equation (5.10) shows that we need to calculate the moments of the two stochastic processes separately. The odd moments of both increments vanish:

$$\langle dB^k \rangle = \langle dN^k \rangle = 0 \quad \text{for } k \text{ odd} \quad (5.11)$$

The even moments are included in the absolute moments, which we give for later use. For dN we assume that at most one shot occurs with rate $\lambda\Delta t$ within the incremental time Δt , and obtain

$$\langle |dN|^k \rangle \approx \lambda(\theta)\Delta t \langle |\beta|^k(\theta) \rangle \quad (5.12)$$

where $\langle |\beta|^k \rangle$ is the k -th moment of the distribution P_β for the tumble angle. To calculate the moments of the Brownian process, we use the normal distribution of the increments with variance $2D_{\text{rot}}\Delta t$,

$$\langle |dB|^k \rangle = [2D_{\text{rot}}(\theta)\Delta t]^{k/2} \frac{2}{\sqrt{2\pi}} \int_0^{\pi/\sqrt{2D_{\text{rot}}\Delta t}} x^k \exp(-x^2/2) \quad (5.13)$$

For small $D_{\text{rot}}\Delta t$ we can extend the upper limit of the integral to ∞ and obtain

$$\langle |dB|^k \rangle = [2D_{\text{rot}}(\theta)\Delta t]^{k/2} (k-1)!! \begin{cases} 1 & \text{for even } k \\ \sqrt{\frac{2}{\pi}} & \text{for odd } k \end{cases}, \quad (5.14)$$

where “!!” denotes the double factorial. Note that λ , β and D_{rot} may in general be functions of θ , for brevity we do not explicitly give the argument in the upcoming formulas. We are now prepared to calculate the even CMs and start with $n = 2$:

$$m_{\Delta t}^2(\theta)[\Theta] = 2D_{\text{rot}} + \lambda\langle \beta^2 \rangle. \quad (5.15)$$

The first term on the right-hand side derives from the mean-square displacement of Brownian motion, the second one comes from the shot noise. We will specify P_β and its

moments in the following sections for each bacterium. The mixed binomial term vanishes according to Eq. (5.11). For higher even moments we only consider terms up to linear order in the small square angular displacement $D_{\text{rot}}\Delta t$. Hence, only the second moment of Brownian motion appears in a mixed term:

$$m_{\Delta t}^4(\theta)[\Theta] \approx \lambda(\langle\beta^4\rangle + 12D_{\text{rot}}\Delta t\langle\beta^2\rangle) \quad (5.16)$$

$$m_{\Delta t}^6(\theta)[\Theta] \approx \lambda(\langle\beta^6\rangle + 30D_{\text{rot}}\Delta t\langle\beta^4\rangle) \quad (5.17)$$

$$m_{\Delta t}^8(\theta)[\Theta] \approx \lambda(\langle\beta^8\rangle + 56D_{\text{rot}}\Delta t\langle\beta^6\rangle). \quad (5.18)$$

To calculate the odd CMs, the absolute value in Eq. (5.8) needs to be treated carefully. When applying Eqs. (5.11), (5.12), and (5.14), we assume the tumble angle to be larger than the Brownian angular step and refer to Appendix A.1 for more details. We obtain for the first and third moment:

$$m_{\Delta t}^1(\theta)[\Theta] = \lambda\langle|\beta|\rangle + 2(1 - \lambda\Delta t)\sqrt{\frac{D_{\text{rot}}}{\pi\Delta t}} \quad (5.19)$$

$$m_{\Delta t}^3(\theta)[\Theta] = \lambda\langle|\beta|^3\rangle + 4(1 - \lambda\Delta t)\sqrt{\frac{D_{\text{rot}}^3\Delta t}{\pi}} + 6\lambda D_{\text{rot}}\Delta t\langle|\beta|\rangle. \quad (5.20)$$

In our optimization procedure, we will only make use of the calculated moments. Note that the tumble rate λ enters linearly in each CM, while parameters related to the tumble angle β will in general be exponentiated up to the order of the moment. We will exploit this different scaling behavior of the CMs to distinguish between chemotaxis strategies concerning the tumble rate or the mean reorientation angle. The different scalings even hold, when we replace the Poisson statistics for the distribution of the tumble events, for example, by a power-law distribution of the running times [91].

5.3.3. Calculating CMs from experimental trajectories

From N experimental trajectories, we have a set of reorientation angles $d\Theta_i(t) = \Theta_i(t + \Delta t) - \Theta_i(t)$ and conditions \mathfrak{C}_i at time t , which we use to determine CMs from the experimental data according to the following formula [144]:

$$m_{\Delta t}^n(\mathbf{c}) = \frac{\sum_{i=1}^N \sum_t \frac{|\Theta_i(t+\Delta t) - \Theta_i(t)|^n}{\Delta t} K(\mathfrak{C}_i(t) - \mathbf{c}, \Delta\mathbf{c})}{\sum_{i=1}^N \sum_t K(\mathfrak{C}_i(t) - \mathbf{c}, \Delta\mathbf{c})}, \quad (5.21)$$

where we average over all orientation angles of N trajectories, with a duration longer than 3 seconds. We cut small parts of the beginning and end of each trajectory since tumbles at these locations are likely to be incomplete (more information in Appendix A.3). The Gaussian kernel $K(\mathfrak{C}_i - \mathbf{c}, \Delta\mathbf{c}) = \exp[-\frac{1}{2}(\frac{\mathfrak{C}_i - \mathbf{c}}{\Delta\mathbf{c}})^2]$ is used to condition the CMs on a defined condition value \mathbf{c} in the presence of a chemical gradient.

Now, to start with our inference, we use Eq. (5.21) to determine a set of moments $m_{\Delta t}^n(\mathbf{c})$ from the experimental trajectories. For a given \mathbf{c} value, we then numerically fit them (see Appendix A.3) with the analytical formulae for the CMs and obtain a set of parameters D_{rot} , λ and the parameters shaping P_β , all of them being, in general, functions of \mathbf{c} . The error bars in Figs. 5.7, 5.8, and 5.9 are obtained by a so-called bootstrap technique (see Appendix A.3). As mentioned earlier, to study a particular organism one only needs to adjust the reorientation distribution P_β and the time step Δt . We start with the bacterium *E. coli* (see Sec. 3.2.2 for more information on this cell).

E.coli

To complete our model of the *E. coli* bacterium, we are inspired by the seminal work of Berg and Brown [46] and specify the distribution of tumble angles β as a gamma distribution restricted to the domain $[0, \pi]$ [88] :

$$P_\beta = \gamma(\sigma, k) = \frac{1}{\sigma^k \gamma_{\text{inc}}(k, \pi)} |\beta|^{k-1} e^{|\beta|/\sigma} \quad (5.22)$$

The lower, incomplete gamma function $\gamma_{\text{inc}}(k, x) = \int_0^x t^{k-1} \exp(-t) dt$ comes in when normalizing P_β to one on the interval $[0, \pi]$. For $k > 1$ the γ -distribution has a maximum at $(k-1)\sigma$. Due to its particular scaling properties, each moment of the gamma function can be written in closed form:

$$\langle |\beta|^n \rangle = \sigma^n \gamma_{\text{inc}}(k+n, \pi/\sigma) / \gamma_{\text{inc}}(k, \pi/\sigma) \quad (5.23)$$

An example of $P_\beta = \gamma(\sigma, k)$ is shown in Fig. 5.4(a) for $\sigma = 0.64$ and $k = 2.73$. We analyze the bacterial trajectories with a time step $\Delta t = 0.5\text{s}$, however, the conclusions we will draw in the following do not sensitively depend on this number. In total, four parameters control the directional dynamics of *E. coli*: D_{rot} , λ , σ , and k . We will infer them by analyzing bacterial trajectories with the help of the CMs defined in Eq. (5.8). We analyze trajectories recorded at different times $T = 7, 12, 30, 45, 60,$ and 95 minutes after releasing the bacteria. Typically, the tracks after 7 and 12 minutes, which we call “early tracks” are analyzed together. The remaining tracks, which we call “late tracks”, are also used together.

P.putida

For *P. putida*, we choose the sampling rate smaller than in the *E. coli* case because the tumbles are typically shorter. We set $\Delta t = 0.3\text{sec}$, nevertheless, as before the exact value of Δt does not alter the results qualitatively. Furthermore, we need to specify the tumbling distribution $P_{\text{put}}(|\beta|)$. In Ref. [87] such a distribution is presented, which exhibits one strong peak at 180° and a small one at 0° corresponding to “stopping” events with no reorientation taking place. The latter ones cannot be distinguished other than by inspecting the bacterium’s speed. In this study we only consider the orientational

part of motion so that this “0-peak” cannot be detected. Due to the expected peak at 180° , we choose the following tumble distribution:

$$P_{\text{put}}(|\beta|) = (\exp[-\xi(\pi - |\beta|)] + C) / \mathcal{N}, \quad (5.24)$$

where \mathcal{N} is a normalization. The respective moments of this distribution are listed in Appendix A.6. The parameter C is a typically small offset which shows that some reorientation angles being significantly smaller than 180° are identified. For *P.putida* we only consider trajectories taken more than one hour after releasing the bacteria.

5.4. Overall tumbling statistics

First of all, we investigate the tumbling statistics irrespective of the gradient direction, in order to test our method of conditioned moments against a commonly used heuristic tumble recognizer. Thus, within this subsection we set $K = 1$ in Eq. 5.21 thereby disregarding the condition on c . We start with an investigation of the tumbling behavior of *E.coli*, then we present a novel tumble recognizer based on the inferred statistics, and finally, we study the tumble statistics of the bacterium *P.putida* at different background concentrations of the nutrient benzoate.

5.4.1. Tumbling statistics of *E.coli*

We consider the heuristic tumble recognizer as described in Refs. [48] and [87] (see also Appendix A.2). We use it to select a set of trajectories S_1 with at least one recognized tumble in all the late data sets at 30, 45, 60, and 95 min. An application of our inference method for S_1 yields a mean tumble rate $\lambda_i = 0.39 \pm 0.03 \text{ s}^{-1}$, which nicely agrees with $\lambda_c = 0.39 \pm 0.01 \text{ s}^{-1}$ determined with the heuristic tumble recognizer. Previously reported tumble rates in literature are about twice as large [46]. The reason is that our data is acquired in two dimensions such that the first and last tumble of a trajectory frequently occur at its start or end, where they enter the recording plane or leave it. We do not consider these events in our analysis because their tumble angles cannot be recorded. Leaving them out alters the overall tumble statistics significantly since most of our trajectories contain at most three tumbles.

Figure 5.4(a) compares the distribution of tumble angles determined with the tumble recognizer and the method of conditioned moments. They share common features: a maximum well below 90° , more explicitly at 50° or 63° , a skewed shape, and a considerable amount of large tumble angles. The main difference of both distributions in Fig. 5.4(a) is the absence of small tumble angles in the inferred distribution, for which we assume a gamma function. Thus, possible small tumble angles do not enter in the inferred tumble statistics, they are rather classified as Brownian noise. To include small tumble angles in the inference method, one would need an alternative ansatz function for

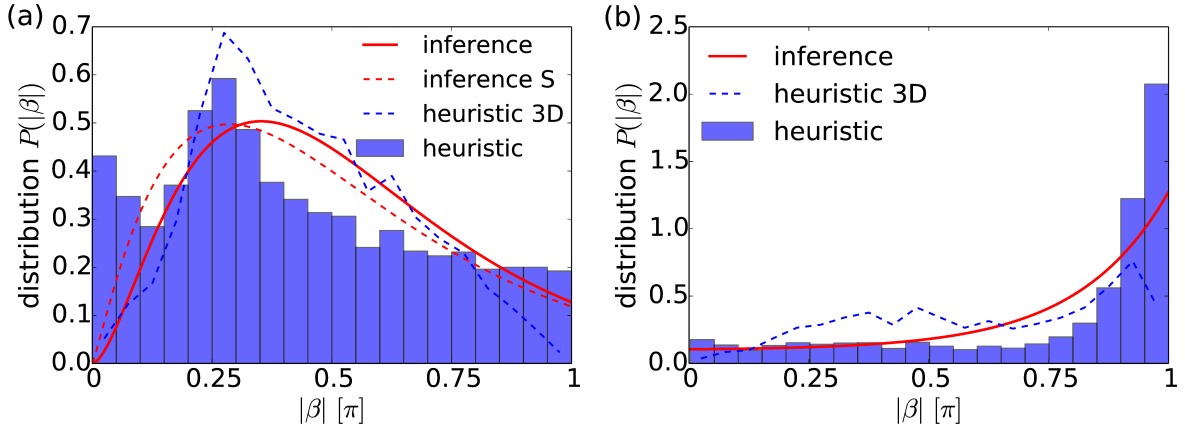


Figure 5.4.: Distribution of tumble angles, $P(|\beta|)$, determined from experiments by the heuristic tumble recognizer (bar graph) and by the inference method with the gamma function $\gamma(\sigma, k)$ as an ansatz (solid red line) for (a) *E. coli* and (b) *P. putida*. (a) All recorded trajectories at 30, 45, 60, and 95 min. with at least one tumble are used. The mean tumble angle and the standard deviation are $\langle |\beta| \rangle = 0.42\pi = 76.0^\circ$, $\Delta|\beta| = 0.27\pi = 48.7^\circ$ (heuristic tumble recognizer) and $\langle |\beta| \rangle = 0.47\pi = 85.4^\circ$, $\Delta|\beta| = 0.23\pi = 41.8^\circ$ (inference method). The inferred parameters of $\gamma(\sigma, k)$ are $\sigma = 0.64$ and $k = 2.73$. The red dashed line refers to the inferred gamma distribution ($\sigma = 0.78$ and $k = 2.15$), when the original data is smoothed. The blue dashed line refers to the histogram values multiplied by $\sin(|\beta|)$ and then normalized, thus representing the tumble angle distribution in three dimensions.

(b) *P. putida* tumble angle distribution (bar graph) by heuristic tumble recognizer and by the inference method (red line) in ChanM. The blue dashed line refers to the histogram values multiplied by $\sin(|\beta|)$ thereby representing the tumble angle distribution in three dimensions. The mean tumble angle and the standard deviation are $\langle |\beta| \rangle = 0.75\pi = 135^\circ$, $\Delta|\beta| = 0.29\pi = 52.2^\circ$ (heuristic tumble recognizer) and $\langle |\beta| \rangle = 0.72\pi = 130^\circ$, $\Delta|\beta| = 0.26\pi = 46.8^\circ$ (inference method).

the distribution P_β . Finally, unlike the heuristic and other classical tumble recognizers, we infer D_{rot} from the available data rather than using a fixed value in our analysis. We find $D_{\text{rot}} \approx 0.06 \pm 0.01 \text{ s}^{-1}$ confirming the literature value of $D_{\text{rot}} \approx 0.062 \text{ s}^{-1}$ [145].

We add two remarks. First, when we use smoothed trajectories in our inference method as the heuristic tumble recognizer does, we also obtain a maximum tumble angle of about 50° [see dashed red line in Fig. 5.4(a)]. The reason is that sharp edges in the bacterial trajectories are smoothed. However, we prefer to perform the inference method with the raw data without any additional parameters to be chosen. Second, in our two-dimensional setup, the tumble events are recorded when the three-dimensional trajectories run in a specific plane. All planes defined by the bacterial path before and after a tumble event are equivalent. So, to obtain the distribution of tumble angles for the three-dimensional trajectories, we just have to multiply $P(|\beta|)$ with $\sin |\beta|$ from the differential solid angle $d\Omega$. Indeed, the resulting distribution [see dashed blue line in Fig. 5.4(a)] compares well to the one reported in Ref. [46]. In particular, it becomes zero at $|\beta| = 0^\circ$ and 180° and it has a peak at about 50° .

5.4.2. Defining a novel tumble recognizer

Averaging over all late experimental trajectories, we have trained our model by adjusting its parameters. In particular, we know the probability distribution P_β of the tumble angle β as well as the probability density for thermal angular displacements, $\mathcal{N}(d\Theta)$, which is a normal distribution with mean 0 and variance $2D_{\text{rot}}\Delta t$. As can be seen in Fig. 5.5(a), both distributions do have considerable overlap. This raises the question, given an angular displacement $d\Theta$ from the overlap region, is it due to Brownian diffusion or due to tumbling. Hence, the task to identify a tumble event based purely on the angular displacements contains some intrinsic uncertainty. Indeed, any heuristic tumble recognizer also contains such an uncertainty, when threshold parameters have to be fixed (see Appendix A.2). Typically, a threshold value is used to define a minimal angular velocity associated with a tumble [46]. Recently, the reduced speed of the bacteria during tumbling was introduced as an additional criterion in heuristic tumble recognizers [48, 87]. It allows for the detection of tumble events with very small $d\Theta$. However, the speed statistics is noisy and one needs to introduce two additional threshold parameter, which in turn leads to further uncertainties in identifying tumble events (see Appendix A.4).

In the following, we define a novel tumble recognizer which makes the probabilistic character of tumbling recognition explicit. To this end, we invoke a standard hypothesis test framework [65]. Intuitively, if for a given reorientation angle $d\Theta$ the tumbling probability density $P_\beta(d\Theta)$ is larger than $2\mathcal{N}(d\Theta)$, we would call the event a tumble.

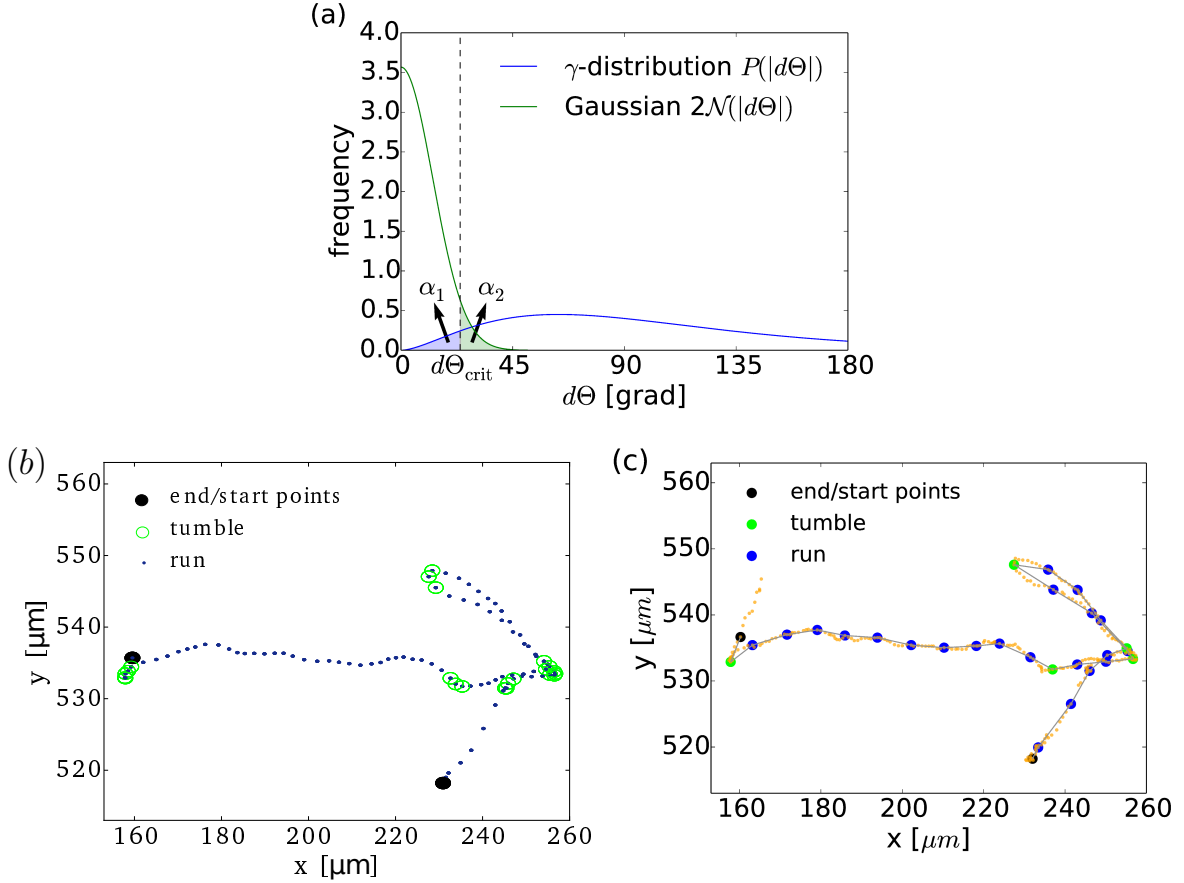


Figure 5.5.: (a) The density distributions P_β (blue, see also Fig. 5.4(a)) and \mathcal{N} (green). The blue marked area corresponds to the type I error α_1 , while the green integral refers to the type II error α_2 . The dashed line marks the threshold $d\Theta_{\text{crit}}$. (b) Smoothed sample trajectory with the tumbles marked as green circles. They are obtained by a heuristic tumble recognizer (see Appendix A.2). (c) Tumble recognition on the basis of a quotient likelihood test with the inferred distributions for $|\beta|$ and Brownian diffusion (more information in the text and in Appendix A.2). Faint red points original trajectory points, colored fat points are trajectory points with time gap $\Delta t = 0.5$. Green refers to tumble, blue to run, endpoints are not classified and therefore black.

Accordingly, we introduce the *likelihood-ratio* function:

$$R(d\Theta) := \frac{\mathcal{N}(d\Theta)}{P_\beta(d\Theta)}. \quad (5.25)$$

If R is small, we accept our hypothesis H : “ $d\Theta$ belongs to a tumble”. Otherwise, we reject it and claim that $d\Theta$ is of thermal origin. This leads to the introduction of a threshold r_{crit} such that we accept our hypothesis whenever $R < r_{\text{crit}}(\alpha_1)$. The confidence level α_1 is the so-called *type I error* and it represents the probability that we miss a tumble. It is given by the following integral [see Fig. 5.5(a)]:

$$\alpha_1 = \int_0^{d\Theta_{\text{crit}}} P_\beta(|d\Theta|) dd\Theta, \quad (5.26)$$

where $d\Theta_{\text{crit}} = R^{-1}(r_{\text{crit}})$. Indeed, by means of Eq. (5.26) we implicitly extract the threshold value r_{crit} . In our case, we choose $\alpha_1 = 0.05$. Once given α_1 and, with it, the threshold value $d\Theta_{\text{crit}}$, we can calculate the *type II error* α_2 which is the probability that by mistake we recognize a tumble. It is given by: $\alpha_2 = \int_{d\Theta_{\text{crit}}}^{\pi} \mathcal{N}(d\Theta) dd\Theta \approx 0.06$. This hypothesis test based on the likelihood-quotient R is also called Neyman-Pearson test [146]. It has the following optimality property: Given the 2 distributions and the confidence level α_1 , there is no other test with smaller type II error. We apply this test to a representative trajectory plotted in Fig. 5.5(c) and compare it to the track divided in tumbles and runs by our heuristic tumble recognizer [Fig. 5.5(b)]. We see that most of the recognized tumbles are identical. Only one tumble is identified by the heuristic tumble recognizer, which is marked as run with our method. The heuristic tumble recognizer detects a (faint) speed minimum at this spot, whereas the angular change is insufficient for the inference recognizer to tag the event as tumble. We checked that our tumble recognizer identifies 85 % of tumbles and runs detected by the heuristic recognizer.

Hence, with our proposed tumble recognizer the uncertainty in tumble recognition is quantified by the type I and II errors. There are no unknown parameters, which have to be set a priori. To increase the accuracy further, one might consider speed fluctuations in addition to the angle statistics.

5.4.3. Tumbling statistics of *P.putida*

In Sec. 3.2.2 we discussed the concept of adaptedness which means that the tumble rate of the respective bacterium is not sensitive to the concentration of a certain chemical. In our experiments, *E.coli* swims in an aspartate suspension, a chemoattractant for which *E.coli* has been proven to be adapted [48]. For the chemo-attractant *benzoate*, Ref. [90] provided evidence that *P.putida* is imperfectly adapted.

In the following, we present the overall tumble statistics of the bacterium *P.putida* as derived by our inference technique for three different background concentrations (see

Sec. 5.3.1) in ChanH (high), ChanM (medium), and ChanL (low). As for *E.coli* we do not condition on any process $\mathfrak{C}(t)$, i.e., set $\Delta c \rightarrow \infty$. First of all, for *P.putida* we always find a nearly constant mean reorientation angle $\langle |\beta| \rangle \approx 2.35 \pm 0.05$ independent of the background concentration (and, as we shall see in Sec. 5.5.2, independent of prior orientation). The tumble angle distribution is plotted in Fig. 5.4(b), red line. It compares well to the distribution obtained by the heuristic tumble recognizer, in particular, the peak at $\beta = \pi$ is clearly recovered and the mean tumble angles of both distributions nicely agree [see caption of Fig. 5.4(b)]. Furthermore, when plotting the normalized distribution $\propto \sin(|\beta|)P(|\beta|)$ to capture the three-dimensional tumble angle distribution (dashed blue line), one recovers a bimodal shape as reported in Ref. [147].

In contrast to the mean tumble angle, the tumble rate λ clearly depends on the channel under investigation. We obtain $\lambda_{\text{ChanL}} = 0.97 \pm 0.06 \text{ sec}^{-1}$, $\lambda_{\text{ChanM}} = 1.1 \pm 0.04 \text{ sec}^{-1}$ and $\lambda_{\text{ChanH}} = 0.61 \pm 0.02 \text{ sec}^{-1}$. Note that in any case the tumble rate is significantly larger than for *E.coli*. This is because *P.putida* typically turns with a turning angle close to π such that it does not leave the focus plane. The varying tumble rates might have two different explanations due to the particular experimental setups. At the beginning of each experiment, different concentrations of benzoate are injected on the left side of each channel. This leads, in stationary state, to both, different gradient strengths $|\nabla c|$ and different background concentrations $c(x)$ in the channels. Both could be the reason for varying tumble rates λ . We note that irrespective of the explanation, this situation is in contrast to the case of *E.coli* responding to aspartate, where the equilibrium tumble rate λ_{equ} is always a constant. In Sec. 5.5.1, we continue this investigation and give evidence for non-adaptedness of *P.putida* to the nutrient benzoate.

5.5. Chemotaxis and Chemokinesis

In Sec. 3.2.2 we have defined chemotaxis as the directed motion along chemical gradients. For cells chemotaxis is pivotal, it guides them to higher concentrations of nutrients *and* makes them stay there. In contrast, chemokinesis, which refers to tumbling behavior based on the present background concentration at every time, leads to disadvantageous stationary states as we have shown in Sec. 3.2.4. Chemokinesis is equivalent to the non-adaptedness of a bacterium, since in both cases its random walk depends on the background concentration.

Furthermore, chemotaxis can only be realized when the chemical gradient is successfully recognized. As detailed in Sec. 3.2.2, bacteria base their decision on the chemical concentration experienced along their past trajectory, which is termed *temporal chemotaxis*. For *spatial chemotaxis*, which is observed for larger organism such as the amoeba *Dictyostelium discoideum*, the chemical gradient is recognized instantaneously based on the nutrient concentration difference along the cell body [148].

Now, no matter if we want to study chemokinesis (i.e., adaptedness), spatial, or even

temporal chemotaxis, each scenario can be treated by our conditioned moment approach. As we will show in the following chapters, we just need to specify the condition process $\mathfrak{C}(t)$ in Eq. (5.8) appropriately.

5.5.1. Adaptedness to the background concentration

In this section, we investigate the adaption for *E.coli* and *P.putida* to their respective nutrients aspartate and benzoate. This can be realized by conditioning the conditioned moments on the x -position in the channel because the chemical gradient extends along it. Hence, we choose $\mathfrak{C}(t) := X(t)$ such that Eq. (5.8) turns into:

$$m_{\Delta t}^n(x) = \left\langle \frac{|\Theta(t + \Delta t) - \Theta(t)|_m^n}{\Delta t} \middle| X(t) = x \right\rangle. \quad (5.27)$$

To extract the moments from experimental trajectories, we apply the formula (5.21) and choose $\Delta \mathbf{c} = \Delta x = 64.5 \mu\text{m}$. We investigate the x -dependence of the tumble rate λ and the mean reorientation angle $\langle |\beta| \rangle$ for the bacteria *E.coli* and *P.putida*. We fit a linear function to the data points to detect trends easier. For *E.coli* we average over all available trajectories (at 7,12,30,45,60, and 95 min) in order to obtain highly reliable results. As it turns out, there is no significant dependency neither in λ nor in $\langle |\beta| \rangle$ on the x -position, i.e., on the background concentration of c [Fig. 5.6(a)]. This result is expected since *E.coli* has been reported to be adapted to the chemical aspartate.

For *P.putida*, the situation is different. We have seen that this bacterium, when exposed to different background concentrations, swims with different tumble rates. However, as we have pointed out, in the three investigated channels not only the background concentration varies but also the gradient strength. We concluded that, a priori, both might be responsible for the different response.

In order to study the dependency $\lambda(c)$, we analyze each channel separately and condition as specified in Eq. 5.27. As in the *E.coli* experiments, in each channel the gradient strength can approximately be assumed as constant [Fig. 5.2(b)]. It turns out that for high overall background concentration of the attractant (ChanH), we observe a clearly increasing tumble rate when approaching the right side of the channel with lower concentration of c [Fig. 5.6(b)]. On the right, the tumble rate λ is about 15% lower than on the left side. In ChanM, i.e., with lower overall benzoate concentration, the relative difference is smaller, about 8%, but still recognizable [Fig. 5.6(c)]. As usual for *P.putida*, the mean reorientation angle is essentially constant. Thus, together with the results from Sec. 5.4.3 we confirm that *P.putida* is not adapted to the attractant benzoate.

One might think that the non-adaptedness to benzoate is of advantage for *P.putida*: It tumbles more often in regions of low concentration in order to leave them faster. P.-G. De Gennes showed in Ref. [92] that such a strategy indeed leads to a drift towards *higher* concentration regions. However, in section 3.2.4 we have shown that, in stationary state, the cell would end up with higher probability in regions with *low* nutrient concentration.

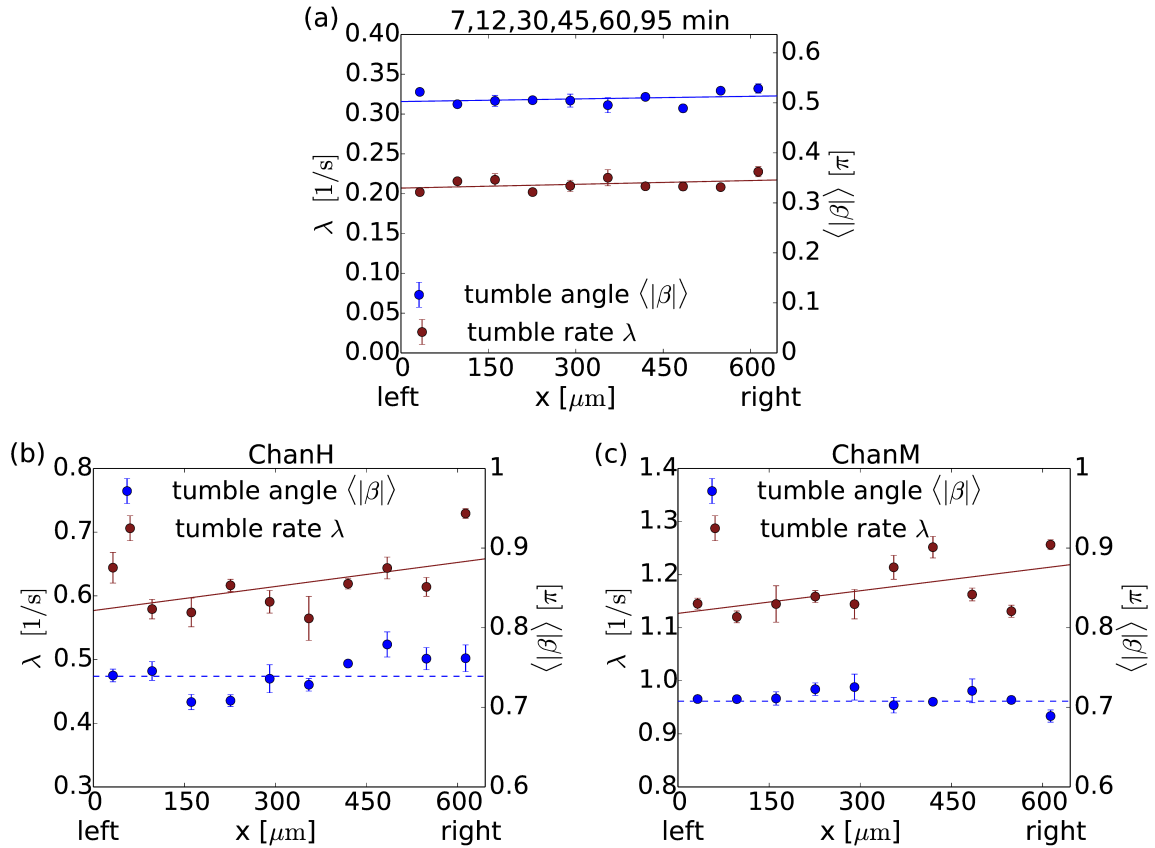


Figure 5.6.: Mean tumble rate λ (red) and mean tumbling reorientation angle $\langle|\beta|\rangle(\theta)$ (blue) against x -position in the channel. The chemical gradient is directed along the negative x -axis, with large concentration on the left and low concentration on the right. All curves are fitted by linear functions to illustrate trends. (a) Averaged over all trajectories of the experiment with *E. coli*. There is no significant dependence on x for neither of the curves. This confirms that *E. coli* is adapted to aspartate. (b),(c) *P. putida* in channel with high (b) and medium (c) nutrient concentration. We see that the tumble rates decrease towards higher background concentration, which indicates that *P. putida* is not adapted to benzoate.

5.5.2. Chemotactic strategies

In this section, we infer the specifics of the tumbling behavior of *E.coli* and *P.putida* when performing (spatial) chemotaxis. Therefore, we condition on the orientation angle θ by setting $\mathfrak{C}(t) := \Theta(t)$ in Eq. (5.8) and set $\Delta\mathbf{c} = \Delta\theta = 0.125\pi$ in Eq. (5.21). However, due to Eq. (5.3) we expect the tumble rate $\lambda(t)$ at time t to depend on the whole past of the trajectory. So, why is conditioning on the orientation angle θ sufficient? The response function R is typically peaked at times close to zero meaning that the response to the very recent past is weighted strongest [47]. Since the bacterium moves persistently between two tumbles, we expect a strong dependence on the orientation θ just before tumbling. We will make this insight more quantitative in Eq. (5.28).

5.5.2.1. Classical chemotaxis and angle bias for *E.coli*

To determine the conditioned moments, we consider all trajectories which are longer than three seconds irrespective of whether they contain tumble events or not. This, of course, leads to a lower tumble rate than for the trajectory set S_1 analyzed above. In the left column of Fig. 5.7 we plot the inferred tumble rate $\lambda(\theta)$ (red curve) and the mean tumble angle $\langle|\beta|\rangle(\theta)$ at different times T after releasing the bacteria. To determine $\langle|\beta|\rangle(\theta)$, we use the inferred parameters $k(\theta)$ and $\sigma(\theta)$ in Eq. (5.23).

Tumble rate

We find that at early and late times T , $\lambda(\theta)$ is essentially symmetric about its minimum $\theta = \pi$, where the bacterium moves along the chemical gradient (see Fig. 5.3). Indeed, the data is well fitted by a shifted cosine function, $\lambda_{\text{fit}}(\theta) = a_1 + a_2 \cos(\theta)$, with two fit parameters a_1 and a_2 . This can be rationalized by means of Eq. (5.3). Since the chemical gradient is directed along the negative x -direction, we can approximate the integral in Eq. (5.3) by the following sum representing the runs of the bacterium between two tumbles:

$$\lambda(t) = \lambda_{\text{equ}} + \cos(\theta)Kv_0 \int_{t_0}^t R(t-t')tdt' + \sum_{i=0}^n \int_{t_{i+1}}^{t_i} \dots \quad (5.28)$$

Here, K is the magnitude of the constant chemical gradient. In the right-hand side of Eq. (5.28) we neglect the sum of the third term resulting from runs before the last tumble. We assume that this sum vanishes when averaging over many trajectories. Hence, comparing our fit function with Eq. (5.28), we recognize that a_1 approximates the mean tumble rate λ_{equ} and $a_2 \propto Kv_0$ is a measure for the strength of the chemotactic response. The plots in Figs. 5.7(a) and (c) reveal that for the late and early trajectories λ_{equ} and chemotactic strength are very similar: $a_1 = 0.28$ and $a_2 = 0.11$ for the early trajectories, and $a_1 = 0.24$ and $a_2 = 0.10$ for the late tracks. Therefore, our method reproduces the classical chemotaxis strategy, *i.e.*, adaption of λ to the gradient and quantifies it.

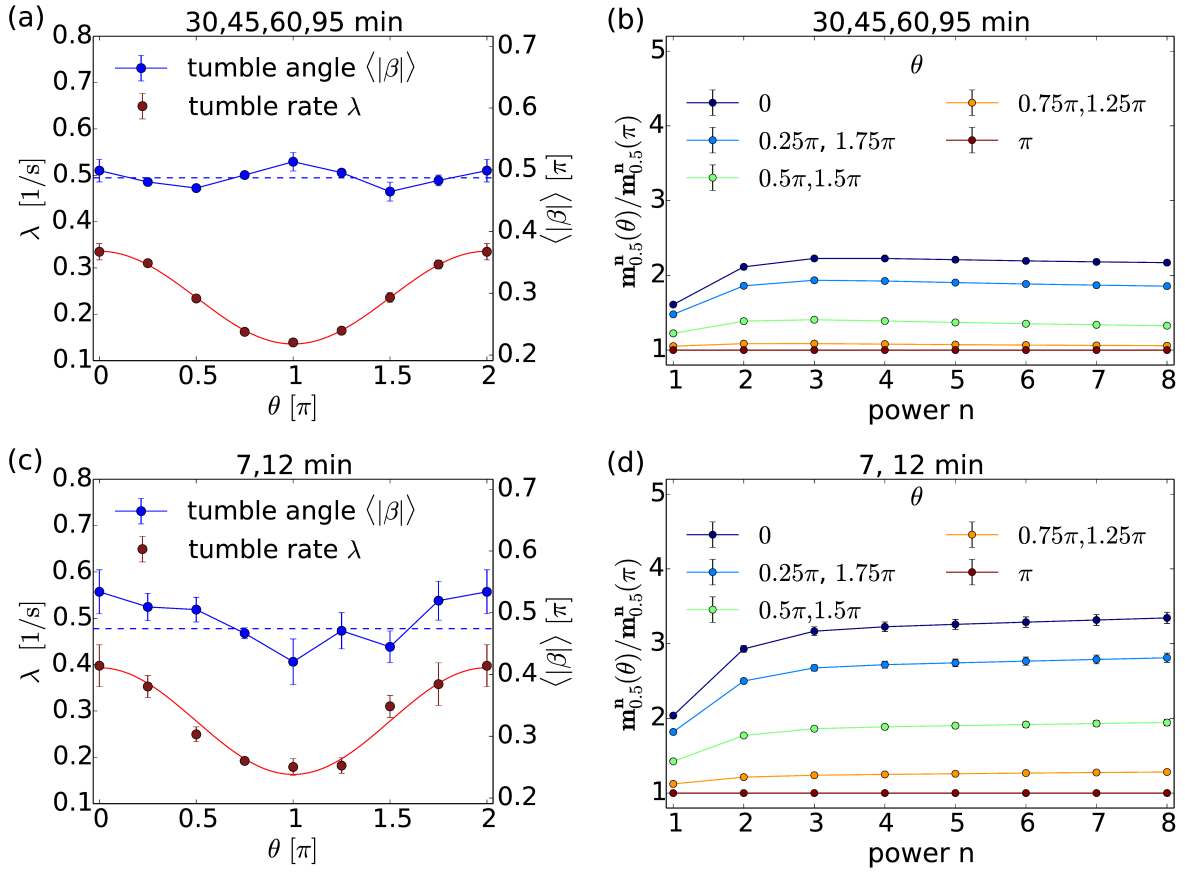


Figure 5.7.: (a) The mean tumble rate λ (red) and the mean reorientation angle $\langle |\beta| \rangle$ (blue) in function of the prior orientation of the bacterium θ . It is calculated averaging over trajectories of the late tracks at $T=30,45,60$, and 95min . The tumble rate is fitted by a cosine function, more details in the main text. (b) $m_{\Delta t}^n(\theta)/m_{\Delta t}^n(\pi)$, i.e., the conditioned moments depending on their direction θ (legend) divided by the conditioned moment with the argument π . These moment fractions are essentially constant so that no angle bias can be expected. Indeed, (a) shows that there is none (blue curve). However, the curves assume different heights which points clearly towards a strong dependence of the tumble rate on θ which is verified in the red curve of (a). (c),(d): Same analysis evaluated with tracks after 7 and 12 minutes. In contrast to the previous later states here we individuate a weak angle bias [blue line in (c)] and accordingly slightly increasing moment fractions in (d).

Mean tumble angle

Surprisingly, early and late trajectories behave differently for the mean tumble angle $\langle |\beta| \rangle(\theta)$. While in the late trajectories it is roughly constant in θ [blue curve in Fig. 5.7(a)], a minimum around $\theta = \pi$ is recognizable in the early tracks [Fig. 5.7(c)]. This indicates that at early times of the experiment tumble angles are biased towards smaller values when *E.coli* moves along the chemical gradient. In Ref. [51] the authors report that the mean direction of the runs is slightly biased in gradient direction. This result is explained with an angle bias, which is so small (about $3^\circ \approx 0.05\pi$) that it could not be observed in previous experiments as pointed out in Ref. [149].

To support our findings, we plot ratios of the CMs of the form $m_{\Delta t}^n(\theta)/m_{\Delta t}^n(\pi)$ versus order n in Figs. 5.7(b) and (d). From Eqs. (5.15)-(5.20) we find that for $n > 3$ the moments are mainly determined by the leading term $\lambda \langle |\beta|^n \rangle$ since $D_{\text{rot}}\Delta t \ll 1$ and thus

$$\frac{m_{\Delta t}^n(\theta)}{m_{\Delta t}^n(\pi)} \approx \frac{\lambda(\theta) \langle |\beta|^n(\theta) \rangle}{\lambda(\pi) \langle |\beta|^n(\pi) \rangle}. \quad (5.29)$$

Since the tumble rate $\lambda(\theta)$ is smallest along the chemical gradient ($\theta = \pi$), we expect this ratio of CMs to increase with growing $|\theta - \pi|$ for each n . This is confirmed by the graphs in in Figs. 5.7(b) and (d) for a fixed n . More importantly, the ratio provides a mean to clearly distinguish between classical chemotaxis and a strategy with angle bias: If the ratio in Eq. (5.29) increases with growing n , we must have $\langle |\beta|(\pi) \rangle < \langle |\beta|(\theta) \rangle$ for $\theta \neq \pi$ and hence an angle bias. In contrast, if the ratios for different θ converge towards constant values at larger n , we confirm classical chemotaxis with $\langle |\beta|(\pi) \rangle = \langle |\beta|(\theta) \rangle$. Therefore, inspecting the ratio of CMs provides a method to distinguish chemotactic strategies without any fitting procedure involved. For the late trajectories we find the expected convergence towards nearly constant values at roughly $\lambda(\theta)/\lambda(\pi)$ [see Fig. 5.7(b)]. However, for the early trajectories the ratios in Fig. 5.7(d) show a small but clearly recognizable increase with n , which hints to an angle bias. This result motivated a more careful analysis of the early trajectories at $T = 7$ and 12 min..

What distinguishes the early acquisitions from the later ones? At early stages of the experiments the population is sub-classified in chemotactically efficient and less efficient swimmers along the x -direction of the channel. This can be seen as follows: In a further analysis presented below, we will divide the viewport of our experimental setting in Fig. 5.2 in a right, middle, and left part of the same width of $222\mu\text{m}$ and condition the CMs also on the location in either of these parts. A bacterium moves with a chemotactic drift velocity along the gradient. For the chemical gradient employed in our experiments a typical value for *E.coli* is $0.9\mu\text{m/s}$ [46]. Now, to reach all locations in the left part of the viewport, an average bacterium needs ca. $800\mu\text{m}/0.9\mu\text{m/s} \approx 900\text{s}$ or ca. 15min.. Given the additional fact that at the initiation of the experiment, the chemotactic gradient has not been established yet, we conclude that only chemotactically fast bacteria can reach the left part of the viewport and be recorded 7 or 12 minutes after the start of the experiment. At later times also chemotactically slower bacteria reach the left part and

the bacterial population is well mixed. Now, how can we explain the efficient swimming of the bacteria in the left part? Either, they have special abilities, for example, they swim faster or they might be able to apply an angle bias. Or they are the outcome of statistical fluctuations, *e.g.*, their tumble angles β *incidentally* turned out to be preferential. In this case, when analyzing efficient swimmers locally in the left part of the channel, there is no reason to find any bias again, since the successful swimming before occurred only by chance.

Notwithstanding, we find strong indications for an angle bias, when restricting our analysis to the left third of the channel (Fig. 5.8). The CM-ratios increase remarkably [Fig. 5.8(b)], whereas for the other sub-populations the curves are essentially constant or they even fall [Figs 5.8(d),(f)]. Accordingly, we find an angle bias in gradient direction for the left part in Fig. 5.8(a) but no clear trend in the middle and right parts [Figs 5.8(c)(e)]. In conclusion, we give evidence for a subpopulation of *E.coli* bacteria which applies an angle bias to climb chemical gradients more effectively.

The tumble rate, on the other hand, is more sensitive to the gradient for bacteria on the right than on the left side of the channel [red curves of Figs 5.8(a)(c)(e)]. This effect is also observed for all later stages of the experiment (see Appendix A.5), so in contrast to the angle bias it is not particular for early data acquisitions. We provide an explanation for a deeper minimum in the tumble rate when focusing on the right side of the channel. At the right side of the channel there are some bacteria which swim in nearly straight lines from the right to the left. These bacteria might have defects in their *cheX*, *cheB*, *cheY*, and *cheZ* genes [150]. When they enter the channel (by chance), they will keep swimming for some time in the correct direction. They are overrepresented because without tumbles they are likely to stay in the focus plane. They of course drastically reduce the mean tumble rate in gradient direction. Due to rotational diffusion they loose track after about 15 seconds, this is typically before they arrive in the middle part of the channel. This reasoning explains why after 60 minutes the total effect becomes somewhat weaker: On the one hand, the amount of non-tumbling swimmers in the channel stays the same. On the other hand, the number of bacteria in the channel is larger because it is permanently increasing in time. Hence, the total effect is weaker.

5.5.2.2. Concentration dependent chemotaxis of *P.putida*

In this section, we discuss the chemotactic strategy of the bacterium *P.putida* using our moment method again. For *P.putida* we analyze two experiments, one with high initial nutrient concentration in the left reservoir (we called this setup ChanH) and one with medium initial nutrient concentration (ChanM) (see Sec. 5.3.1). As for *E.coli*, we plot the tumble rate and mean tumble angle (see Fig. 5.9) for both channels.

We first note that the mean tumble angle $\langle |\beta| \rangle = 0.72\pi \pm 0.03\pi$ is approximately constant [see Fig. 5.9(a),(b)]. This is also confirmed by the ratios of CMs, which clearly converge to constant values (see Fig. A.5).

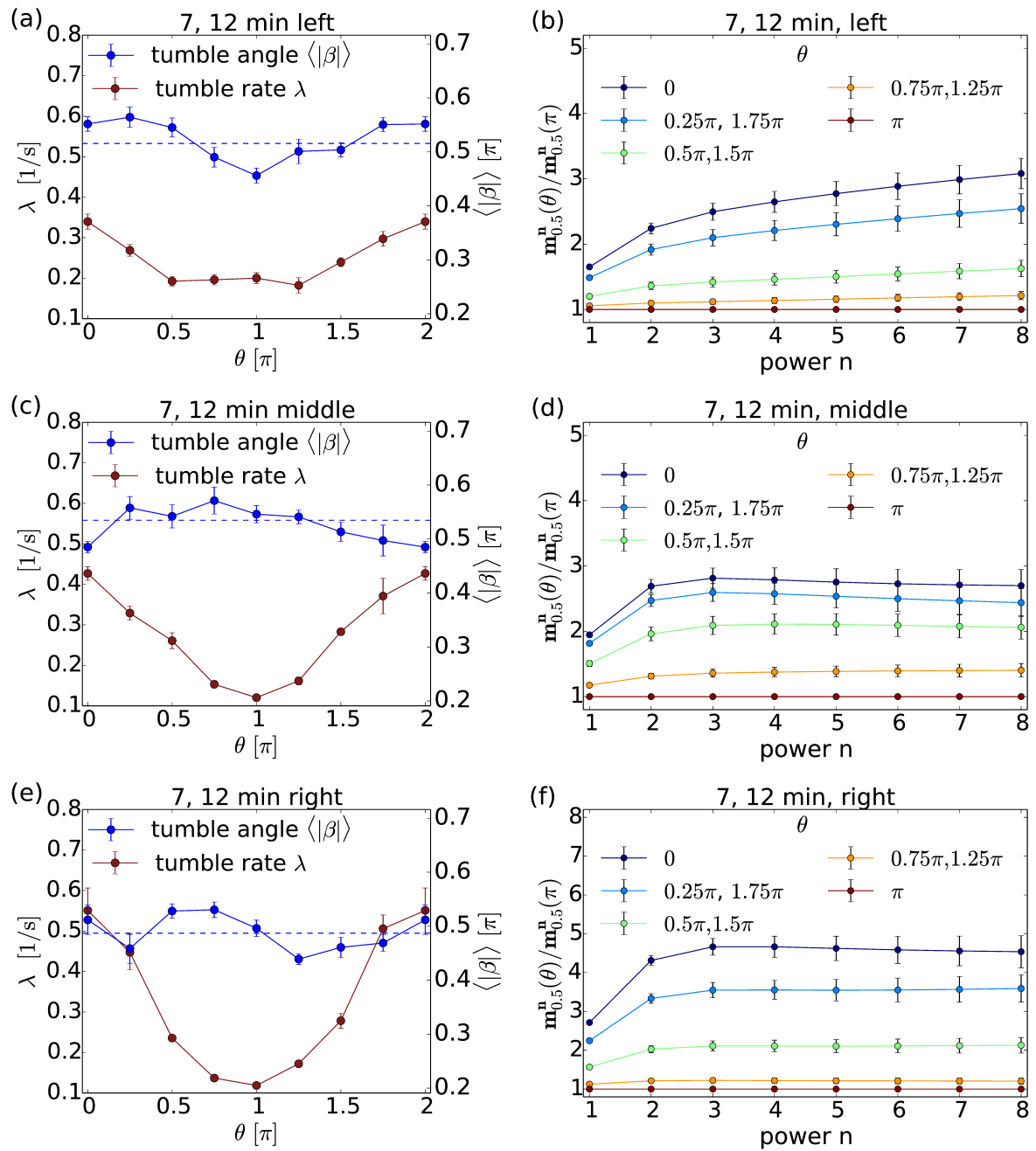


Figure 5.8.: Early bacterial tracks analyzed separately in different parts of the channel. Left column: The mean tumble rate λ (red) and the mean tumble angle $\langle|\beta|\rangle$ (blue) plotted versus the orientation angle θ prior to tumbling for (a) the left, (c) the middle, and (e) the right part. The blue dashed line marks $\langle|\beta|\rangle(\theta)$ averaged over all directions. Right column: Ratios of CMs, $m_{\Delta t}^n(\theta)/m_{\Delta t}^n(\pi)$, plotted versus power n for different orientation angles θ for (b) the left, (d) the middle, and (f) the right part.

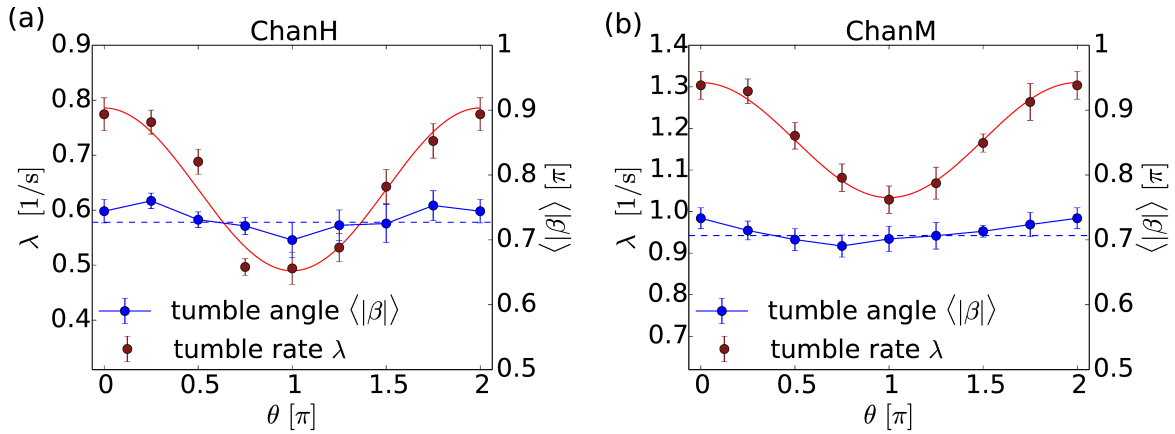


Figure 5.9.: The mean tumble rate λ (red) and the mean reorientation angle $\langle|\beta|\rangle$ (blue) in function of θ for the bacterium *P.putida*. The tumble rate assumes a minimum in gradient direction whereas the mean reorientation angle is approximately constant. We fit the curves with a cosine function, more details in the main text. (a) High background concentration and gradient strength. (b) Medium background concentration and gradient strength.

However, as *E.coli*, *P.putida* biases its tumble rate, i.e., it applies a classical chemotaxis strategy [Fig. 5.9(a),(b)]. The tumble rate is again well approximated by a shifted cosine $\lambda_{\text{fit}}(\theta) = a_1 + a_2 \cos(\theta)$. In ChanM we obtain $a_1 = 1.17$ and $a_2 = 0.14$ while in ChanH the fitting gives $a_1 = 0.64$ and $a_2 = 0.15$. Hence, the equilibrium tumble rate of *P.putida* differs nearly by a factor of 2, which we have discussed already in Sec. 5.4.3. The chemotactic response strength a_2 is comparable for the two cases. This implies that the ratio a_2/a_1 is about twice as large in ChanH compared to ChanM meaning that the relative chemotactic response is more pronounced in the strong gradient situation.

5.5.3. Temporal chemotaxis: Testing the response function

In the previous section, we have conditioned on the bacteria's moving direction with respect to the gradient right before a reorientation event. Thereby, we identified the chemotactic strategies applied by the bacteria *E.coli* and *P.putida*. With Eq. (5.28) we established a connection between the chemotactic response to the current moving direction of a bacterium, θ , and the response to its past trajectory. Typically, the first is called *spatial*, the second *temporal* chemotaxis. We have seen that conditioning on θ was sufficient to detect bacterial chemotaxis, although its actual origin is temporal. However, by neglecting the past, we also left the response function aside. In this section, we measure temporal chemotaxis directly while testing various response functions.

As before, we need to specify the condition in the CMs correctly. This time, the

information right before the reorientation is not sufficient. In the case of *E.coli*, the past concentration history affects the tumble rate as dictated by Eq. (5.3). Hence, we define a temporal chemotactic condition process:

$$\mathfrak{C}(t) := C_T(t) = \int_{-\infty}^t c[\mathbf{r}(t')]R(t-t')dt'. \quad (5.30)$$

We denote the associated condition $\mathfrak{c} = c_T$ in Eq. (5.8). As detailed in Sec. 5.5.3, the response function was experimentally measured. However, its parametrization in a particular functional shape is not straight forward. In Ref. [151], the following exponential form was chosen:

$$\tilde{R}_\alpha(t) := \alpha^2 \exp(-\alpha t)(c_1 t - 0.5c_2 \alpha t^2). \quad (5.31)$$

The function exhibits a maximum close to $t = 0$, becomes negative for larger t , and relaxes back to zero on the time scale $t \sim \alpha^{-1}$ [see Fig. 5.10(a)]. For $c_1 = c_2$ the integral of \tilde{R}_α is zero. Hence, it captures essential features of the experimentally measured response function (Sec. 3.2.2). The response function (5.31) with $\alpha = 1.5$ resembles it best.

Nevertheless, this particular form might be problematic when used for comparison of different response functions, in particular, for varying α . To see this, consider the chemotactic response, i.e., the variation in the tumble rate, generated by a straight walk up the gradient with constant velocity so that $c_s[\mathbf{r}(t)] = v_0 K t$ with constant gradient strength $K = |\nabla c|$. For such a typical trajectory, the response should be independent of α . However, substituting c_s in Eq. (5.30) and using the definition (5.33) one obtains after an explicit integration:

$$\int_{-\infty}^t c_s(t')\tilde{R}_\alpha(t-t')dt' = \alpha^{-1}v_0 K(3c_2 - 2c_1) \quad (5.32)$$

Hence, a response function \tilde{R} with large relaxation time α^{-1} creates a stronger chemotactic response *by definition*. In order to avoid such a self-induced bias, we define:

$$R(t) = R_\alpha(t) := \alpha \tilde{R}_\alpha(t) = \alpha^3 \exp(-\alpha t)(c_1 t - 0.5c_2 \alpha t^2). \quad (5.33)$$

We choose equal constants $c_1 = c_2 = 0.02$ such that the response function is adapted. By varying the only free parameter α , we can test the effect of different response functions on the CMs by virtue of Eqs. (5.8) as well as (5.30) and, subsequently, their effect on the tumbling parameters.

In this section, we concentrate on the behavior of the tumble rate $\lambda = \lambda(c_T)$. First of all, we note that when the function $\lambda(c_T)$ is axially symmetric, there is no chemotactic response. This is because in such a case, the bacteria respond the same way to upward and downward gradient swimming. Hence, we choose the degree of asymmetry of $\lambda(c_T)$ as a measure for the strength of the chemotactic response

$$\eta := \frac{1}{2C} \left[\int_{-L}^0 \lambda(c_T) dc_T - \int_0^L \lambda(c_T) dc_T \right], \quad (5.34)$$

with $L = 1$ for *P.putida* and $L = 1.2$ for *E.coli*. η indeed vanishes for symmetric $\lambda(c_T)$ and is large for strong chemotactic response. Using this measure, we can compare different response functions R_α , thereby searching for maximal chemotactic response.

From a biological point of view, this corresponds to the search for an “optimal” response function because maximal chemotactic response leads to optimal chemotactic performance (see Sec. 3.2.4). This is in contrast to the Bayesian method of Ref. [48], which we introduced in Sec. 3.2.3. There, one searches for the response function which exists *most likely*, i.e., with highest probability, given the experimental observations.

Results

We start with the bacterium *E.coli*. For the inference we use all available trajectories together (7, 12, 30, 45, 60, and 95 min.). We would expect the tumble rate λ to linearly fall as a function of c_T [Eq. (5.3)]. In fact, as can be seen in Fig. 5.10(b), the tumble rate $\lambda(c_T)$ for different values of α exhibits a decrease starting from $c_T \approx -0.2$. For more negative c_T , there is no clear trend recognizable. The reason for large tumble rates around $c_T = 0$, especially for response functions with large α , are very long tumble times of some bacteria. During a long tumble, c_T is small due to many reorientations, where at the same time, the bacterium reorients very often.

Leaving this issue aside, inspecting the different curves in Fig. 5.10(b), we see a similar response for all α . However, choosing the experimentally measured response function with $\alpha = 1.5$, the chemotactic response η indeed turns out to be maximal (Fig. 5.10(e), blue curve).

For *P.putida*, to our knowledge, nothing is known about the temporal chemotactic response. Only from Sec. 5.5.2 we know that it performs more pronounced chemotaxis in ChanH than in ChanM. As can be seen in Fig. 5.10(c), in ChanH we obtain an approximately linear decrease in all cases, apparently in line with Eq. (5.3) valid for *E.coli*. The response η is maximal for $\alpha = 2.5$ and decreases with decreasing relaxation time α^{-1} of the response function [Fig. 5.10(e), red curve]. The situation for medium gradient strength in ChanM is different. First of all, the response is, for all curves in Fig. 5.10(d), much weaker than in ChanH. This was expected based on the results in Sec. 5.5.2.2. Furthermore, comparing the curves, we see great similarities. Only the curve corresponding to the *E.coli* response function ($\alpha = 1.5$) exhibits significantly smaller chemotactic response η than the others [Fig. 5.10(e), green curve].

Summing up, for *E.coli* we have weak evidence that the measured response function ($\alpha = 1.5$) indeed is the optimal one because the chemotactic response appears to be maximal. In Ref. [151] a similar optimal response function is derived, however, they made use of a different parametrization of the response function (see discussion above). For the bacterium *P.putida*, we confirm the result of the previous section that the chemotactic response is stronger in ChanH than in ChanM. More importantly, we provide evidence that the optimal response function of *P.putida* is R_α with $\alpha \approx 2.5$. This corresponds to

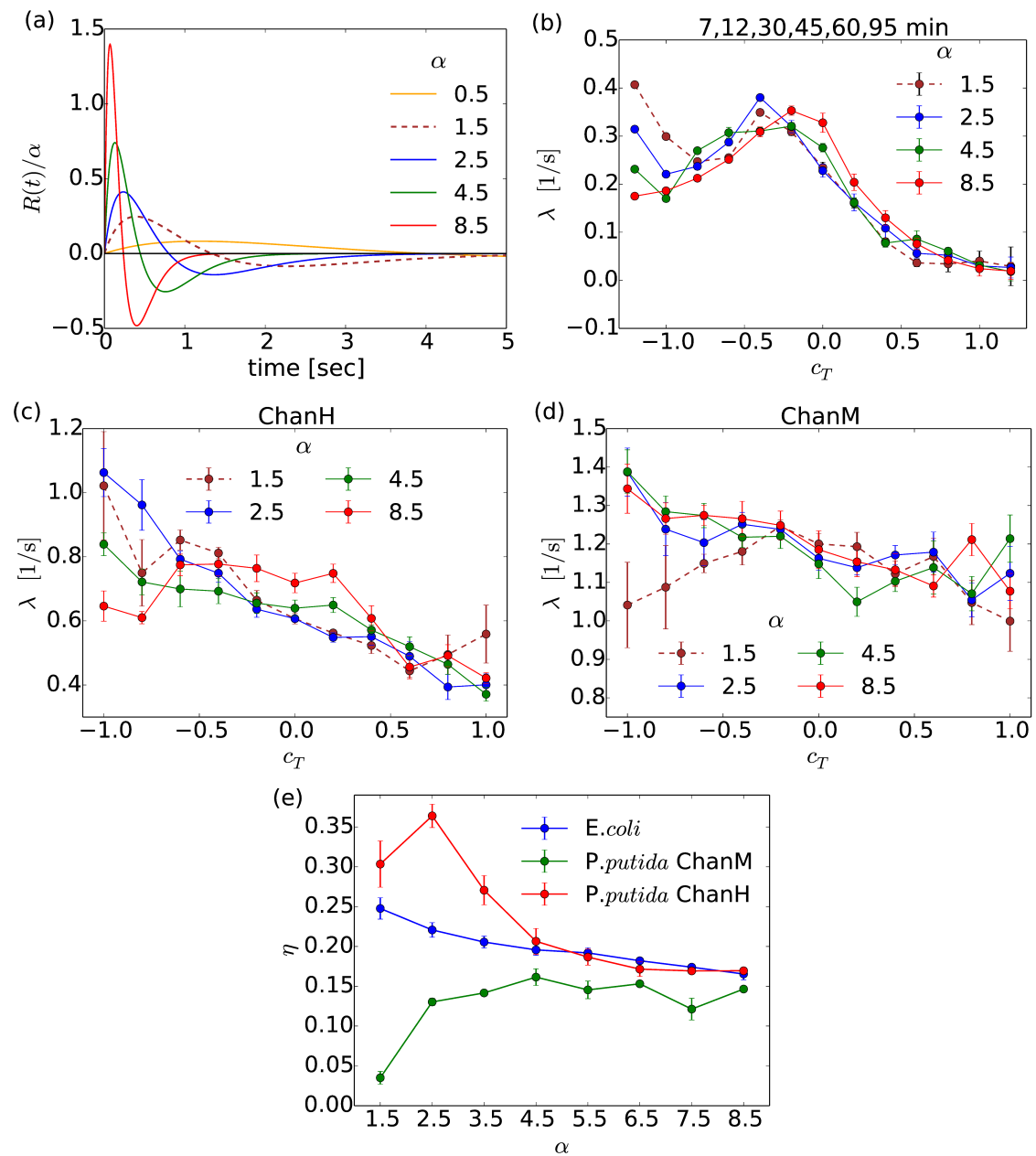


Figure 5.10.: (a) Several response functions with different relaxation parameter α as in Eq. (5.33). (b,c,d): The tumble rate λ conditioned on c_T as in Eq. (5.30) for *E.coli* (b), for *P.putida* with high background concentration (c), and for medium background concentration (d). The brown dashed curve corresponds to $\alpha = 1.5$, which approximates the response function measured for *E.coli*. Please note the different y -axis scales, in particular, the decrease in (c) is much more pronounced than in (d). (e) The chemotactic response strength η vs. α for *E.coli* and *P.putida* in the two channels ChanM and ChanH.

a smaller relaxation time of the response function than for *E.coli* [see Fig. 5.10(a)]

5.6. Conclusion

Concluding, we have presented a novel method to determine the tumbling behavior of bacteria. It is based on conditioned moments of their moving direction. We have calculated them for our theoretical model and for experimental trajectories. Matching these moments allows for inference of parameters associated to tumbling. With the inferred parameters the model can be used to define a tumble recognizer based on stochastic test theory. Exploiting the condition of the moments, we draw conclusions on chemotaxis and chemokinesis of the bacteria *E.coli* and *Pseudomonas putida*. First, we have confirmed the results of former studies by showing that *E.coli* is adapted to the chemotattractant aspartate, while *P.putida* is not adapted to benzoate. Second, we quantified the classical chemotactic strategy of both bacteria. For *E.coli* we detected a subpopulation, which biases its tumble angle significantly in response to the external gradient, thereby increasing its chemotactic velocity significantly. Last, by conditioning on the past trajectory, we gave evidence that the optimal response function for *P.putida* relaxes to zero faster than for *E.coli*.

Conclusions

Bridging the gap between biological and synthetic model systems is one of the major challenges in modern research [18, 22, 152]. Since physics is devoted to the procedure of reducing a system to its essential properties, its methods are particularly adequate for this effort. Indeed, the random walk of an active colloid and of a run-and-tumble bacterium might look different and its origins definitely are. However, in this thesis, we have seen various connections from a statistical point of view. The same is true for chemotaxis: a bacterium actively biases its random walk, while the colloid is driven by fluid flow on its surface. Still, in both cases a drift in gradient direction emerges, although noise typically dominates. For practical purposes, a detailed understanding of these connections is essential. Then, it might become possible to use biomimetic properties of colloidal matter to fulfill biological tasks with it.

This thesis contributes to the understanding of phoretic interactions in a system of active colloidal particles and elaborates a method to study chemotaxis in bacterial systems. It contains applications from chemical, physical and biological contexts treated with methods from statistical physics and probability theory. Thereby, it constitutes a contribution to interdisciplinary research.

In Chap. 2 we first introduced basic stochastic concepts and presented various ways to characterize stochastic processes. They turn out to be sufficiently general to be applicable in the biological as well as in the colloidal context the reason being that both fields operate on micron scale. We used these concepts to characterize the behavior of active particles. A dynamic model was introduced and the statistics of a self-propelling particle were discussed. Particular attention was laid on the study of their collective motion focusing on highly crowded systems where a non-equilibrium phase transition was discussed.

In Chap. 3 we started with an outline of the mechanism of chemotaxis in cellular systems. In particular, we presented the celebrated Keller-Segel model, which we later invoked for an analysis of active colloids. Last, we contrasted the concepts of chemotaxis and chemokinesis. We related them to various shapes of the chemotactic response function as well as to different interpretations of one single stochastic differential equation inspired by the seminal work of Mark J. Schnitzer [80].

In Chap. 4 we established a theoretical framework for the experiments presented in Ref. [14], which exhibit non-equilibrium cluster behavior in a system of synthetic particles. We adopted the theory of diffusiophoresis to the multi-particle system and showed that two interaction mechanisms induced by diffusiophoresis need to be considered. The

interactions are mediated by a chemical concentration field, as known from biological chemotaxis. Indeed, we were able to map our stochastic model equations to the Keller-Segel model, which permitted us to draw conclusions on the onset of the chemotactic collapse. We showed that this collapse may become unstable and for certain phoretic parameters pulsating behavior occurs. In the case when the two phoretic contributions give rise to competing attractive and repulsive interactions, we showed the emergence of dynamic clustering. In this situation particles merge and dissolve from clusters dynamically and we were able to calculate the according reaction rates. They provide a method to distinguish between the dynamic clustering 1 and dynamic clustering 2 states, which we had identified before by analyzing their respective cluster size distribution functions.

Finally, in Chap. 5, we presented a method to infer the tumbling behavior of bacteria. It was inspired by a procedure called conditional averaging, where the first two Kramers-Moyal coefficients are used to separate deterministic from stochastic motion in biological systems [49, 50]. We generalized it for the run-and-tumble random walk of bacteria by calculating more than the first two coefficients. We showed how to use this method for the definition of a novel, probabilistic tumble recognizer, which functions on the basis of the previously inferred parameters. In addition, it quantifies, for the first time, the intrinsic uncertainty in recognizing tumble events. Defining the condition of the Kramers-Moyal coefficients adequately, conclusions concerning chemotaxis and chemokinesis can be drawn. Experimental trajectories of the species *E. coli* and *P. putida* in gradients of a chemoattractant were analyzed by means of the inference method. In spite of the *temporal* nature of their bacterial chemotaxis, conditioning on the current moving direction is sufficient to draw conclusions on chemotactic strategies. First we confirm and quantify for both species the classical strategy reported in Ref. [46], i.e., adaption of the tumble rate to the chemical gradient. In the case of *E. coli*, we gave evidence that a small fraction of the investigated population applies a second chemotactic strategy, a so-called *angle bias*. This means that the bacterium alters its tumble angle depending on the chemical gradient direction. For the species *P. putida*, we showed that the background concentration of the nutrient benzoate significantly affects the tumbling statistics and the chemotactic behavior. Hence, this bacterium exhibits an example, where chemokinesis as well as chemotaxis are observed simultaneously. Last, we showed how different response functions can be tested within our framework.

In conclusion, we elucidated the concept of chemotaxis by studying it in colloidal as well as in bacterial systems. We theoretically rationalized recent experiments on active colloids and discussed bacterial chemotactic behavior with the aid of a novel inference method. The topics we touched in this thesis are far from being completely understood. Also, the methods we used or provided could be applied and refined into several directions. In the following, we want to discuss some of these aspects.

Outlook

Referring to the colloidal field, phoretic interactions of colloidal particles are mediated by a dynamically changing chemical concentration field. Instead of solving the according diffusion equation approximately, one might simulate their dynamical evolution considering flux conditions at all colloidal surfaces. In Ref. [153] reactions of reactants catalyzed by dumbbell particles were explicitly simulated and dynamic clustering for small clusters was indeed observed. Possibly, in the future such detailed simulations can be performed with larger system sizes using faster computers or algorithms in order to draw quantitative statistics from it.

We mentioned in Chap. 4 that the mapping of our model to the Keller-Segel equations allows us to draw conclusions on the collapsed state, however, it does not provide insight in dynamic clustering. In Ref. [154] oscillations have been observed when considering logistic growth in the system. Possibly, this could guide a way to design an extended Keller-Segel framework which captures the dynamic “birth and death” of clusters.

Furthermore, we think that experiments, which permit explicit control over the phoretic interaction strengths, would help to explore the rich state space of active colloidal systems. This would generate new insights in the emergent collective behavior of active colloids, which respond to chemical field gradients by diffusiophoresis.

Focusing on the biological part of this thesis, we discussed the concepts of chemokinesis and chemotaxis. When inferring the tumbling behavior of the bacterium *P.putida* in gradients of the nutrient *benzoate*, we indeed encountered both effects. As we have seen, *P.putida* has a very particular swimming mechanism with a peaked tumble distribution. It could be interesting to analyze this particular tumbling behavior with the formalism of Sec. 3.2.4. In numerical simulations, one could take into account that this organism typically lives in soil by simulating obstacles possibly with density gradients .

Concerning our moment method, it would be interesting to apply it to different bacterial random walks. Due to its universality, one can adapt it easily to a particular species. For instance, so-called magnetotactic bacteria [155, 156] experience a torque, which aligns their active motion with a magnetic field. Such an angular drift would be well captured in the context of our inference method by means of the first conditioned moment. Furthermore, a bimodal tumble distribution with two maxima was measured for maritime bacteria [69]. Relying on a model- and optimization-free approach, one could calculate a bimodality coefficient based on the third and fourth moments [157]. With our inference method, one could check for bimodality by assuming a sufficiently general tumble distribution as input. However, a more complex tumble distribution requires more parameters to describe it. To infer them, one could include the bacterial speed statistics being of particular interest for bacteria which modify their speed patterns with different swimming mechanisms [87, 156].

We have shown the existence of an angle bias for a subpopulation of *E.coli*, however, the mechanism behind it is unknown. Ref. [158] reports on correlations between clockwise rotation of nearby flagella, and the authors speculate that such dependencies could lead

to an angle bias. Indeed, the positions of attachment as well as the number of flagella vary significantly within different bacteria of one species [85] and between different bacterial species [159]. Possibly this diversity is the origin of different (chemo-) tactic strategies. We think that the moment method elaborated throughout this thesis could help to uncover more fascinating instances of bacterial ingenuity.

CM Inference method

A.1. Calculation of odd conditioned moments

Calculating the CMs for odd power n is not straight forward because they are defined as absolute values [see Eq. (5.8)]. We use $|a + b| = 2 \max(a, -b) - a + b$ and obtain for $n=1$:

$$\begin{aligned}
m_{\Delta t}^1(\theta)[\Theta] &= \langle |dN + dB|/\Delta t \mid \Theta(t) = \theta \rangle \\
&= \langle 2 \max(dB, -dN) - dB + dN \rangle / \Delta t \\
&= \langle 2 \max(dB, -dN) \rangle / \Delta t \\
&\approx 2(1 - \lambda\Delta t)0.5 \frac{\langle |dB| \rangle}{\Delta t} + 2\lambda 0.5 \langle |\beta| \rangle + 2\lambda 0.5 \langle dB \rangle \\
&= (1 - \lambda\Delta t) \langle |dB|/\Delta t \rangle + \lambda \langle |\beta| \rangle.
\end{aligned}$$

For the third equation we used Eq. (5.11). In the approximation line the first term represents the case when no tumbling occurs (probability $1 - \lambda\Delta t$) and $dB > 0$ (probability 0.5). The second term represents a tumbling with $dN < 0$ (probability 0.5) where we assume $|dB| < |dN|$. The third term appears for $dN > 0$, but since the maximum is always the Gaussian increment, this term vanishes.

In the same spirit we proceed for $n=3$:

$$\begin{aligned}
m_{\Delta t}^3(x)[\Theta] &= \langle 2 \max(dN^3 + dB^3, -3dN^2dB - 3dB^2dN) \rangle / \Delta t \\
&\approx (1 - \lambda\Delta t) m_{\Delta t}^3(x)[B] + \lambda \langle |\beta|^3 \rangle + 6\lambda\Delta t D_{\text{rot}} \langle |\beta| \rangle.
\end{aligned}$$

The first term in the last line refers to a no-tumbling situation, the second to a positive and the last term to a negative tumbling angle. For the latter we assume the right side of the max function in the second line to be larger than the left side and only the last term survives the average.

A.2. Materials and Methods

We here provide details of the experimental procedure and some data analysis referring to the bacterium *E.coli*.

Cell culture *E. coli* strain AW405 was streaked on 1.5% agar (AppliChem, Germany) containing Lysogeny broth (LB medium) (AppliChem, Germany) and grown at 37 °C. A single-colony isolate was used to inoculate 10 ml of LB medium in a 100 ml flask and grown over night in shaking culture (300 min⁻¹, 37 °C). The stationary culture was diluted 1:100 into 10 ml of fresh LB medium and grown \approx 3 h to an optical density at 600nm of OD₆₀₀ \approx 0.8 in mid-exponential phase. Bacteria were washed two times by centrifugation at 1000g for 10 min and carefully resuspended in 10 ml motility buffer (1 \times 10⁻² M potassium phosphate, 6.7 \times 10⁻² M NaCl, 1 \times 10⁻⁴ M EDTA and 0.5% (w/v) glucose; pH 7.0). Cells were diluted further to an OD₆₀₀ of 0.05 before filling them into the chemotaxis device.

Microfluidics and imaging We used a μ -Slide Chemotaxis 3D (ibidi, Martinsried, Germany) to generate stable linear gradients of the chemoattractant α -methyl-aspartate (Sigma-Aldrich, USA). First, the gradient region was filled with motility buffer as reported above, then the cell suspension was filled into the right reservoir of the channel. Lastly, the left reservoir was filled with motility buffer containing 0.5 mM α -methyl-aspartate. Imaging was done using an IX71 inverted microscope with a 20x UPLFLN-PH objective (both Olympus, Germany) in phase contrast mode with an attached Orca Flash 4.0 CMOS camera (Hamamatsu Photonics, Japan). All data was aquired at 20 Hz. Video sequences of 2 minutes each were recorded at 7, 12, 30, 45, 60, and 95 minutes after filling the channel. By recording some datasets with 1 μ M fluorescein added to the chemoattractant reservoir, we confirmed that the gradient was already established at the time of recording. Using confocal laser scanning microscopy on a channel filled only with buffer and buffer with fluorescein, we estimated the concentration profile of the chemoattractant at different times after filling. As shown in Fig. 5.2, the gradient is approximately linear already at 7 minutes after filling, and remains sufficiently stationary for the duration of the experiment.

Image processing and cell tracking Image sequences were exported from the camera manufacturers native data format to BigTIFF sequences and further processed using a custom program written in Matlab (version R2014a, The MathWorks, USA). For each image stack the pixel wise average projection was calculated, which was then used for background correction. Dividing each frame by the background image corrected for shading effects and yielded an image, which was free of non-moving objects. The resulting background corrected image stack was segmented using a Matlab version of the Maxentropy thresholding algorithm by Ref. [160]. To minimize noise introduced by the segmentation, the threshold was computed for each image separately and the median of these values was used to segment the whole stack. Small specks present after segmentation were removed by morphological opening and closing with a disk of equivalent radius of 0.3 μ m. Positions of cells were determined by computing the centroid of each

connected component in the binary image. Afterwards, only objects with areas between $1 \mu\text{m}^2$ to $15.6 \mu\text{m}^2$ were considered as single cells and used for further analysis. Finally, cell tracking was performed using a Matlab version of the particle tracking algorithm by Crocker and Grier [161].

Filtering Cells tend to tumble at the beginning and end of each trajectory, because this is the only way to enter the focal plane. Cells swimming at an angle to the plane only appear very briefly and are not tracked. Thus we disregard the first and last 0.5 s of each recorded track in order to avoid any biasing in the tumble rates. Because run-and-tumble detection is not feasible with very wobbly tracks, the dataset was filtered based on several criteria. Trajectories with a duration longer than 10 s and with a total displacement below $10 \mu\text{m}$ were discarded as well tracks with a median curvature above the 80th percentile.

Run-and-tumble recognition For the heuristic run-and-tumble recognition we sub-sample the track data by using only every third data point leading to an effective data rate of 6.6 Hz. Furthermore, we smooth the tracks by applying a 5-point, second-order Savitzky–Golay filter [162]. Smoothed tracks were used to compute frame-wise speed $v = \frac{\Delta s}{\Delta t}$, direction of propagation θ , and turn rate $\omega = \frac{\Delta \theta}{\Delta t}$. The tumble recognition algorithm characterizes tumbles based on variations in speed and turn rate as described in [87] and [48]. For the speed it first identifies local minima in the speed v at time points t_{\min} . The two adjacent maxima $t_{1,2}$ are then used to compute the depth of the minimum $\Delta v = \max[v(t_1) - v(t_{\min}), v(t_2) - v(t_{\min})]$. If the relative depth satisfies $\frac{\Delta v}{v(t_{\min})} > \alpha$ with $\alpha = 1$, the cell is considered to be tumbling for the time where $v(t) \leq v(t_{\min}) + 0.45 \Delta v$. For the turn rate we only consider the absolute value of the time series $\omega = |\omega|$. Local maxima are identified at times t_{\max} with adjacent minima at times $t_{1,2}$. If the total angular deviation between t_1 and t_2 satisfies $\sum_t \Delta \theta > \beta \sqrt{D_r(t_2 - t_1)}$, with $\beta = 3.5$ and $D_r = 0.1 \text{ rad}^2 \text{ s}^{-1}$ the cell is considered to be tumbling for the times where $|\omega(t_{\max}) - \omega(t)| \leq 0.85 \Delta \omega$. The relative change in turn rate is defined analogously to the speed case by $\Delta \omega = \max[\omega(t_{\max}) - \omega(t_1), \omega(t_{\max}) - \omega(t_2)]$.

A.3. Numerical details

In this section, we note some technical details, which might serve the reader for the practical realization of the moment method.

Bootstrap technique

In our fitting procedure we infer parameters from the trajectories by means of a non-linear optimization. Hence, the variance in the trajectories translates in a variance of

estimated parameters in a hardly predictable way. To obtain reliable standard deviations for our inferred parameters, we apply a bootstrap technique.

To this purpose, we call the set of n experimental trajectories $T_0 = \{t_1, \dots, t_N\}$. Now, we sample K new sets of trajectories $T_{\{1, \dots, K\}}$ each with N elements and define: $T_i := \{\tilde{t}_1, \dots, \tilde{t}_N\}$ where each \tilde{t}_j is sampled with the same probability out of the experimental trajectories of T_0 . By doing so, some of the trajectories of T_0 may appear multiple times in the sets $T_{j>0}$, others will not appear at all. Each new sample set T_j is then treated like T_0 as explained in the main text. In particular, we perform the parameter inference for each new trajectory set, from which we obtain K sets of parameters. The variance averaged over all sets represents the variance of the parameters. Its square root, i.e., the standard deviation, is plotted as error bars in the plots for λ and $\langle |\beta| \rangle$ in the main article.

Sampling trajectories

In fact, we do not only step once over each trajectory with fixed $\Delta t = 0.5$ (in the case of *E.coli*, the case for *P.putida* is analogous) thereby missing 90% of the original trajectory points. Rather more, we cut off the first m points of each trajectory starting with $m=7$ (corresponding to 0.35 seconds cut, the trajectory starting at 0.4 seconds) and iterate up to $m=16$ (0.8 seconds cut). In addition, we cut at least the last m trajectory points. Thereby, we obtain 10 sets of trajectories each associated with a certain m . This is effectively the T_0 (with the notation of the previous paragraph) trajectory set which we use.

This procedure has two effects: First of all, we cut a certain bit of the start and end of each trajectory avoiding incomplete tumbles. Second, we make sure that we effectively use each original data point for our data inference.

Optimization of parameters

As detailed in the main text, we fit the experimentally obtained moments with the aid of our analytical formulae for them. Our optimization problem can be stated as :

$$\mathbf{p}_{\text{opt}}(\mathbf{c}) = \mathit{arg} \min_{\mathbf{p}} |\mathbf{m}(\mathbf{c}) - \mathbf{f}(\mathbf{p})|, \quad (\text{A.1})$$

where $\mathbf{m}(\mathbf{c}) \in \mathbb{R}^6$ are the experimentally determined moments and $\mathbf{f} : \mathbb{R}^4 \rightarrow \mathbb{R}^6$ consists of the six calculated analytical formulae for the moments 5.19,5.15, 5.20,5.16,5.17 and 5.18. $\mathbf{p}_{\text{opt}}(\mathbf{c}) \in \mathbb{R}^4$ are the four parameters, which we seek to infer (for example for *E.coli* D_{rot} , λ , k and σ). To obtain the function $\mathbf{p}_{\text{opt}}(\mathbf{c})$ one needs to repeat the optimization for each different \mathbf{c} .

Since \mathbf{f} is a highly non-linear function, the optimization is executed numerically. For this purpose, we have checked the stability and accuracy of the optimization for various algorithms from the package “optimize” of the open source Python library “scipy”. Finally, we chose to sample the parameter space on a lattice (method “optimize.brute”)

to find the optimal starting point for another optimization procedure called “Downhill Simplex Algorithm” (method “optimize.fmin”). It finalizes the optimization in a non-gradient based search algorithm.

A.4. Trajectory analysis

For our method we only need to fix Δt , while for a heuristic tumble recognition, several parameters need to be adjusted. We present example trajectories together with their assigned speed statistics, which illustrate possible effects of particular parameter choices on the tumbling statistics.

Fig. A.1 shows a running averaged trajectory (colored points) of *E. coli* and its respective speed tracks. The triangles refer to the exact trajectory points, where the red ones mark every 10th data point corresponding to a time step $\Delta t = 0.5$ used for our inference. Based on the two prominent speed minima in the *smoothed* trajectory of Fig. A.1 on the left, a heuristic tumble detector might recognize 2 tumbles. In such a case, the correct large turning angle (following the original track, red triangles in Fig. A.1) is missed and does not contribute to the statistics. In Fig. A.2 we show another example, in which, depending on the parameters of the heuristic tumbling detector, there might be one, two or even three tumbles. Naturally, the number of recognized tumbles effects the overall tumble rate.

From this inspection of particular tumble events, we draw two conclusions. First, depending on the arbitrary parameters controlling the smoothing procedure, the trajectories may have considerably different shapes, in particular smaller tumble angles might be preferred (as described in the main text). Furthermore, the prediction of tumbles based on a heuristic tumble recognizer depends sensitively on the underlying threshold parameters. In the main text we referred to this fact as *uncertainty* in tumble recognition.

A.5. Chemotaxis in late trajectories $T = 30,45$ min. and $T = 60$ min.

In the main text we provided evidence for an angle bias in the 7, 12 min. case. Inspecting Figs. A.3(a)(c)(e), no clear trend in the mean tumble angle is recognizable, hence, there is no indication for an angle bias. However, at the right side the tumble rate depends much stronger on the prior moving direction than on the left side of the channel. In the middle part one detects a medium chemotactic response. The CM ratios support this finding, since in the levels, to which the curves converge, are increasingly different from the left side to the right side of the channel. This effect of the tumble rate has also been observed for the 7, 12 min. case. We conclude that, unlike the angle bias, the different dependencies on the tumble rate are not particular for early trajectories.

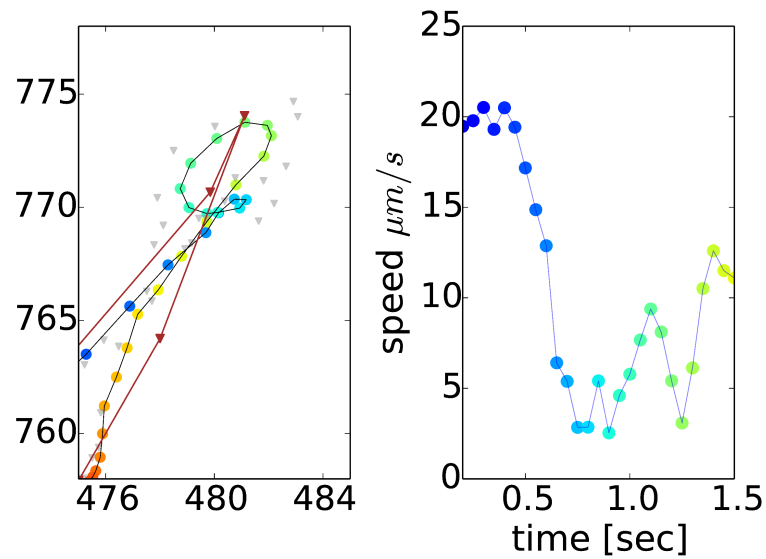


Figure A.1.: A tumble event of a particular trajectory of *E. coli* (left) together with the assigned speed values (right). Left: The original trajectory points as triangles with every 10th point in brown, the others in grey. Colored points are pseudo data points obtained by a running average over five points of the original trajectory. Right: A point with a particular color marks the speed at the pseudo trajectory point with matching color.

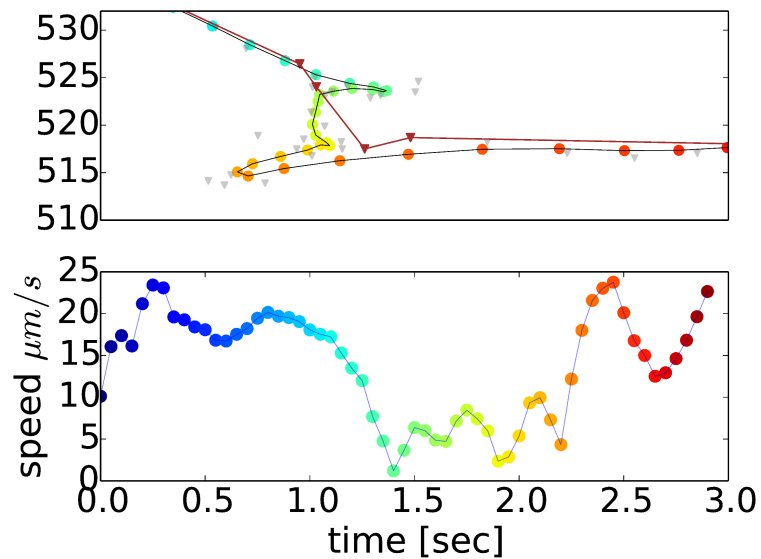


Figure A.2.: Another example of a tumble event (top) with its assigned speed values. Compare Fig. A.2

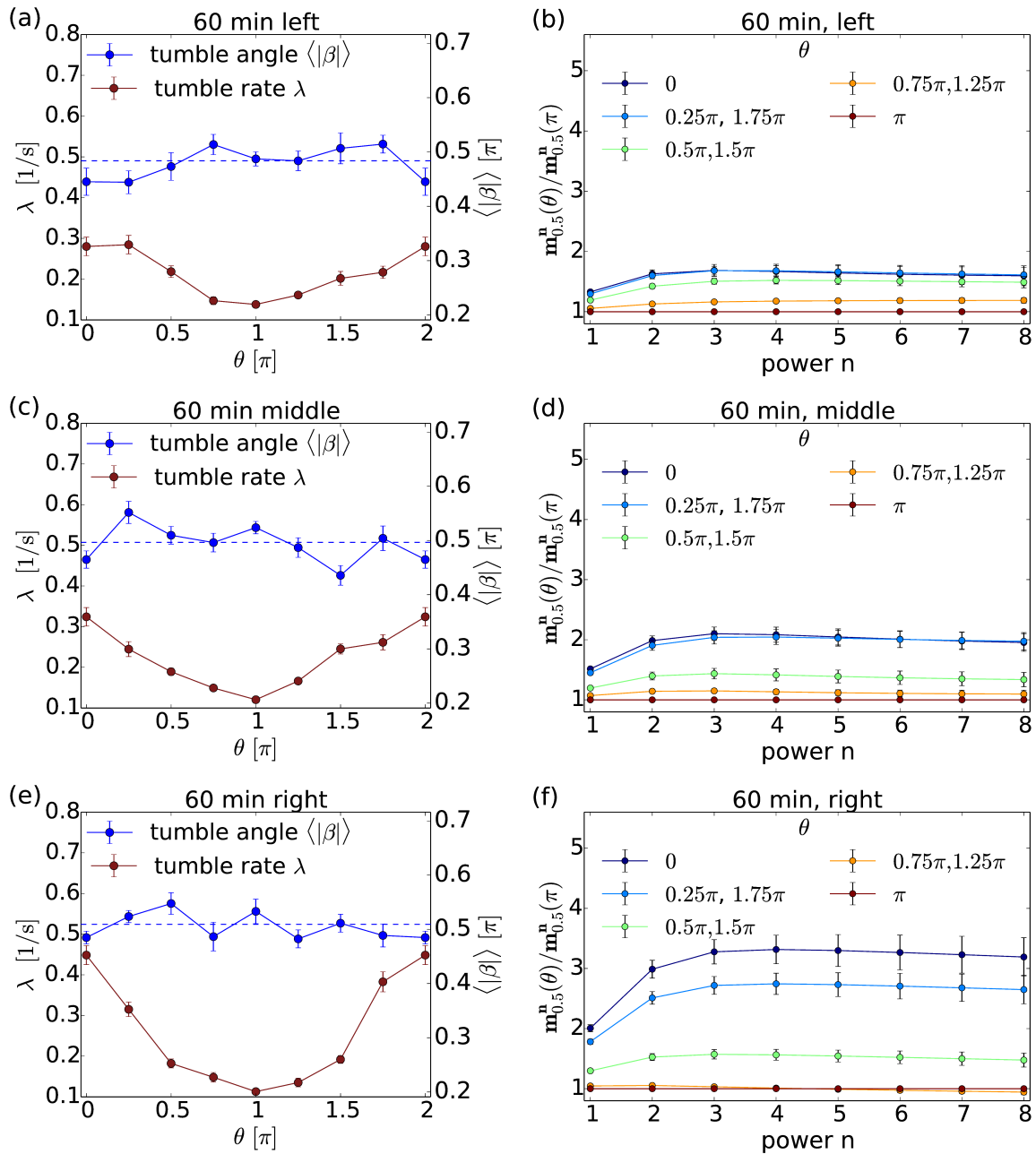


Figure A.3.: Same analysis as in Fig. 5.8 for *E.coli* after 60 minutes. No angle bias can be distinguished, however, we see larger variations in the tumblerate on the right than on the left side of the channel (red curves, left column).

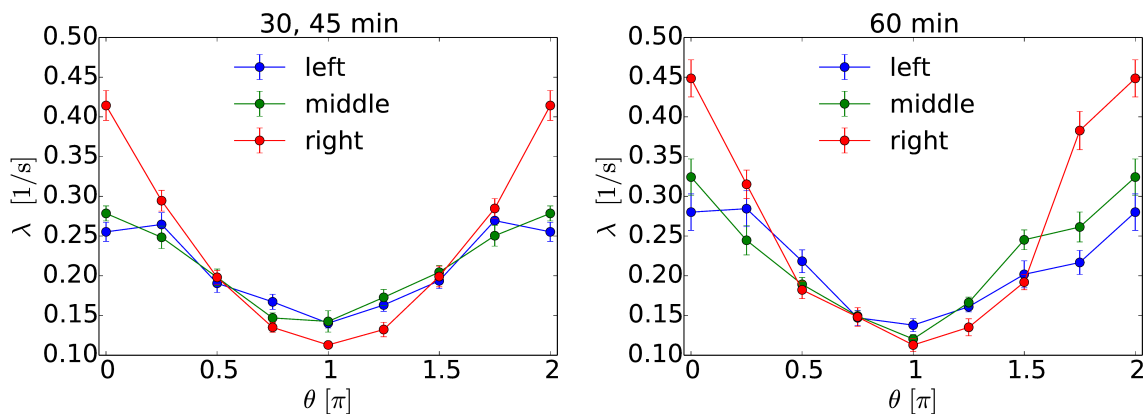


Figure A.4.: Tumble rates for (left) the 30 and 45 min. tracks and for (right) the 60 min. tracks, where the channels are divided in left, middle and right part.

A.6. Moments of P_β of *P.putida*

In the main text we defined the tumble angle distribution of *P.putida* as: $P_{\text{put}}(|\beta|) = [\exp(-\xi(\pi - |\beta|) + C)]/\mathcal{N}$. The normalization is calculated to $\mathcal{N} = \frac{1}{\xi} (\exp(\pi\xi) - 1) + C\pi$. We obtain for the n-th moment:

$$\langle |\beta|^n \rangle = \frac{1}{\mathcal{N}} \left[\frac{\exp(\pi\xi)}{\xi^{n+1}} \left(\sum_{i=1}^n [(-1)^{n-i} n! (\xi\pi)^i / i!] + (-1)^n n! \right) + \frac{C}{n+1} \pi^{n+1} - \frac{(-1)^n n!}{\xi^{n+1}} \right] \quad (\text{A.2})$$

A.7. CM ratios for *P.putida*

Here we present the CM ratios for *P.putida*, all of which converge almost exactly to constants.

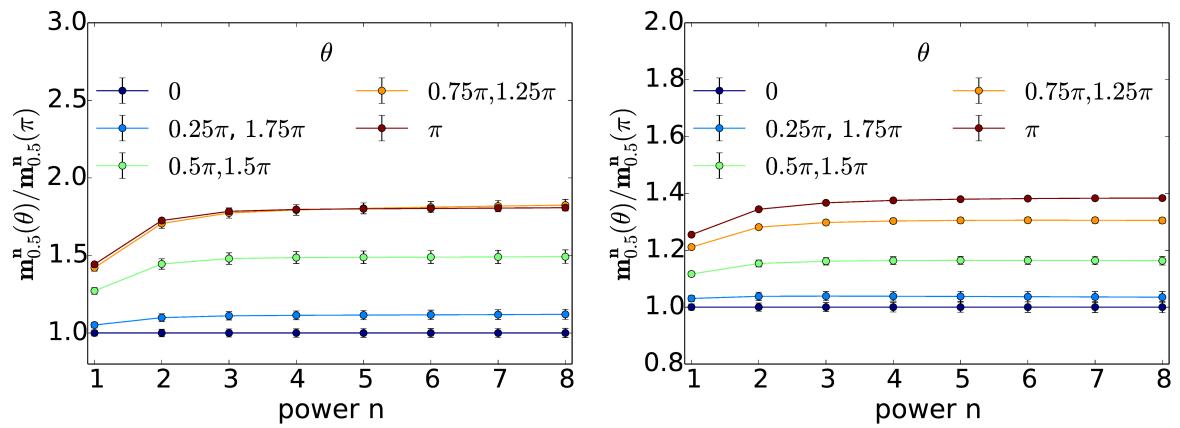


Figure A.5.: CM ratios as for example in Fig. 5.7 for *P.putida*. (a) High background concentration and gradient strength. (b) Medium background concentration and gradient strength.

List of publications

Related to this thesis

- O. Pohl and H. Stark, “Dynamic clustering and chemotactic collapse of self-phoretic active particles”, *Phys. Ref. Lett.* **35**, 238303 (2014).
- O. Pohl and H. Stark, “Self-phoretic active particles interacting by diffusiophoresis: A numerical study of the collapsed state and dynamic clustering”, *Eur. Phys. J. E* **36**, 1 (2015).
- O. Pohl and H. Stark, “Inferring the chemotactic strategy of *P. putida* and *E. coli* using modified Kramers-Moyal coefficients”, submitted to *PLoS Comput. Biol.* (2016).

Others

- A. Attanasi, A. Cavagna, L. Del Castello, I. Giardina, T. Grigera, A. Jelić, S. Melillo, L. Parisi, O. Pohl, E. Shen, and others, “Information transfer, behavioural inertia in starling flocks”, *Nature Phys.* **10**, 691 (2014).
- W. Bialek, A. Cavagna, I. Giardina, T. Mora, O. Pohl, E. Silvestri, M. Viale, and A.M Walczak, “Social interactions dominate speed control in poising natural flocks near criticality”, *PNAS* **111**, 7212 (2014).
- A. Attanasi, A. Cavagna, L. Del Castello, I. Giardina, S. Melillo, L. Parisi, O. Pohl, B. Rossaro, E. Shen, E. Silvestri, and others, “Finite-size scaling as a way to probe near-criticality in natural swarms”, *Phys. Rev. Lett.* **113**, 238102 (2014).
- A. Attanasi, A. Cavagna, L. Del Castello, I. Giardina, S. Melillo, L. Parisi, O. Pohl, B. Rossaro, E. Shen, E. Silvestri, and others, “Collective behaviour without collective order in wild swarms of midges”, *PLoS. Comput. Biol.* **10**, e1003697 (2014).

Bibliography

- [1] J. Adler, “Chemotaxis in bacteria,” *Science* **153**, 708 (1966).
- [2] J. T. Bonner and L. J. Savage, “Evidence for the formation of cell aggregates by chemotaxis in the development of the slime mold *dictyostelium discoideum*,” *J. Exp. Zool.* **106**, 1 (1947).
- [3] B. M. Friedrich and F. Jülicher, “Chemotaxis of sperm cells,” *PNAS* **104**, 13256 (2007).
- [4] A. Celani, E. Villermaux, and M. Vergassola, “Odor landscapes in turbulent environments,” *Phys. Rev. X* **4**, 041015 (2014).
- [5] L. Hall-Stoodley, J. W. Costerton, and P. Stoodley, “Bacterial biofilms: from the natural environment to infectious diseases,” *Nature Rev. Microbiol.* **2**, 95 (2004).
- [6] I. S. Aranson, “Collective behavior in out-of-equilibrium colloidal suspensions,” *C. R. Acad. Sci.* **14**, 518 (2013).
- [7] J. Bialké, T. Speck, and H. Löwen, “Active colloidal suspensions: Clustering and phase behavior,” *J. Non-Cryst. Solids* **407**, 367 (2015).
- [8] H.-R. Jiang, N. Yoshinaga, and M. Sano, “Active motion of a janus particle by self-thermophoresis in a defocused laser beam,” *Phys. Rev. Lett.* **105**, 268302 (2010).
- [9] R. Golestanian, “Collective behavior of thermally active colloids,” *Phys. Rev. Lett.* **108**, 038303 (2012).
- [10] J. L. Moran and J. Posner, “Locomotion of electrocatalytic nanomotors due to reaction induced charge autoelectrophoresis,” *Phys. Rev. E.* **81**, 065302 (2010).
- [11] W. F. Paxton, A. Sen, and T. E. Mallouk, “Motility of catalytic nanoparticles through self-generated forces,” *Chem. Eur. J.* **11**, 6462 (2005).
- [12] S. Thutupalli, R. Seemann, and S. Herminghaus, “Swarming behavior of simple model squirmers,” *New J. Phys.* **13**, 073021 (2011).
- [13] M. Schmitt and H. Stark, “Swimming active droplet: A theoretical analysis,” *EPL* **101**, 44008 (2013).
- [14] I. Theurkauff, C. Cottin-Bizonne, J. Palacci, C. Ybert, and L. Bocquet, “Dynamic clustering in active colloidal suspensions with chemical signaling,” *Phys. Rev. Lett.* **108**, 268303 (2012).

- [15] I. Buttinoni, J. Bialke, F. Kümmel, H. Löwen, C. Bechinger, and T. Speck, “Active colloidal suspensions: Clustering and phase behavior,” *Phys. Rev. Lett.* **110**, 238301 (2013).
- [16] P. Malgaretti, I. Pagonabarraga, and J. M. Rubí, “Cooperative rectification in confined Brownian ratchets,” *Phys. Rev. E* **85**, 010105 (2012).
- [17] R. Soto and R. Golestanian, “Self-assembly of catalytically active colloidal molecules: Tailoring activity through surface chemistry,” *Phys. Rev. Lett.* **112**, 068301 (2014).
- [18] Z. Zeravcic and M. P. Brenner, “Self-replicating colloidal clusters,” *PNAS* **111**, 1748 (2014).
- [19] S. Ramaswamy, “The mechanics and statistics of active matter,” *Annu. Rev. Condens. Matter Phys.* **1** (2010).
- [20] S. Henkes, Y. Fily, and M. C. Marchetti, “Long-lived giant number fluctuations in a swarming granular nematic,” *Phys. Rev. E* **84**, 040301 (2011).
- [21] G. S. Redner, M. F. Hagan, and A. Baskaran, “Structure and dynamics of a phase-separating active colloidal fluid,” *Phys. Rev. Lett.* **110**, 055701 (2013).
- [22] M. C. Marchetti, J. F. Joanny, S. Ramaswamy, T. B. Liverpool, J. Prost, M. Rao, and R. A. Simha, “Hydrodynamics of soft active matter,” *Rev. Mod. Phys.* **85**, 1143 (2013).
- [23] M. E. Cates and J. Tailleur, “Motility-induced phase separation,” *Annu. Rev. Condens. Matter Phys.* **6**, 219 (2015).
- [24] A. Attanasi, A. Cavagna, L. D. Castello, I. Giardina, T. Grigera, A. Jelić, S. Melillo, L. Parisi, O. Pohl, E. Shen, *et al.*, “Information transfer and behavioural inertia in starling flocks,” *Nature Phys.* **10**, 691 (2014).
- [25] W. Bialek, A. Cavagna, I. Giardina, T. Mora, O. Pohl, E. Silvestri, M. Viale, and A. Walczak, “Social interactions dominate speed control in poising natural flocks near criticality,” *PNAS* **111**, 7212 (2014).
- [26] A. Attanasi, A. Cavagna, L. D. Castello, I. Giardina, S. Melillo, L. Parisi, O. Pohl, B. Rossaro, E. Shen, E. Silvestri, *et al.*, “Finite-size scaling as a way to probe near-criticality in natural swarms,” *Phys. Rev. Lett.* **113**, 238102 (2014).
- [27] Y. Katz, K. Tunstrøm, C. C. Ioannou, C. Christos, C. Huepe, and I. D. Couzin, “Inferring the structure and dynamics of interactions in schooling fish,” *PNAS* **108**, 18720 (2011).

-
- [28] H. Levine, I. Aranson, L. Tsimring, and T. V. Truong, “Positive genetic feedback governs cAMP spiral wave formation in dictyostelium,” *PNAS* **93**, 6382 (1996).
- [29] T. Vicsek, A. Czirók, E. Ben-Jacob, I. Cohen, and O. Shochet, “Novel type of phase transition in a system of self-driven particles,” *PRL* **75**, 1226 (1995).
- [30] W. Bialek, A. Cavagna, I. Giardina, T. Mora, E. Silvestri, M. Viale, and A. M. Walczak, “Statistical mechanics for natural flocks of birds,” *PNAS* **109**, 4786 (2012).
- [31] K. Schaar, A. Zöttl, and H. Stark, “Detention times of microswimmers close to surfaces: Influence of hydrodynamic interactions and noise,” *Phys. Rev. Lett.* **115**, 038101 (2015).
- [32] S. Stas, J.-H. Jeon, R. Metzler, and E. Barkai, “Single particle tracking in systems showing anomalous diffusion: the role of weak ergodicity breaking,” *Phys. Chem. Chem. Phys.* **13**, 1800 (2011).
- [33] E. Barkai, Y. Garini, and R. Metzler, “Strange kinetics of single molecules in living cells,” *Phys. Today* **65**, 29 (2012).
- [34] Y. Fily and M. C. Marchetti, “Athermal phase separation of self-propelled particles with no alignment,” *Phy. Rev. Lett.* **108**, 235702 (2012).
- [35] J. Palacci, S. Sacanna, A. P. Steinberg, D. J. Pine, and P. M. Chaikin, “Living crystals of light-activated colloidal surfers,” *Science* **339**, 936 (2013).
- [36] J. L. Anderson, “Colloid transport by interfacial forces,” *Ann. Rev. Fluid Mech.* **21**, 61 (1989).
- [37] M. E. Cates and J. Tailleur, “When are active Brownian particles and run-and-tumble particles equivalent? Consequences for motility-induced phase separation,” *EPL* **101**, 20010 (2013).
- [38] J. Bialke, H. Löwen, and T. Speck, “Microscopic theory for the phase separation of self-propelled repulsive disks,” *Europhys. Lett.* **103**, 30008 (2013).
- [39] T. Speck, J. Bialke, A. M. Menzel, and H. Löwen, “Effective cahn-hilliard equation for the phase separation of active Brownian particles,” *Phys. Rev. Lett.* **112**, 218304 (2014).
- [40] S. Saha, R. Golestanian, and S. Ramaswamy, “Clusters, asters, and collective oscillations in chemotactic colloids,” *Phys. Rev. E* **89**, 062316 (2014).
- [41] E. F. Keller and L. A. Segel, “Model for chemotaxis,” *J. Theor. Biol.* **26**, 399 (1970).

- [42] J. Taktikos, V. Zaburdaev, and H. Stark, “Collective dynamics of model microorganisms with chemotactic signaling,” *Phys. Rev. E* **85**, 051901 (2012).
- [43] T. S. Shimizu, N. L. Novère, M. D. Levin, A. J. Bevil, B. J. Sutton, and D. Bray, “Molecular model of a lattice of signalling proteins involved in bacterial chemotaxis,” *Nat. cell. biol.* **2**, 792 (2000).
- [44] V. Sourjik, “Receptor clustering and signal processing in *E. coli* chemotaxis,” *Trends microbiol.* **12**, 569 (2004).
- [45] H. C. Berg, *E. coli in Motion* (Springer Science & Business Media, 2008).
- [46] H. C. Berg and D. A. Brown, “Chemotaxis in *Escherichia coli* analysed by three-dimensional tracking,” *Nature* **239**, 500 (1972).
- [47] S. M. Block, J. E. Segall, and H. C. Berg, “Impulse responses in bacterial chemotaxis,” *Cell* **31**, 215 (1982).
- [48] J.-B. Masson, G. Voisinne, J. Wong-Ng, A. Celani, and M. Vergassola, “Noninvasive inference of the molecular chemotactic response using bacterial trajectories,” *PNAS* **109**, 1802 (2012).
- [49] C. A. Yates, R. Erban, C. Escudero, I. D. Couzin, J. Buhl, I. G. Kevrekidis, P. K. Maini, and D. J. T. Sumpter, “Inherent noise can facilitate coherence in collective swarm motion,” *PNAS* **106**, 5464 (2009).
- [50] G. Amselem, M. Theves, A. Bae, E. Bodenschatz, and C. Beta, “A stochastic description of *dictyostelium* chemotaxis,” *PLOS ONE* **7**, e37213 (2012).
- [51] J. Saragosti, V. Calvez, N. Bournaveas, B. Perthame, A. Buguin, and P. Silberzan, “Directional persistence of chemotactic bacteria in a traveling concentration wave,” *PNAS* **108**, 16235 (2011).
- [52] O. Pohl and H. Stark, “Dynamic clustering and chemotactic collapse of self-phoretic active particles,” *Phys. Rev. Lett.* **112**, 238303 (2014).
- [53] O. Pohl and H. Stark, “Self-phoretic active particles interacting by diffusiophoresis: A numerical study of the collapsed state and dynamic clustering,” *EPJ E* **38**, 1 (2015).
- [54] R. Brown, “Xxvii. a brief account of microscopical observations made in the months of june, july and august 1827, on the particles contained in the pollen of plants; and on the general existence of active molecules in organic and inorganic bodies,” *Philosophical Magazine* **4**, 161 (1828).

-
- [55] P. Pearle, B. Collett, K. Bart, D. Bilderback, D. Newman, and S. Samuels, “What Brown saw and you can too,” *Am. J. Phys.* **78**, 1278 (2010).
- [56] L. Arnold, “Stochastic differential equations,” New York (1974).
- [57] F. C. Klebaner *et al.*, *Introduction to stochastic calculus with applications*, Vol. 57 (World Scientific, 2005).
- [58] H. Risken, *Fokker-planck equation* (Springer, 1984).
- [59] C. W. Gardiner *et al.*, *Handbook of stochastic methods*, Vol. 3 (Springer Berlin, 1985).
- [60] E. Errais, “Financial modeling: A backward stochastic differential equations perspective,” *Quant. Finance* , 1 (2015).
- [61] J. Strefler, W. Ebeling, E. Gudowska-Nowak, and L. Schimansky-Geier, “Dynamics of individuals and swarms with shot noise induced by stochastic food supply,” *Eur. Phys. J. B* **72**, 597 (2009).
- [62] Y. M. Blanter and M. Büttiker, “Shot noise in mesoscopic conductors,” *Phys. rep.* **336**, 1 (2000).
- [63] M. J. Richardson and R. Swarbrick, “Firing-rate response of a neuron receiving excitatory and inhibitory synaptic shot noise,” *Phys. Rev. Lett.* **105**, 178102 (2010).
- [64] V. Zaburdaev, S. Denisov, and J. Klafter, “Lévy walks,” *Rev. Mod. Phys.* **87**, 483 (2015).
- [65] H.-O. Georgii, *Stochastics: introduction to probability and statistics* (Walter de Gruyter, 2013).
- [66] F. T. Bruss and J. B. Robertson, “Wald’s lemma for sums of order statistics of iid random variables,” *Adv. Appl. Probab.* , 612 (1991).
- [67] S. G. Kou, “Jump-diffusion models for asset pricing in financial engineering,” *Handbooks in operations research and management science* **15**, 73 (2007).
- [68] C. Ball and A. Roma, “A jump diffusion model for the european monetary system,” *J. Int. Money Financ.* **12**, 475 (1993).
- [69] L. Xie, T. Altindal, S. Chattopadhyay, and X.-L. Wu, “Bacterial flagellum as a propeller and as a rudder for efficient chemotaxis,” *PNAS* **108**, 2246 (2011).

- [70] P. Friedler, S. Borgmann, and E.-B. Bröcker, “Amoeboid leukocyte crawling through extracellular matrix: lessons from the dictyostelium paradigm of cell movement,” *J. Leukoc. Biol.* **70**, 491 (2001).
- [71] D. Alizadehrad, T. Krüger, M. Engstler, and H. Stark, “Simulating the complex cell design of trypanosoma brucei and its motility,” *PLoS Comput. Biol.* **11**, e1003967 (2015).
- [72] L. Zhang, J. J. Abbott, L. Dong, B. E. Kratochvil, D. Bell, and B. J. Nelson, “Artificial bacterial flagella: Fabrication and magnetic control,” *Appl. Phys. Lett.* **94**, 064107 (2009).
- [73] R. Di Leonardo, L. Angelani, D. Dell’Arciprete, G. Ruocco, V. Iebba, S. Schippa, M. Conte, F. Mecarini, F. De Angelis, and E. Di Fabrizio, “Bacterial ratchet motors,” *Proceedings of the National Academy of Sciences* **107**, 9541 (2010).
- [74] V. Narayan, S. Ramaswamy, and N. Menon, “Long-lived giant number fluctuations in a swarming granular nematic,” *Science* **317**, 105 (2007).
- [75] H.-P. Zhang, A. Be’er, E.-L. Florin, and H. L. Swinney, “Collective motion and density fluctuations in bacterial colonies,” *PNAS* **107**, 13626 (2010).
- [76] F. Schweitzer, W. Ebeling, and B. Tilch, “Complex motion of Brownian particles with energy depots,” *Phys. Rev. Lett.* **80**, 5044 (1998).
- [77] F. Peruani and L. G. Morelli, “Self-propelled particles with fluctuating speed and direction of motion in two dimensions,” *Phys. Rev. Lett.* **99**, 010602 (2007).
- [78] J. Taktikos, V. Zaburdaev, and H. Stark, “Modeling a self-propelled autochemotactic walker,” *Phys. Rev. E* **84**, 041924 (2011).
- [79] I. Buttinoni, J. Bialké, F. Kümmel, H. Löwen, C. Bechinger, and T. Speck, “Dynamical clustering and phase separation in suspensions of self-propelled colloidal particles,” *Phys. Rev. Lett.* **110**, 238301 (2013).
- [80] M. J. Schnitzer, “Theory of continuum random walks and application to chemotaxis,” *Phys. Rev. E* **48**, 2553 (1993).
- [81] J. Tailleur and M. E. Cates, “Statistical mechanics of interacting run-and-tumble bacteria,” *Phys. Rev. Lett.* **100**, 218103 (2008).
- [82] S. Childress and J. K. Percus, “Nonlinear aspects of chemotaxis,” *Math. Bioscience* **56**, 217 (1981).

-
- [83] W. Jäger and S. Luckhaus, “On explosions of solutions to a system of partial differential equations modelling chemotaxis,” *J. Am. Math. Soc.* **329**, 819 (1992).
- [84] M. P. Brenner, L. S. Levitov, and E. O. Budrene, “Physical mechanisms for chemotactic pattern formation by bacteria,” *Biophys. J.* **74**, 1677 (1998).
- [85] G. N. Cohen-Ben-Lulu, N. R. Francis, E. Shimoni, D. Noy, Y. Davidov, K. Prasad, Y. Sagi, G. Cecchini, R. M. Johnstone, and M. Eisenbach, “The bacterial flagellar switch complex is getting more complex,” *EMBO J.* **27**, 1134 (2008).
- [86] L. Molinao, C. Ramos, E. Duque, M. C. Ronchel, J. M. Garcia, L. Wyke, and J. L. Ramos, “Survival of *Pseudomonas putida* kt2440 in soil and in the rhizosphere of plants under greenhouse and environmental conditions,” *Soil Biol. Biochem.* **32**, 315 (2000).
- [87] M. Theves, J. Taktikos, V. Zaburdaev, H. Stark, and C. Beta, “A bacterial swimmer with two alternating speeds of propagation,” *Biophys. J.* **105**, 1915 (2013).
- [88] H. G. Othmer, X. Xin, and C. Xue, “Excitation and adaptation in bacteria—a model signal transduction system that controls taxis and spatial pattern formation,” *Int. J. Mol. Sci.* **14**, 9205 (2013).
- [89] <http://www.nature-education.org/water-ecoli.html>.
- [90] C. S. Harwood, K. Fosnaugh, and M. Dispensa, “Flagellation of *Pseudomonas putida* and analysis of its motile behavior.” *J. Bact.* **171**, 4063 (1989).
- [91] E. Korobkova, T. Emonet, J. M. G. Vilar, T. S. Shimizu, and P. Cluzel, “From molecular noise to behavioural variability in a single bacterium,” *Nature* **428**, 574 (2004).
- [92] P.-G. De Gennes, “Chemotaxis: the role of internal delays,” *European Biophysics Journal* **33**, 691 (2004).
- [93] Y. V. Kalinin, L. Jiang, Y. Tu, and M. Wu, “Logarithmic sensing in *Escherichia coli* bacterial chemotaxis,” *Biophys. J.* **96**, 2439 (2009).
- [94] J. K. G. Dhont, “An introduction to dynamics of colloids,” (1996).
- [95] C. L. Fefferman, “Existence and smoothness of the Navier-stokes equation,” *The millennium prize problems*, 57 (2000).
- [96] A. Malevanets and R. Kapral, “Mesoscopic model for solvent dynamics,” *J.Chem.Phys.* **110**, 8605 (1999).

- [97] B. Dünweg and A. J. C. Ladd, “Lattice boltzmann simulations of soft matter systems,” (2008).
- [98] E. M. Purcell, “Life at low reynolds number,” *Am. J. Phys* **45**, 3 (1977).
- [99] J. Happel and H. Brenner, *Low Reynolds number hydrodynamics: with special applications to particulate media*, Vol. 1 (Springer Science & Business Media, 2012).
- [100] H. A. Stone and A. D. T. Samuel, “Propulsion of microorganisms by surface distortions,” *Phys. Rev. Lett.* **77**, 4102 (1996).
- [101] J. L. Anderson, “Effect of nonuniform zeta potential on particle movement in electric fields,” *Journal of colloid and interface science* **105**, 45 (1985).
- [102] A. Zöttl and H. Stark, “Hydrodynamics determines collective motion and phase behavior of active colloids in quasi-two-dimensional confinement,” *Phys. Rev. Lett.* **112**, 118101 (2014).
- [103] V. Narayan, S. Ramaswamy, and N. Menon, “Long-lived giant number fluctuations in a swarming granular nematic,” *Science* **317**, 105 (2007).
- [104] R. W. Nash, R. Adhikari, J. Tailleur, and M. E. Cates, “Run-and-tumble particles with hydrodynamics: sedimentation, trapping, and upstream swimming,” *Phys. Rev. Lett.* **104**, 258101 (2010).
- [105] M. Hennes, K. Wolff, and H. Stark, “Self-induced polar order of active Brownian particles in a harmonic trap,” *Phys. Rev. Lett.* **112**, 238104 (2014).
- [106] W. M. Durham, J. O. Kessler, and R. Stocker, “Disruption of vertical motility by shear triggers formation of thin phytoplankton layers,” *Science* **323**, 1067 (2009).
- [107] A. Zöttl and H. Stark, “Nonlinear dynamics of a microswimmer in poiseuille flow,” *Phys. Rev. Lett.* **108**, 218104 (2012).
- [108] X. Garcia, S. Rafai, and P. Peyla, “Light control of the flow of phototactic microswimmer suspensions,” *Phys. Rev. Lett.* **110**, 138106 (2013).
- [109] A. Zöttl and H. Stark, “Periodic and quasiperiodic motion of an elongated microswimmer in poiseuille flow,” *Eur. Phys. J. E* **36**, 4 (2013).
- [110] J. Palacci, C. Cottin-Bizonne, C. Ybert, and L. Bocquet, “Sedimentation and effective temperature of active colloidal suspensions,” *Phys. Rev. Lett.* **105**, 088304 (2010).
- [111] M. Enculescu and H. Stark, “Active colloidal suspensions exhibit polar order under gravity,” *Phys. Rev. Lett.* **107**, 058301 (2011).

-
- [112] K. Wolff, A. M. Hahn, and H. Stark, “Sedimentation and polar order of active bottom-heavy particles,” *EPJ E* **36**, 1 (2013).
- [113] Q. Liu, A. Doelman, V. Rottschäfer, M. de Jager, P. M. Herman, M. Rietkerk, and J. van de Koppel, “Phase separation explains a new class of self-organized spatial patterns in ecological systems,” *PNAS* **110**, 11905 (2013).
- [114] R. C. Gerum, B. Fabry, C. Metzner, M. Beaulieu, A. Ancel, and D. P. Zitterbart, “The origin of traveling waves in an emperor penguin huddle,” *New. J. Phys.* **15**, 125022 (2013).
- [115] H. H. Wensink, J. Dunkel, S. Heidenreich, K. Drescher, R. E. Goldstein, H. Löwen, and J. M. Yeomans, “Meso-scale turbulence in living fluids,” *PNAS* **109**, 14308 (2012).
- [116] D.-P. Häderi, A. Rosumi, J. Schäfer, and R. Hemmersbach, “Gravitaxis in the flagellate euglena gracilis controlled by an active gravireceptor,” *J. Plant Physiol.* **146**, 474 (1995).
- [117] B. Ten Hagen, F. Kümmel, R. Wittkowski, D. Takagi, H. Löwen, and C. Bechinger, “Gravitaxis of asymmetric self-propelled colloidal particles,” *Nat. Commun.* **5** (2014).
- [118] K. Maeda, Y. Imae, J.-I. Shioi, and F. Oosawa, “Effect of temperature on motility and chemotaxis of escherichia coli.” *J. Bacteriol.* **127**, 1039 (1976).
- [119] J. A. Cohen and R. Golestanian, “Emergent cometlike swarming of optically driven thermally active colloids,” *Phys. Rev. Lett.* **112**, 068302 (2014).
- [120] M. Braun, A. Würger, and F. Cichos, “Trapping of single nano-objects in dynamic temperature fields,” *Phys. Chem. Chem. Phys.* **16**, 15207 (2014).
- [121] T. Bickel, G. Zecua, and A. Würger, “Polarization of active janus particles,” *Phys. Rev. E* **89**, 050303(R) (2014).
- [122] F. Ginot, I. Theurkauff, D. Levis, C. Ybert, L. Bocquet, L. Berthier, and C. Cottin-Bizonne, “Nonequilibrium equation of state in suspensions of active colloids,” *Phys. Rev. X* **5**, 011004 (2015).
- [123] L. F. Valadares, Y.-G. Tao, N. S. Zacharia, V. Kitaev, F. Galembeck, R. Kapral, and G. A. Ozin, “Catalytic nanomotors: Self-propelled sphere dimers,” *Small* **6**, 565 (2010).
- [124] J. L. Moran and J. Posner, “Electrokinetic locomotion due to reaction-induced charge auto-electrophoresis,” *J.Fluid Mech.* **680**, 31 (2011).

- [125] P. de Buyl and R. Kapral, “Phoretic self-propulsion: a mesoscopic description of reaction dynamics that powers motion,” *Nanoscale* **5**, 1337 (2013).
- [126] K. Drescher, J. Dunkel, L. H. Cisneros, S. Ganguly, and R. E. Goldstein, “Fluid dynamics and noise in bacterial cell–cell and cell–surface scattering,” *PNAS* **108**, 10940 (2011).
- [127] H. Masoud and M. J. Shelley, “Collective surfing of chemically active particles,” *Phys. Rev. Lett.* **112**, 128304 (2014).
- [128] D. Levis and L. Berthier, “Clustering and heterogeneous dynamics in a kinetic monte carlo model of self-propelled hard disks,” *Phys. Rev. E* **89**, 062301 (2014).
- [129] T. J. Newman and R. Grima, “Many-body theory of chemotactic cell-cell interactions,” *Phys. Rev. E* **70**, 051916 (2004).
- [130] O. Ciftja and I. Hysi, “The electrostatic potential of a uniformly charged disk as the source of novel mathematical identities,” *Appl. Math. Lett.* **24**, 1919 (2011).
- [131] S. Gueron and S. A. Levin, “The dynamics of group formation,” *Math. Biosci.* **128**, 243 (1995).
- [132] F. Peruani, J. Starruß, V. Jakovljevic, L. S. Andersen, A. Deutsch, and M. Bär, “Collective motion and nonequilibrium cluster formation in colonies of gliding bacteria,” *Phys. Rev. Lett.* **108**, 098102 (2012).
- [133] H. Niwa, “Power-law versus exponential distributions of animal group sizes,” *J. Theor. Biol.* **224**, 451 (2003).
- [134] F. Peruani, A. Deutsch, and M. Bär, “Nonequilibrium clustering of self-propelled rods,” *Physical Review E* **74**, 030904 (2006).
- [135] F. Peruani and M. Baer, “A kinetic model and scaling properties of non-equilibrium clustering of self-propelled particles,” *New Journal of Physics* **15**, 065009 (2013).
- [136] A. C. Grimm and C. S. Harwood, “Chemotaxis of pseudomonas spp. to the polycyclic aromatic hydrocarbon naphthalene,” *Appl. Environ. Microbiol.* **63**, 4111 (1997).
- [137] M. Homma, H. Oota, S. Kojima, I. Kawagishi, and Y. Imae, “Chemotactic responses to an attractant and a repellent by the polar and lateral flagellar systems of vibrio alginolyticus,” *Microbiology* **142**, 2777 (1996).
- [138] G. Rosser, A. G. Fletcher, D. A. Wilkinson, J. A. de Beyer, C. A. Yates, J. P. Armitage, P. K. Maini, and R. E. Baker, “Novel methods for analysing bacterial tracks reveal persistence in rhodobacter sphaeroides,” *PLoS Comput. Biol.* **9**, e1003276 (2013).

-
- [139] A. R. Conn, N. I. Gould, and P. Toint, *Trust region methods*, Vol. 1 (Siam, 2000).
- [140] D. A. R. Erban, I G Kevrekidis and T. C. Elston, “Gene regulatory networks: A coarse-grained, equation-free approach to multiscale computation,” *J. Chem. Phys.* **124**, 084106 (2006).
- [141] C. V. D. Broeck, “On the relation between white shot noise, gaussian white noise, and the dichotomic markov process,” *J. Stat. Phys.* **31**, 467 (1983).
- [142] A. C. F. Ribeiro, M. C. F. Barros, L. M. P. Verissimo, V. M. M. Lobo, and J. M. A. Valente, “Binary diffusion coefficients for aqueous solutions of l-aspartic acid and its respective monosodium salt,” *J. Sol. Chem.* **43**, 83 (2014).
- [143] G. Jetschke, *Mathematik der Selbstorganisation* (Springer, 1989).
- [144] F. M. Bandi and T. H. Nguyen, “On the functional estimation of jump–diffusion models,” *J. Econometrics* **116**, 293 (2003).
- [145] H. C. Berg, *Random walks in biology* (Princeton University Press, 1993).
- [146] J. Neyman and E. S. Pearson, “On the use and interpretation of certain test criteria for purposes of statistical inference: Part i,” *Biometrika* , 175 (1928).
- [147] K. J. Duffy and R. M. Ford, “Turn angle and run time distributions characterize swimming behavior for pseudomonas putida.” *J. Bacteriol.* **179**, 1428 (1997).
- [148] S. Funamoto, R. Meili, S. Lee, L. Parry, and R. A. Firtel, “Spatial and temporal regulation of 3-phosphoinositides by pi 3-kinase and pten mediates chemotaxis,” *Cell* **109**, 611 (2002).
- [149] N. Vladimirov, D. Lebiedz, and V. Sourjik, “Predicted auxiliary navigation mechanism of peritrichously flagellated chemotactic bacteria,” *PLoS Comput. Biol.* **6**, e1000717 (2010).
- [150] J. S. Parkinson, “Complementation analysis and deletion mapping of Escherichia coli mutants defective in chemotaxis.” *J. Bacteriol.* **135**, 45 (1978).
- [151] A. Celani and M. Vergassola, “Bacterial strategies for chemotaxis response,” *PNAS* **107**, 1391 (2010).
- [152] Z. Zeravcic, V. N. Manoharan, and M. P. Brenner, “Size limits of self-assembled colloidal structures made using specific interactions,” *PNAS* **111**, 15918 (2014).
- [153] S. Thakur and R. Kapral, “Collective dynamics of self-propelled sphere-dimer motors,” *Phys. Rev. E* **85**, 026121 (2012).

- [154] S.-I. Ei, H. Izuhara, and M. Mimura, “Spatio-temporal oscillations in the Keller–Segel system with logistic growth,” *Physica D: Nonlinear Phenomena* **277**, 1 (2014).
- [155] R. Blakemore, “Magnetotactic bacteria,” *Science* **190**, 377 (1975).
- [156] M. Reufer, R. Besseling, J. Schwarz-Linek, V. A. Martinez, A. N. Morozov, J. Arlt, D. Trubitsyn, F. B. Ward, and W. C. K. Poon, “Switching of swimming modes in magnetospirillum gryphiswaldense,” *Biophys. J.* **106**, 37 (2014).
- [157] K. Pearson, “Mathematical contributions to the theory of evolution. xix. second supplement to a memoir on skew variation,” *Philos. T. Roy. Soc. A.* **216**, 429 (1916).
- [158] S. Terasawa, H. Fukuoka, Y. Inoue, T. Sagawa, H. Takahashi, and A. Ishijima, “Coordinated reversal of flagellar motors on a single *Escherichia coli* cell,” *Biophys. J.* **100**, 2193 (2011).
- [159] A. L. Houwink and W. V. Iterson, “Electron microscopical observations on bacterial cytology ii. a study of flagellation,” *Biochim. Biophys. acta* **5**, 10 (1950).
- [160] J. N. Kapur, P. K. Sahoo, and A. K. Wong, “A new method for gray-level picture thresholding using the entropy of the histogram,” *Comput. Vision Graph.* **29**, 273 (1985).
- [161] J. C. Crocker and D. G. Grier, “Methods of digital video microscopy for colloidal studies,” *J. Colloid Interface Sci.* **179**, 298 (1996).
- [162] A. Savitzky and M. J. E. Golay, “Smoothing and differentiation of data by simplified least squares procedures,” *Anal. Chem.* **36**, 1627 (1964).

Zusammenfassung

Chemotaxis in Systemen aktiver Teilchen ist ein äußerst interessantes Forschungsfeld. Typischerweise untersucht man dafür Zellkolonien. Zuletzt wurde jedoch die Bewegung von aktivierten Kolloiden entlang von chemikalischen Gradienten in Experimenten nachgewiesen, ein Effekt, der auf Diffusiophorese zurückgeführt werden kann. In solchen Systemen im Nichtgleichgewichtszustand treten neuartige Typen kollektiven Verhaltens auf, zum Beispiel “dynamic clustering” (dynamische Aggregation). Theoretische Studien konzentrierten sich bisher vorwiegend auf das kollektive Verhalten ohne Diffusiophorese, obwohl solche Systeme experimentell schwieriger zu realisieren sind.

In dieser Arbeit führen wir ein Modell aktiver Kolloide ein, das Diffusiophorese berücksichtigt. Letzterer Effekt führt zu Interaktionen zwischen den Teilchen, die durch ein chemisches Feld übertragen werden. Dabei zeigen wir, dass für die von uns betrachteten Janusteilchen Diffusiophorese nicht nur zu einer translativen Anziehung (Abstoßung) führt, sondern sich zusätzlich die Teilchen aufeinander zu (voneinander weg) bewegen. Zusätzlich berücksichtigen wir, dass die Interaktionen zwischen den Kolloiden in Gebieten mit hoher Teilchendichte abgeschirmt werden können, weil die zuvor erwähnte Chemikalie nicht frei diffundieren kann. In numerischen Simulationen zeigen wir, dass dieses Modell “dynamic clustering” dann reproduziert, wenn die Teilchen voneinander weg schwimmen, aber sich gegenseitig anziehen. Wir unterteilen diese Phase dynamischen Aggregierens in “dynamic clustering 1” und “dynamic clustering 2”, wobei wir die Größenverteilungen von Clustern analysieren. Des Weiteren beobachten wir einen rapiden Übergang in eine sogenannte kollabierte Phase. Wir überführen unsere Modellgleichungen in die Keller-Segel-Gleichungen, wodurch wir diesen Übergang erklären können. Bei einer genaueren Untersuchung der kollabierten Phase finden wir einen oszillierenden Cluster für bestimmte Parameterkonstellationen. Zuletzt bestimmen wir noch Assoziations- und Dissoziationsraten an den Oberflächen der Cluster und zeigen, dass sie als Indikator für “dynamic clustering” und dessen Übergänge verwendet werden können.

Viele Bakterien führen Chemotaxis dadurch aus, dass sie ihre “run-and-tumble” (laufen und neu orientieren) Bewegung aktiv manipulieren, indem sie die Laufzeit verlängern, wenn sie sich in einem Nahrungsgradienten nach vorne bewegen. Diese sogenannte klassische Chemotaxisstrategie ist bis auf molekulare Ebene erforscht. Die Aufgabe, “tumbles” von “runs” zu unterscheiden, basiert dabei auf einer heuristischen Methode, für die mehrere unbekannte Parameter bestimmt werden müssen.

Im zweiten Teil dieser Arbeit widmen wir uns zellulären Systemen mit Chemotaxis, wobei wir einen künstlichen externen Konzentrationsgradienten eines Lockstoffes anlegen. Wir berechnen sogenannte bedingte Momente aus einem minimalen Modell, das die “run-and-tumble” Bewegung beschreibt. Die bedingten Momente ähneln den sogenannten *Kramer-Moyal-Koeffizienten*. Um die Parameter des Modells zu inferieren, werden die theoretisch berechneten mit den aus den Experimenten berechneten Momenten

verglichen. Unter Verwendung dieser Parameter können wir unser Modell als “tumble”-Erkenner nutzen ohne unbekannte Parameter festlegen zu müssen. Wenn die Bedingungen der Momente adäquat definiert werden, können wir Aussagen zu den Phänomenen Chemotaxis und Chemokinesis treffen. Zuerst bestätigen wir mit unserer Methode die klassische Chemotaxisstrategie und quantifizieren sie. Des Weiteren belegen unsere Resultate die Existenz eines sogenannten “angle-bias” (Winkeldrift), mit dem eine kleine Kolonie unserer Bakterienpopulation effektiver den Gradienten erklimmt. Indem wir auf ganze Trajektorien der Vergangenheit bedingen, können wir verschiedene chemotaktische Antwortfunktionen testen.

Abstract

Chemotaxis in systems of active particles is a most interesting topic to study. Typically, these phenomena are encountered in cellular systems. However, recently, motion along chemical gradients in form of diffusiophoresis in systems of activated colloids has been observed. Such out-of-equilibrium systems give rise to novel types of collective behavior, for example, dynamic clustering emerges. Theoretical studies have been mainly concentrated on collective behavior without diffusiophoresis, although such systems are much harder to realize experimentally.

We here introduce a model of an assembly of active colloids which incorporates diffusiophoresis. The latter gives rise to interactions between the colloids, which are transmitted by a dynamically evolving chemical field. We show that for Janus particles diffusiophoresis leads not only to translational attraction (or repulsion), but also to an effective torque, which orients the particles towards (or away) from each other. In addition, we take into account that interactions may be screened in crowded regions because the chemical field cannot diffuse freely. In numerical simulations we show that this model reproduces dynamic clustering, whenever particles direct their motion *away* from each other. We classify this state in dynamic clustering 1 and 2 by means of their cluster size distribution functions. In addition, we observe rapid transitions to so-called collapsed states. By mapping our model to the Keller-Segel equations, we rationalize this phenomenon. A deeper investigation of the collapsed state reveals a pulsating collapsed cluster for certain parameter configurations. Finally, we calculate association and dissociation rates of clusters and show that they serve as indicator for dynamic clustering and its transitions.

Many Bacteria perform chemotaxis by actively biasing their particular run-and-tumble random walk, where they increase the run length when swimming up a nutrient gradient. This “classical” chemotaxis strategy is well understood down to the molecular level. However, the task of distinguishing runs from tumbles still is based on heuristic procedures, for which several unknown parameters need to be determined a priori.

In the second project of this thesis, we study a cellular system with chemotaxis by considering an externally applied concentration gradient. We analytically calculate conditioned moments similar to Kramers-Moyal coefficients in a basic run-and-tumble model. In order to infer its parameters, the calculated moments are matched to the ones obtained from experimentally recorded trajectories. Using the inferred tumbling parameters, we can turn our model in a tumble recognizer without undefined parameters. Defining the condition of the moments adequately, we draw conclusions on chemotaxis and chemokinesis. As a result, we confirm classical chemotaxis in the bacteria *E.coli* and *P.putida* and quantify it. Furthermore, we give evidence for an additional angle bias, with which a subpopulation *E.coli* orients more effectively towards the gradient. By conditioning on entire bacterial tracks, we can test various chemotactic response functions.

Acknowledgments / Danksagung

Im Laufe meiner Doktorandenzeit habe ich viel und entscheidende Unterstützung von verschiedenen Personen erfahren, bei denen ich mich im folgenden kräftig bedanken möchte. Zuerst möchte ich mich bei meinem Doktorvater, Prof. Holger Stark, für seine Geduld, für wertvolle Anregungen und spannende Diskussionen während meiner gesamten Promotion bedanken. Insbesondere möchte ich mich für die Unterstützung in der Anfangszeit bedanken, die mir als Quereinsteiger das Einleben in die Gruppe erleichtert hat. Außerdem möchte ich mich bei meinem zweiten Betreuer Carsten Beta für viele fruchtbare Diskussionen bedanken.

I am grateful for the funding by the Deutsche Forschungsgemeinschaft through the Research Training Group 1558.

Moreover, I am indebted to many people of our excellent working group and I would like to thank all of the great colleagues I had the pleasure to work with. Thanks to Maria Zeitz and Philipp Kanehl for correcting parts of my thesis. Thank you to Marius Hintsche and Zahra Alirezai for performing the experiments mentioned in this thesis. I would like to thank Christopher Prohm, who never hesitated to help me out with a brilliant google search. Furthermore, I would like to thank Tapan Adhyapak for brightening up my day whenever I entered the seventh floor and for many helpful discussions about physics. *dhônyôbad!* I would also like to thank Julia Eckert for her great support and endless patience. Finally, I would like to thank Raffaele Tavarone for being a good friend and for accompanying me on my way from Rome to Berlin.

I would like to thank Andrea Cavagna and Irene Giardina for their great support and confidence through all the years. Thanks for the warm welcome (back) to Rome you gave me and my family.

Quiero decir gracias por el gran apoyo a la fraccion colombiana, un abrazo para todos. En particular quisiera mandar un abrazo a Fanny, Ceci y claramente mi querida Ana por soportarme durante nuestro tiempo en colombia. Muchas gracias!

Vielen Dank an meine lieben Großeltern, dass ihr immer an mich geglaubt habt.

Vor allem möchte ich meinen lieben Eltern danken, weil ihr einfach immer für mich da wart.

Zuletzt möchte ich noch meiner Diana danken für deine Liebe und Unterstützung während unserer Zeit in Berlin. Und mein frecher Fratz Juli-Lu? Dein zahnloses Lächeln ist meine tägliche Inspiration.